Properties of Hydrogels Incorporating Graphene Oxide-based Nanoparticles for Tissue Engineering Purposes

by

Louis Cheung

A thesis

presented to the University of Waterloo

in fulfillment of the

thesis requirement for the degree of

Master of Science

in

Chemistry (Nanotechnology)

Waterloo, Ontario, Canada, 2016

AUTHOR'S DECLARATION

I hereby declare that I am the sole author of this thesis. This is a true copy of the thesis, including any required final revisions, as accepted by my examiners.

I understand that my thesis may be made electronically available to the public.

Abstract

Tissue engineering involves designing and fabricating scaffolds for tissue regeneration and replacement. Much research has focused on identifying the key factors that affect scaffold performance and the necessary material properties. Nanotechnological approaches have been applied towards tissue engineering and the development of novel biomaterials for scaffold fabrication, such as the incorporation of nanomaterials to supplement the properties of traditional materials. The current work involves the synthesis of graphene oxide (GO) decorated with magnetite nanoparticles to impart magnetic properties to GO, intended for providing anisotropic mechanical reinforcement in hydrogels. Co-precipitation and thermal decomposition were explored as synthesis routes, suggesting that co-precipitation yielded colloidally stable nanoparticles while thermal decomposition yielded magnetite with better crystallinity.

The synthesized GO decorated with magnetite, GO-Fe_3O_4, was incorporated into alginate hydrogels and the mechanical properties were explored. It was shown that GO and GO-Fe_3O_4 enhanced hydrogel stiffness to similar extents. Due to its rigid nature, hydrogels incorporating GO-Fe_3O_4 tended to fracture at lower strains. Anisotropic alignment and mechanical reinforcement could not be demonstrated due to the synthesized GO-Fe_3O_4 having insufficient magnetic response.

As another strategy to enhancing the mechanical properties of hydrogels, GO was covalently attached to alginate polymer chains (GO-EDA-alginate). Mechanical tests indicated that GO-EDA-alginate does not increase the stiffness of the hydrogel, but enhances the toughness, which can be due to improved interactions between GO and the polymer phase, leading to better energy dissipation.

Finally, the use of alginate as a scaffold material was explored by investigating cell viability. It was shown that the crosslinking process was cytotoxic, although modifications to the protocol could alleviate the problem, in part.

The current work demonstrates the use of GO-based nanoparticles as reinforcing nanofillers which could be extended to polymer systems beyond alginate. It is anticipated that magnetic ordering can lead to anisotropic material properties, such as mechanical properties and electrical conductivity. This material could also find application in providing mechanical stimulation to cultured cells via application of an external magnetic field.

Acknowledgements

I would like to thank my supervisor, Dr. Shirley Tang, for providing me an environment in which to learn and develop as a researcher. I am grateful for being given academic freedom while being given the support and guidance when it was needed. I would also like to thank the past and current members of the group: Dr. David Donkor, Dr. Mahyar Mazloumi, Dr. Samaneh Shadmehr, Xiguang Gao, Andrew Ward, Mike Coleman, Yverick Rangom, Zhi Li, Gaganprit Gill, Kai Wang, and Yun Wu.

Through my interactions with staff and colleagues across various research groups, I have been able to learn about various aspects relating to science and doing research. My work would not have been possible if they had not generously given me some of their time and advice.

I would like to thank the research groups that have graciously let me use their facilities, including Prof. Juewen Liu, Prof. Hyock Ju Kwon, Prof. Linda Nazar and Prof. Michael Tam. Also, I would like to acknowledge Debbie Wu from Prof. Michael Tam's group, who helped me with the TEM characterization, Dr. Shantinarayan Rout for helping me run samples on the SQUID, and Takuto Kwok from Prof. Linda Nazar's group who helped me run the cobalt XRD samples.

Table of Contents

List of Figures

List of Tables

List of Abbreviations

AFM: atomic force microscope

APTES: (3-aminopropyl)triethoxysilane

BSE: backscattered electrons

CLSM: confocal laser scanning microscope

CNTs: carbon nanotubes

DEG: diethylene glycol

DGEA: aspartic acid-glycine-glutamic acid-alanine

DLS: dynamic light scattering

DNA: deoxyribonucleic acid

ECM: extracellular matrix

EDA: ethylenediamine

EDC: 1-Ethyl-3-(3-dimethylaminopropyl)carbodiimide

EDTA: ethylenediaminetetraacetic acid

EDX: energy dispersive x-ray spectroscopy

EthD-1: ethidium homodimer-1

FTIR: Fourier transform infrared

FWHM: full width at half maximum

GAGs: glycosaminoglycans

GO: graphene oxide

HA: hydroxyapatite

HBSS: Hank's balanced salt solution

ICSD: inorganic crystal structure database

MES: 2-(*N*-morpholino)ethanesulfonic acid

MPMS: magnetic property measurement system

MRI: magnetic resonance imaging

MSCs: mesenchymal stem cells

MTS: (3-(4,5-dimethylthiazol-2-yl)-5-(3-carboxymethoxyphenyl)-2-(4-sulfophenyl)-2H-tetrazolium)

MTT: 3-(4,5-dimethylthiazol-2-yl)-2,5-diphenyltetrazolium bromide

NHS: *N*-Hydroxysuccinimide

PCL: poly-caprolactone

PES: polyethersulfone

PHSRN: proline-histidine-serine-arginine-asparagine

PLGA: poly-lactic-co-glycolic acid

RGD: arginine-glycine-aspartic acid

SE: secondary electrons

SEM: scanning electron microscope

SQUID: superconducting quantum interference device

TCP: tricalcium phosphate

TEM: transmission electron microscope

TGA: thermogravimetric analysis

UV: ultraviolet

XRD: x-ray diffraction

XTT: (2,3-bis-(2-methoxy-4-nitro-5-sulfophenyl)-5-[(phenylamino)carbonyl]-2H-tetrazolium hydroxide)

Chapter 1: Introduction to Tissue Engineering

1.1 Tissue Engineering

Tissue engineering is a multidisciplinary field which aims to develop therapeutic products for the purpose of replacing and regenerating cells and tissue lost to natural aging, injury, disease.[1–3] Tissue and organ repair have traditionally been performed by either tissue grafting or organ transplantation; or by synthetic material replacement.[4,5] Both of these approaches have their drawbacks. Tissue grafting requires a source of tissue from the patient, referred to as an autologous source, or from another host, referred to as an allogeneic source, and is plagued by the limited amount of material available, the cost and pain of transplantation procedures, and the possibility of an immune response or disease transmission in the case that the transplanted tissue is from another host; while synthetic materials integrate poorly with native tissue and fail over time from wear and fatigue. In the early 1990s, a paradigm shift occurred, transitioning from the traditional methods to one where a degradable, porous material is implanted, carrying biomacromolecules such as cells, genes and proteins to aid in the recovery. Such synthetic material helps to retain the tissue volume, while providing mechanical strength and delivery of the biomacromolecules. This is the approach used for contemporary tissue engineering research. Although it is possible to use cell-free scaffolds, recent advances in tissue engineering stress the encapsulation of mature cell types or stem cells.[6] The intention of the implanted material is thus to provide a framework on which cells can adhere, proliferate, migrate and differentiate to restore the original function of the lost or diseased tissue. The potential of tissue engineering has been recognized to be of importance in the areas of skin, cartilage, bone, blood vessel, nerves and soft tissues.[3,7]

In addition to the goal of tissue replacement, scaffolds have garnered interest in the field of cell culturing with 3D matrices, and are important in the study of disease pathology such as cancer, toxicological studies, and drug discovery.[8–11] By emulating the extracellular matrix (ECM), cells in culture communicate and behave differently, leading to the observation of different mechanisms in growth and motility which more closely resembles to what happens in the natural *in vivo* environment. Traditionally, *in vitro* tests have been performed on 2D substrates, due to their simplicity in preparation and use in assays, and as such have been adopted

by industry as an inexpensive way to perform multi-variable drug testing. However, numerous reports have shown that cells behave fundamentally differently when cultured in a 3D environment, owing to the cells' interactions with the matrix material and how cells communicate with each other in this unique environment. For example, in cancer research, it was shown that the cell binding activity to surfaces was different when 2D and 3D substrates were compared directly.[8] Antibodies against a cell-to-matrix receptor, β-1 integrin, changed the behaviour of cancerous cells only in a 3D environment, causing the cells to become non-cancerous and losing properties of cancerous cells such as their abnormal shape and growth patterns. This initial finding spurred further research into exploring the use of 3D culturing materials for cancer research, and led to discoveries such as furthering the understanding of how cancerous cells metastasize and migrate in a matrix as the binding between cell-surface receptors and the matrix material was cleaved by specific enzymes. In addition, the characteristics of normal cells such as fibroblasts grown in 3D environments have been studied and contrasted with 2D substrates, and has shown that the cell shape, distribution of transmembrane proteins, and regulation of gene expression are all different than what was traditionally observed in 2D systems.[9] The explanation for this behaviour, in short, is that cells are confined to grow and communicate with their extracellular environment and neighbouring cells on a planar surface, resulting in an unnatural binding of integrins with the matrix and the associated abnormal mechanical signals experienced by cultured cells as they interact with the ECM.[12] Other factors are in play, such as the abnormal concentration gradient of dissolved nutrients and growth factors in the cell media which contact a limited surface area of cell membranes exposed to the bulk media, but the conclusion is that cells in culture interact with their 3D environment in a different manner than a 2D culture environment. New discoveries are continuously being made in the field of 3D cell culturing, and these advances will help to provide more reliable and accurate data for drug screening as a relatively inexpensive alternative to animal testing, as well as improving integration of implanted scaffolds with host bodies.

1.2 Bone structure

A short review of the structure of bone is useful for illustrating the complexity of natural tissue. Bone is made up of two distinct types of tissue: cancellous and cortical bone.[13] Cancellous

bone, also known as spongy or trabecular bone, is highly porous, supporting the production of blood and providing a reservoir for calcium and phosphorus. As opposed to the temporal and spatial variation of cancellous bone, cortical bone, also called dense or compact bone, is a solid and hierarchically structured material. Due to the laminated structure, cortical bone is able to withstand much higher compressive stress while providing vascularization for the bone tissue as it continually renews itself. **Figure 1.1** provides a visual representation of cancellous and cortical bone.

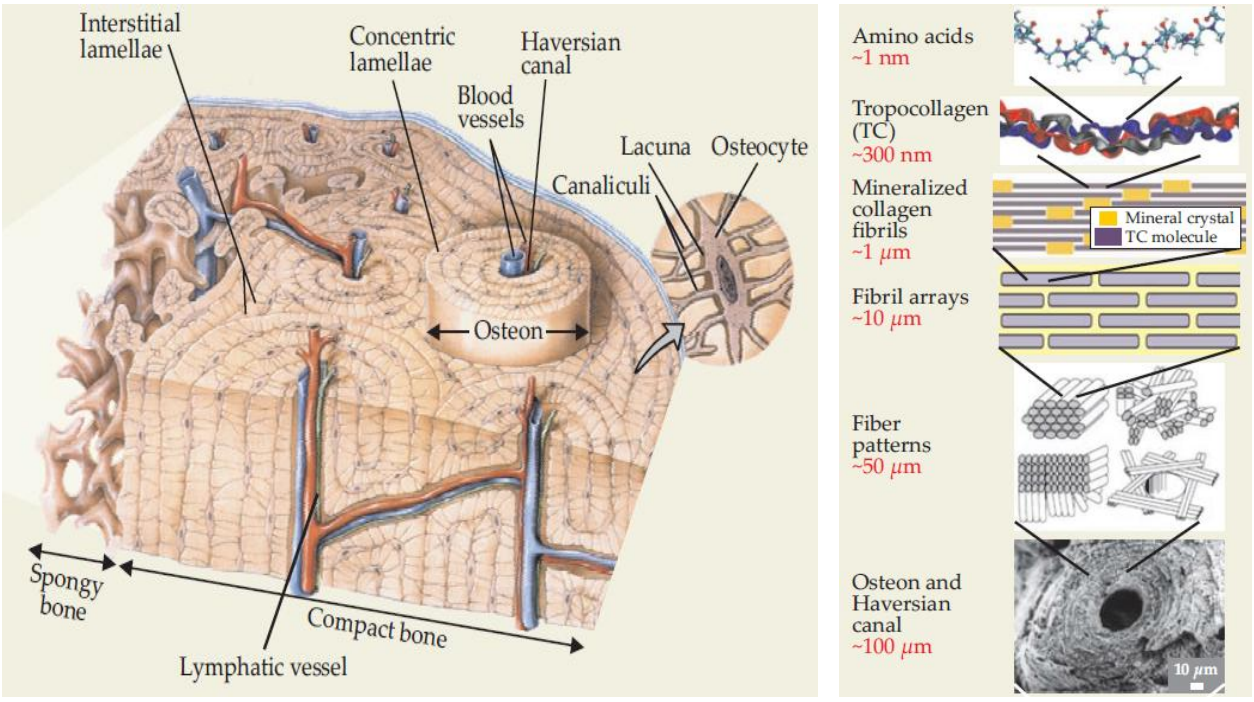

Figure 1.1: Bone Structure. The general structure of bone (left); depiction of the hierarchical nature of bone tissue (right). Adapted from ref. 13.

At the fundamental level, the ECM of bone is made up of one third of organic material, mainly collagen, and two thirds inorganic material, mainly hydroxyapatite (HA) and calcium phosphate, by mass, highlighting the specific needs of this type of tissue.[6] As represented in **figure 1.1**, hydroxyapatite mineralizes in the gaps between collagen fibres, leading to self-assembled templates that aid in bone tissue formation.[13] Bone is made of three major cell types: osteoblasts, osteocytes, and osteoclasts.[6] Each have their own functions, such as the synthesis of ECM, regulating matrix mineralization, and mechanical sensing and signaling. The interactions between these types of cells determine skeletal growth and modelling. Hence the precise organization of these cells into functional tissues is crucial.

1.3 Overview of Tissue Properties Crucial for Artificial Scaffolds

In the early days of exploring scaffold materials for tissue engineering, several requirements were defined. The creation of artificial scaffolds revolves around recreating the extracellular matrix in which cells reside, as such a short discussion of the chemical and physical properties of the ECM is appropriate. The ECM provides a 3D environment in which cultured cells grow in, and the immediate extracellular environment has been summarized to contain three major components: (1) the ECM backbone made of fibrous and hydrated proteins such as collagen that provide a structural framework and mechanical strength, glycoproteins consisting of proteins with oligosaccharides (or glycans) covalently attached to the side chains of amino acids through post-translational modification and includes compounds such as elastin, laminin and fibronectin, as well as hydrophilic proteoglycans which are proteins with covalently bound glycosaminoglycans (GAGs) side chains (long polysaccharides consisting of a repeating disaccharide unit), (2) biomolecules bound by proteoglycans and includes growth factors, chemokines and cytokines which signal important processes within cells such as the regulation of gene expression, direction of cell phenotype and tissue organization, and establishing homeostatic conditions, and (3) neighbouring cells which interact with other cells and the ECM through proteins presented on the cellular membranes.[10,12,14,15,16] Each component of the ECM has a specific purpose; for example, whereas fibrous collagen provides mechanical strength to the matrix, elastin provides elasticity to the material and proteoglycans control the level of hydration in the overall matrix resulting in tunable resistance to compressive forces and transport rates of macromolecules diffusing through the porous structure.[16] Encapsulated cells interact with the ECM matrix in a bidirectional manner as the cells attempt to reach a homeostatic state. The specific composition of the ECM varies with different tissue, and it is also important to stress that the body constantly breaks down and restructures the ECM through specific proteins such as metalloproteinases as encapsulated cells proliferate and mature. The degradability and chemical stability of the selected scaffold material under physiological conditions (pH, temperature, ionic strength) need to be tailored such that the material degrades over time once the encapsulated cells are able to proliferate and produce their own ECM components. Choosing the appropriate materials to emulate the target tissue is a challenge, as batch-to-batch variability of the provided materials can cause scaffolds to have poorly controlled mechanical and

biochemical properties, not to mention that the optimal culture conditions may not be known beforehand.[12]

The material must support cell adhesion and subsequent proliferation. To facilitate this, the material must be porous to facilitate the transport of oxygen and nutrients, as well as the removal of waste products as a result of cell metabolism. The porosity and pore size distribution of the scaffold encourages the migration of native cells into the scaffold, leading to integration with the host body, which is called the property of osteoconduction in the context of bone tissue engineering.[6] In addition, the scaffold material must not release agents that are toxic or otherwise initiate an inflammatory response, a property called biocompatibility.[6]

The mechanical properties of scaffolds must be tailored to the specific cell or tissue type being investigated. For example, brain tissue tends to be soft, on the order of 1kPa; muscle tissue is of intermediate stiffness on the order of 10kPa, whereas bone tissue is relatively stiff on the order of 100kPa.[17] Mechanical properties can be optimized through appropriate material selection and tailoring the degree of crosslinking. Scaffold stiffness has been found to affect cell migration speed through the matrix in addition to factors studied in 2D systems such as the density of receptors on cell membranes and number of ligands on the matrix surface which affects the adhesion of cells to the matrix[18]; as well as cell differentiation, where the sensitivity of seeded mesenchymal stem cells (MSCs) to matrix stiffness was used to direct their differentiation into brain, muscle or bone cells as the matrix stiffness was increased through chemical crosslinking in a collagen-coated, polyacrylamide gel system.[17] Cells interact and deform their surrounding matrix through integrin binding, converting mechanical signals into chemical signals, and affects reorganization of intracellular components as they accommodate applied stresses which determine cell phenotype, and on a larger scale affects cell organization into functional tissue, such as endothelial layers.[16] From an engineering standpoint, the mechanical strength of the scaffold material must be enough to withstand handling of the material during transplants, and wear from the abrasion from physiological loading and *in vivo* processes such as the migration of cells. The scaffold must retain its structure and integrity to function as a mechanical support for implanted cells, until the cells have organized into functional tissues and integrated with native tissue.[5]

The morphology, or surface topography, has also been explored as a relevant factor in enhancing the biological functions of scaffolds. For example, researchers designed a specific

peptide containing phosphoserine, an amino acid, and observed that the mineralization of hydroxyapatite was enhanced, and the crystallinity was preferentially oriented along the peptide fiber's long axis. It was theorized that the presence of the acid group on the amino acid or highly negatively charged groups in general enhanced the mineralization of HA as those groups could capture the salts of calcium and phosphorus effectively to start the crystallization.[19] In another instance described in the same review paper,[19] a hybrid copolymer combining poly[n-(2-hydroxypropyl)methacrylamide] with a β-sheet peptide, which is a peptide sequence that self-assembles into a sheet-like structure, created an anisotropic porous structure, where the peptides helped to capture ions and influenced the mineralization of HA into a particular morphology.

The design of the bulk material chemistry is important, but another crucial element of scaffold materials is the surface chemistry. The surface of the material is what interacts with the in vitro and in vivo environment, and includes phenomena such as protein, ion and molecular interactions such as adsorption and desorption, as well as interactions with whole cells which relate closely with the scaffold property of cell adhesion. With the exception of collagen, polymers usually do not have receptors or ECM proteins such as laminin, fibronectin and vitronectin to promote the adhesion of cells. To promote cell recognition and binding with scaffold materials, ECM components are often used as "tethering moieties" to capture cells.[19] This strategy is usually employed with synthetic polymers and natural polymers which lack cell recognition sequences and have poor cell adhesion, such as chitosan and alginate. Proteins are of special interest. For example, poly-caprolactone (PCL) has been modified with laminin to better mimic the nerve basement membrane for neural cell tissue engineering.[19] Chitosan has been modified with collagen or fibronectin in numerous instances to enhance the adhesion of cell types such as chondrocytes and MSCs. Aside from the protein components of the ECM, other compounds such as GAGs can be used. These components have been shown to also confer enhanced capture of growth factors, such as the use of heparin to capture fibroblast growth factors.[19] This technique of surface modification can also be applied to inorganic or inorganic/polymer hybrid scaffolds. A very important example of this is the modification of HA or polymers with HA mineral with osteocalcin, which is a key protein in the ECM of bone tissue. In fact, the adsorption of other bone-related proteins is also favourable due to the presence of cations such as calcium and phosphorus which electrostatically interact with the acid groups on proteins. Yet another component that has been used to modify the surface of scaffold materials

are peptide fragments, which have been identified as the key regions of recognition by encapsulated cells. The use of engineered peptides is advantageous in that the presence of factors that can affect whole protein folding and conformation such as solvents, temperature and pH would not affect short peptide sequences, such that the recognition sites on the peptide fragments would always be available for binding. Examples of peptides engineered from proteins include arginine-glycine-aspartic acid (RGD) and aspartic acid-glycine-glutamic acid-alanine (DGEA) derived from collagen, and proline-histidine-serine-arginine-asparagine (PHSRN) derived from fibronectin.[11,19]

Taking this one step further, the incorporation of biomacromolecules, such as cytokines, and growth and differentiation factors, is a powerful strategy to mimic the spatial and temporal variability of natural tissue, and is a idea commonly explored in efforts to direct stem cell fate,[15,20] although the difficulty lies in identifying the chemical signals that the body uses to direct cell proliferation, motility, and differentiation.[21] Strategies have been established to incorporate molecules such as drugs, nucleic acids and proteins in porous foam scaffolds, hydrogels, nano- and microfibrous mats and in nano- and microspheres depending on the desired time frame for the release of these compounds. The compounds can be incorporated into the internal structure of the scaffold material, which leads to longer-term release or incorporated onto the surface of the material through covalent bonds or adsorption, which leads to shorter-term release. Certain macromolecules functionalized to the surface of scaffolds such as heparin have been shown to improve the binding affinity for growth factors, leading to a longer release profile, due to its ability to capture molecules through electrostatic binding. The time scale of the release of therapeutics is crucial for proper maturation of cells, and more advanced delivery of therapeutics have been developed. For example, the use of microspheres to encapsulate therapeutics has been explored. Poly-lactic-co-glycolic acid (PLGA) microspheres have been developed, as well as composites, such as PLGA combined with calcium phosphate have been shown to provide a controlled and sustainable release of molecules, where the use of composite materials allows the tailoring of the decomposition rates of the delivery vehicles and hence, release kinetics.[19] The release profile can be very steady, as demonstrated by the use of PCL microspheres for the delivery of levonorgestrel, showing a zero-order release profile for four months.[19] Similarly, for electrospun fibers, one of the strategies used is the design of core-shell fibers, where the release of therapeutics can be tailored based on the degradation rate of the outer

shell as well as the affinity for the therapeutic molecules with the material used for the core. Finally, the release of molecules can be triggered through external stimuli, most commonly to sensitivity towards pH, temperature and magnetic fields, and spans an entire field related towards the design of smart, stimuli-responsive biomaterials.[19]

As ECM conditions vary in a temporal and spatial manner, researchers have attempted to control certain environmental variables and include certain forms of stimulation to cultured cells to provide optimal conditions for proliferation and differentiation, tailored to the particular cell type. For example, work in this field of "bioreactors" can be summarized into stimulation through perfusion, mechanical, and electrical means.[22] In the area of perfusion, one particular component that has been explored in addition to the supply of nutrients, is the supply of oxygen. It has been noted that oxygen solubility in aqueous forms such as blood plasma and cell media is low, and that the distance that oxygen can be transported through diffusion in order to support dense cell populations is about 100μm resulting in hypoxic conditions for the interior of cell scaffolds unless further measures are taken to vascularize the constructs. Without providing too much detail, possible solutions to this problem include the patterning of microchannels to simulate vascularization, as well as the construction of reactors where a continuous supply of cell media is introduced to cultured cells which ensures a high oxygen supply and hence diffusion of oxygen to the cells.[22,23] Mechanical stimulation operates on the principle that cells remodel their internal structure in response to mechanical signals, and as such it is possible to promote cells with structures that have particular functions. An obvious example of tissue that responds to mechanical signals and remodels itself to enhance performance are load-bearing tissues such as bone, where they are intended to sustain loads along their long axis. Moreover, providing mechanical stimulation to cultured cells introduces movement to the fluid surrounding cells to improve the flux of nutrients and metabolites. The use of mechanical stimulation to guide the maturation remodelling of tissue has been applied to cartilage, bone and heart tissue. Electrical stimulation applies to tissue that rely on the propagation of electrical impulses across cell-cell junctions to induce mechanical contractions on the macroscopic scale. An instance of research in this topic involves the *in situ* electrical stimulation to cardiac tissue, which showed that cells organized themselves to enhance cell-cell coupling and electrical signal propagation leading to improved tissue contraction.

The conclusion is that understanding and recreating the natural ECM to further improve cell proliferation and differentiation is a complex issue, involving the chemical and physical properties of the scaffold material as well as the chemical signals received by the encapsulated cells. **Figure 1.2** summarizes some of the factors that need to be considered when designing and optimizing a scaffold.

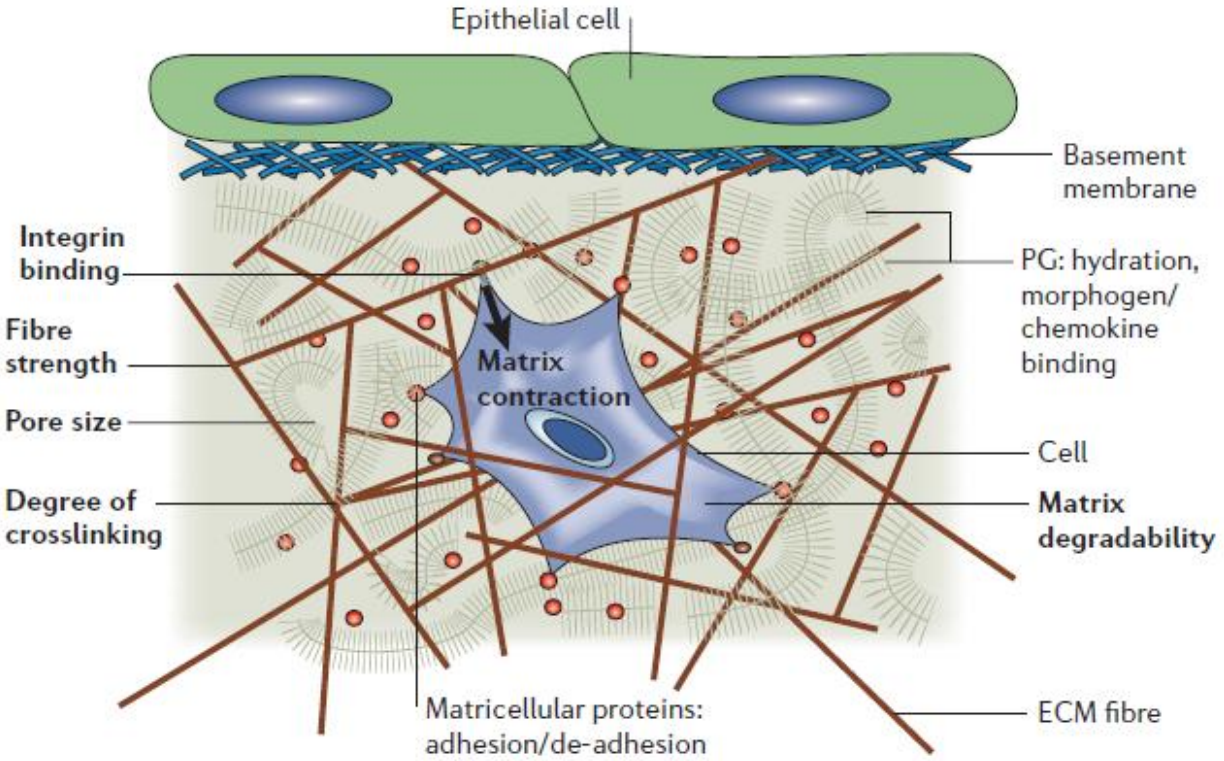

Figure 1.2: Cells in the *in vivo* environment. Cells cultured in a 3D scaffold are subject to many factors, which have to be considered when selecting materials to use in an artificial scaffold. PG is an acronym for proteoglycan. Reproduced with permission from ref. 16. © 2006 Nature Publishing Group.

1.4 Methods of Validating Tissue Scaffold Performance

The following section reviews some of the commonly used techniques to evaluate the performance of artificial scaffolds and their suitability as a tissue replacement. For hydrogels intended as a replacement for load-bearing tissues, the mechanical properties must be investigated. Such studies can yield fundamental information such as the polymer structure or molecular weight between crosslinks, and the viscoelasticity of bulk hydrogel samples.[24] The most basic and commonly studied mechanical property is the stiffness/elasticity and viscoelasticity. Stiffness of hydrogels can be measured using tensile or compressive strains.[24–26]

Tensile testing involves mounting a hydrogel strip between two grips and applying a outward pulling force to obtain stress data. The resulting stress-strain graphs can be used to identify properties such as the Young's modulus, yield strength and ultimate tensile strength. Compressive testing involves mounting samples in between two parallel plates and compressing the sample to measure the force experienced by the sample. The stiffness can be calculated using models such as a linear fit or rubber elasticity theory.[24] Viscoelasticity refers to the time-dependent deformation or recovery of materials as strain or stress is applied, where materials demonstrating no lag in recovery is referred to as perfectly elastic while materials exhibiting recovery after a lag phase are referred to as viscoelastic. This property is measured by dynamic mechanical testing, where a sample is periodically deformed using controlled strain or stress in a sinusoidal manner, and a transducer measures the resulting stress or strain experienced by the sample, respectively. This technique can be used on solid hydrogel samples or polymeric pre-gelated solutions, which is referred to as the rheological properties, since both of these types of samples exhibit viscoelastic behaviour.[27]

Toughness is another mechanical property often studied.[26,13,28,29] Toughness measures the amount of energy that a brittle material can absorb before fracture, in the presence of an existing crack or an undamaged sample. For un-notched samples, the property being measured is known as the toughness, and includes the energy needed for a crack to form and propagate until ultimate failure, whereas notched samples quantify the fracture toughness, which is limited to the energy for crack propagation up until fracture. It is generally recognized that using tensile and compressive testing to measure toughness is not very reproducible or reliable, as crack formation is highly dependent on artifacts within the gel and may form from different sources.[26] Toughness is calculated by integrating the area under the curve up until fracture, but such tests often vary widely in the ultimate strain, leading to variability in the ultimate stress and hence calculated toughness. As an alternative, performing notched tensile tests or micro/nano-indentation tests are widely accepted as yielding reproducible results, where crack formation is well defined either by cutting a macroscopic scale defect into the sample or using a probe to introduce a micro or nano-sized defect and allowing such defects to propagate over the course of mechanical loading.

The electrical conductivity of the scaffold matrix is important for cell types that involve electrical signal propagation such as neurons and cardiomyocytes, and can be measured as a bulk property using a four-point probe setup to measure conductivity,[30] or an impedance spectroscopy

instrument to measure impedances.[31,32] It is even possible to use a conductive atomic force microscopy (AFM) tip to probe specific points of a scaffold to probe point-to-point electrical conductivity.[31]

The mass transport properties of hydrogels are important to the survival of encapsulated cells. Compounds of interest include gasses, nutrient and waste products, which move through hydrogel matrices mainly through the mechanism of diffusion.[33] Diffusion depends on several factors, such as the hydrodynamic or Stokes radius of the analyte as well as the porosity of the scaffold network. Porosity and pore size distribution are affected by the properties of the polymeric material such as the molecular weight, weight volume of polymer used, and the crosslinking density. The porosity and pore size distribution can be observed by microscopy, specifically scanning electron microscopy, and gas adsorption techniques. For gas adsorption experiments, Brunauer–Emmett–Teller theory can be used to elucidate the total surface area and pore size distribution of a porous material.[34,35] These techniques require a dried sample, however sample preparation has to be carefully performed; for hydrogels in particular the method of freeze drying has been shown to produce varying pore sizes depending on the size of ice crystals formed during the freezing process.[36]

Proliferation of cells measures the growth rate over a period of time, from several days to weeks, by directly or indirectly counting the number of cells present in a number of replicate wells. Cell proliferation can be quantified qualitatively by the use of a haemocytometer combined with trypan blue dye for passaged cells, whereas cells encapsulated or seeded onto scaffolds can be similarly observed under optical microscopy with trypan blue dye. The trypan blue stain operates under the principle that viable cells are impermeable to this dye, while dead cells are permeable and will be labelled due to ruptured cell membranes. Viability can be made more accurate by performing the stain in replicates. Moreover, cultured cells can be observed for their morphology as an indicator of their proliferation. Suppliers of cell stocks typically provide graphical references, but for adherent cell lines, healthy cells tend to exhibit a stretched morphology as they attach and spread onto substrates, whereas the appearance of a balled-up shape indicates that the cells are lifting from the substrate and aren't proliferating. The proliferation of cells may also be quantitatively reported, and can be achieved through commercially available products such as Quant-iT™ PicoGreen® dsDNA staining kit from Invitrogen. In this particular instance, double-stranded deoxyribonucleic acid (DNA) is

selectively labelled and can be used to quantitatively report on cell counts using a spectrophotometer capable of fluorescence measurements, and is used in work involving the purification and amplification of DNA for diagnostics or polymerase chain reaction protocols.[37] By comparing with a known standard, cell counts can be quantitatively reported selectively in the presence of compounds that typically contaminate nucleic acid samples and with high sensitivity and linearity compared with other stains such as Hoechst 33258. The viability of cells can be determined using a combination of dyes simultaneously. An instance of this is the Live/Dead® Viability/Cytotoxicity kit supplied by Invitrogen.[38] In this case, the assay involves calcein-AM and ethidium homodimer-1 (EthD-1). Calcein-AM is cell-permeable, and can be used to measure intracellular esterase activity, since this enzyme converts the non-fluorescent calcein-AM to highly fluorescent calcein. Ethidium homodimer-1 is permeable only to ruptured cell membranes and will selectively bind to double-stranded DNA, exhibiting fluorescence enhancement. As a result, the assay provides simultaneous information about cell activity and viability, as well as the presence of cytotoxic compounds. This technique can be used to provide qualitative information though the use of fluorescence microscopy or quantitative information using a flow cytometer or spectrophotometer capable of detecting fluorescence phenomena.

Cell activity can be quantitatively determined by the classical 3-(4,5-dimethylthiazol-2-yl)-2,5-diphenyltetrazolium bromide (MTT) assay.[39] This assay relies on dehydrogenase enzymes located in active mitochondria inside cells, which act on the MTT molecule, converting the water-soluble MTT into a water-insoluble formazan dye when the tetrazolium ring is cleaved. Upon solubilizing with solvents such as dimethyl sulfoxide, the formazan is dissolved into a purple product that can be quantitatively determined using a UV-vis spectrophotometer. Other tetrazolium salts include (2,3-bis-(2-methoxy-4-nitro-5-sulfophenyl)-5-[(phenylamino)carbonyl]-2H-tetrazolium hydroxide), also called XTT,[40] (3-(4,5-dimethylthiazol-2-yl)-5-(3-carboxymethoxyphenyl)-2-(4-sulfophenyl)-2H-tetrazolium), also called MTS,[41] as well as a series of water-soluble tetrazolium salts. In addition to observing mitochondrial activity as an indicator of cell proliferation, the MTT assay has also been used to indicate overall viability or cytotoxicity.[39] A closely related behaviour often studied is cell migration. Fluorescent dyes such as CellTracker™ fluorescent probes which can be used to fluorescently label cells and retain fluorescence for up to 72 hours while posing no toxicity, making such probes ideal for tracking cell motion for extended experiments.[42]

Differentiation of cells is typically determined through the use of antibodies specific to surface-presented antigens on the cell membranes of the cell type being studied, and can be quantitatively and qualitatively reported through the use of secondary antibodies labelled with fluorophores. For example in bone tissue engineering, an enzyme called alkaline phosphatase can be labelled with antibodies, and can be visualized under fluorescence microscope or quantified using a fluorimeter.[23,43,5] Other protein markers for bone include osteopontin and osteocalcin. Furthermore, calcium and phosphate can be stained with alizarin red and the Von Kossa method, respectively.[5] In the investigations of cardiomyocytes, connexins are commonly labelled.[32,30,31] These are transmembrane proteins that form gap junction channels that regulate electrical coupling between cells. Proteins can also be extracted and quantified using a Western blot procedure.

1.5 Biomaterials used in Tissue Scaffolds

The field of biomaterials for regenerative medicine purposes focuses on mimicking the ECM backbone introduced in **Section 1.3**. The use of polymers, both natural and synthetic, in tissue engineering is widespread, where the polymers are fabricated into hydrogel networks. In this fashion, the porosity and rate of degradation can be controlled by the degree of cross-linking and molecular weight; in addition the delivery of biomacromolecules can be incorporated.[6] Natural polymers are advantageous in that they are generally more biocompatible than synthetic polymers, owing to the fact that these polymers are components of or have properties of native ECM, but suffer from poorer mechanical properties. Polymers of interest include collagen, hyaluronic acid, alginate and chitosan. Particularly, collagen is a highly investigated material due to its natural abundance.[33] Methods of crosslinking include the use of chemical crosslinkers, such as glutaraldehyde, formaldehyde and carbodiimide, or through physical processes such as ultraviolet (UV) radiation, freeze drying or heating. Collagen is amenable to natural degradation processes, and is broken down by metalloproteases such as collagenase and serine proteases. It is also possible to blend more than one polymer together to tailor mechanical and degradation properties.

Synthetic polymers are favourable since their chemistry, and hence properties, are controllable and reproducible.[33] The molecular weight, block structure, crosslinking density and

mode of crosslinking can be tailored to the needs of the application. Polyethylene glycol is a hydrophilic polymer, commonly applied to biomedical applications with some approved by the United States Food and Drug Administration. Methods of crosslinking include the incorporation of acrylate or methacrylate groups which allows the photo-crosslinking of polymer chains upon UV light exposure. Block copolymers of polyethylene glycol and poly(L-lactic acid) have been shown to be thermally reversible in their gelling behaviour. Polyvinyl alcohol can be physically crosslinked with repeated freeze-thaw cycles of aqueous polymer solutions, or by chemical crosslinking with glutaraldehyde, succinyl chloride, adipoyl chloride and sebacoyl chloride. Other synthetic polymers of interest for bone tissue applications include polycaprolactone, poly(glycolic acid) and poly(lactic-co-glycolic) acid.[6]

Another class of materials that have been explored for bone tissue engineering is ceramics.[6] In particular, calcium sulfate and calcium phosphates, such as hydroxyapatite and β-tricalcium phosphate (TCP) have been used. Advantages include biocompatibility and degradation over time as the injected material integrates with native tissue, however this class of material tends to be brittle under compressive stress and have limited porosity. In many cases, research in the field of tissue engineering employs the use of composite materials, combining natural, synthetic and inorganic materials in unique combinations to emulate the chemical and mechanical properties of the ECM.[19]

The delicate balance of maintaining an acceptable porosity, degradation, and mechanical strength is a challenge in the area of tissue scaffolds.[1] Simply put, the use of hydrogel matrices made of polymeric material alone do not confer all the necessary attributes necessary for supporting cell proliferation compared with native ECM. Polymers such as collagen do not have the same mechanical properties, possessing a Young's modulus of approximately 100MPa, while the Young's modulus of bone ranges in between 2-50GPa.[1] Increasing the cross-linking density to increase mechanical strength comes at the cost of decreased porosity and longer degradation times, which is not a viable solution since the viability and spreading of encapsulated cells is compromised.[44] The topography of polymeric scaffolds usually lack nanofibrous architectures, on the order of 10-100nm, which are found in native ECM and serve to regulate cell behaviour.[32] Finally, the electrical conductivity of polymeric scaffold materials at biologically relevant frequencies, which range from direct current to several hertz, is too low to allow electrical

signals to propagate along cells.[32] To address these shortcomings of polymeric materials, the use of nano-fillers have been explored, leading to the creation of hybrid synthetic materials.

The addition of natural or synthetic hydroxyapatite into polymers has achieved positive results, owing to the osteoinductivity of HA. The incorporation of calcium phosphates such as HA and β-TCP have been proven to be osteoinductive since these minerals can bind with endogenous bone morphogenetic proteins to help with the crystallization of osteoblasts, due to the surface roughness introduced by the minerals.[1,45] For example, it was found that while collagen and HA individually support the differentiation of stem cells into osteoblasts, the combination of the components accelerated the process of osteogenesis. As a mineral found in natural bone, it has been shown that the presence of HA improves biocompatibility and mechanical strength over the bare polymer.

The selected biomaterials can be used to form several morphologies.[14,2] The simplest way is to form hydrogels, in which polymeric materials are physically or chemically crosslinked into a hydrated network. While in this form factor, polymer chains are susceptible to conditions such as the solvent, ionic strength, pH and temperature. For example, thermally responsive polymers like poly(N-isopropyl-acrylamide) demonstrate phase separating behaviour depending on the temperature. Above the lower critical solution temperature, the polymer phase tends to interact with itself more favourably leading to phase separation, whereas below the critical temperature, hydrogen bonding dominates and results in dissolution in water. Scaffolds can also be made as a porous foam, where the polymer is injected with particulates such as sodium chloride, sugar or paraffin, which take up a certain volume but can be removed afterwards by chemical means, leaving voids in the matrix. Such porous foams can also be made by foaming, where gas bubbles are introduced by chemical reactions or the introduction of supercritical CO_2 which expands and decompresses, leaving porous voids. Finally, fibrous mats can be produced by electrospinning,[7,46–48] where an electric field is used to draw polymeric solutions into fibers with nano- to micron scale diameters which are collected on a grounded plate, or by phase separation. This information is summarized in **figure 1.3**.

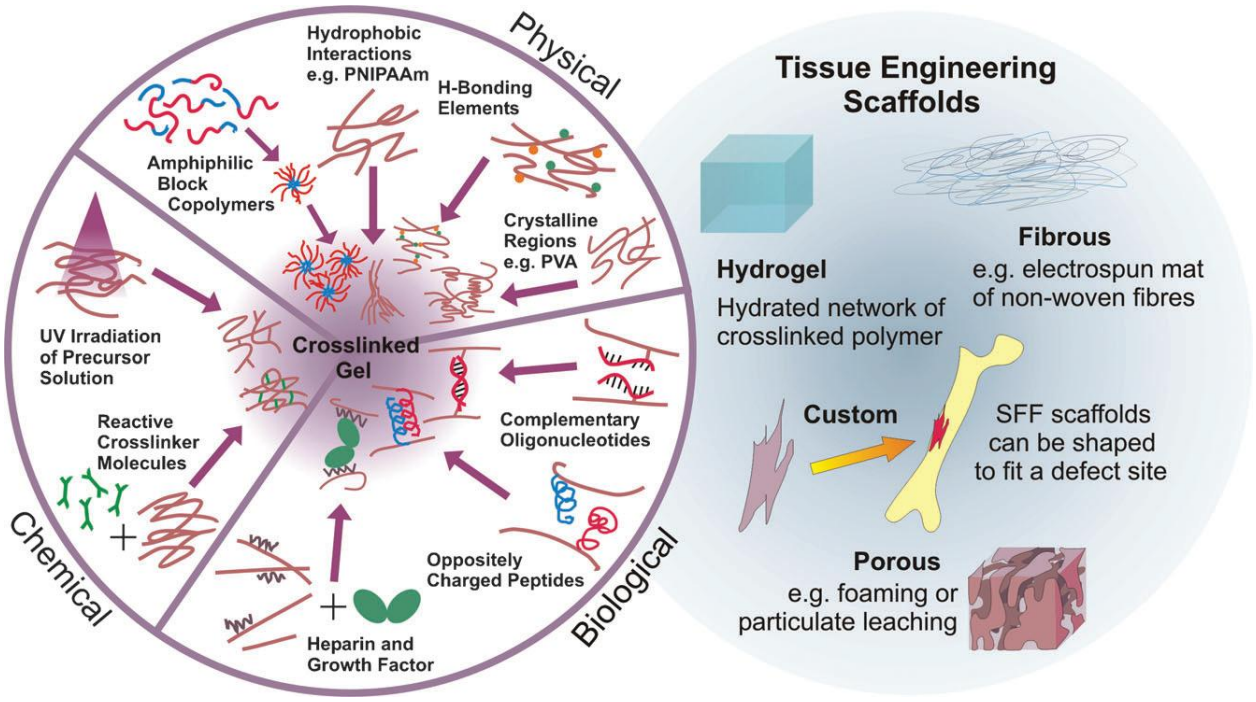

Figure 1.3: Modes of Crosslinking and Scaffold Form Factors. Scaffold materials can undergo a various routes of crosslinking and be made into one of several morphologies. Reproduced with permission from ref. 2. © 2009 The Royal Society of Chemistry.

1.6 Incorporating Nanomaterials with Traditional Biomaterials

The purpose of using secondary materials to form nanocomposites is to supplement the properties that polymeric materials cannot provide. Such nanomaterials confer additional properties, such as mechanical strength, electrical conductivity, and chemical functionalities to aid in cell adhesion and microenvironment modification.[21]

Graphene and carbon nanotubes (CNTs) afford the advantages of improved mechanical strength and electrical conductivity while maintaining biocompatibility of the hybrid synthetic material. Graphene can be thought of as two-dimensional, sheet of carbon atoms arranged in a sp^2 molecular geometry; while CNTs can be thought of as rolled up graphene sheets. Both graphene and CNTs enhance electrical and mechanical properties of hybrid materials, but it is believed that graphene and its derivatives may be more biocompatible, since they have a lower aspect ratio and are not fibre-shaped.[49] Moreover, due to its shape and higher surface area, graphene and its derivatives may be better for cell adhesion.

Nevertheless, work has been done demonstrating their application in tissue engineering; for example, Shin et al. have shown the enhancement in cell adhesion, electrical conductivity and mechanical strength by incorporating CNTs and graphene oxide (GO) into photo-crosslinkable gelatin-methacrylate (GelMa) hydrogels.[32,44,50] It was found that by incorporating CNTs into the hydrogel matrix, the compressive modulus increased from 10 ± 0.5kPa, without CNTs, to 31 ± 2.4kPa. As a point of comparison, the paper referenced highly crosslinked GelMa as having achieved 15-30kPa, although such gels suffer from poor porosity, leading to compromised cell viability.[44] Referring to **figure 1.4**, it is evident that such polymeric matrices have a homogeneously distributed population of carbon nanotubes which promote cell adhesion and spreading.

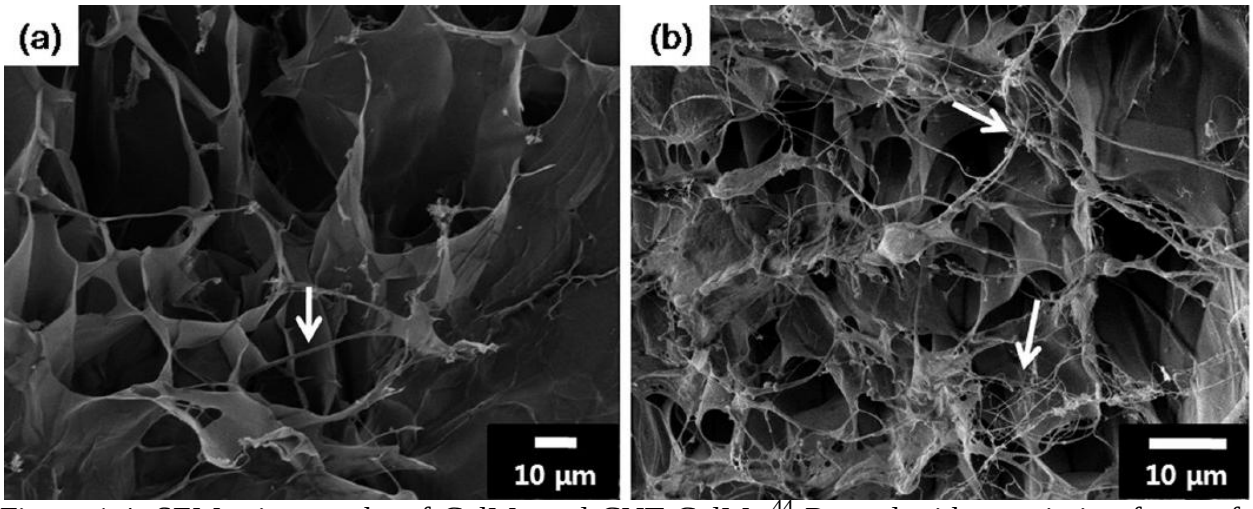

Figure 1.4: SEM micrographs of GelMa and CNT-GelMa.[44] Reused with permission from ref. 44. © 2012 American Chemical Society.

The use of CNTs towards bone tissue engineering has been explored in depth.[51,52] In a particular instance, Shao et al. demonstrated that the nanotopography offered by CNTs in a mixture with poly(lactic acid) promoted the extension and alignment of osteoblasts along the axial direction of the nanotubes, while the application of 100µA direct current had a major effect on further promoting cell elongation and growth, thus conclusively demonstrating the enhanced electrical conductivity over the polymer alone.[53] Numerous studies have shown that the presence of negatively charged functional groups on CNTs attracts calcium cations and leads to the self-assembly of aligned, plate-like hydroxyapatite crystals, not to mention that CNT closely resemble collagen fibers in shape.[51] Following this principle, groups have demonstrated the combination of polymeric materials such as collagen, gelatin and chitosan in conjunction with

HA and carbon nanotubes, thus showing the application of carbon nanomaterials towards bone tissue engineering. By decorating nanofibers with HA nanocrystals, the natural ECM backbone in bone tissue is emulated, where HA crystallites act as adhesion sites for osteoblast cells which in turn generate a higher mineral content in bones.[21,14]

Other instances of using nanomaterials to supplement the properties of polymers include the use of nanotitanate wires and belts to create a more hydrophilic structure with overall higher surface area to promote cell adhesion,[21] and the use of gold nanowires and nanoparticles to improve scaffold conductivity for the purposes of enhancing the bioactivity of encapsulated cardiomyocytes.[30,31] Recently, cellulose nanocrystals have garnered more interest towards applications in tissue engineering, due to its high natural abundance, mechanical properties, low toxicity and the presence of functional groups for covalent modification.[14]

The work described in this thesis explores the synthesis and incorporation of graphene oxide and graphene oxide derivatives as a structurally reinforcing element in hydrogels.

Chapter 2: Synthesis of Iron Oxide-Decorated Graphene Oxide

This chapter summarizes the work done on synthesizing magnetically responsive GO flakes through the decoration of the GO surface with magnetite nanoparticles, and subsequent characterization of the product. The rationale for this work was to incorporate these GO flakes into hydrogels to not only enhance the mechanical properties, but to potentially demonstrate the viability of such nanoparticles as a platform technology allowing response to externally applied magnetic fields. Such a phenomena would be useful in the context of tissue scaffolds and tissue engineering, opening up possibilities for anisotropic enhancement of mechanical properties, influence over cell organization, and *in situ* mechanical actuation on cultured cells.

Some literature review regarding the common synthesis techniques of iron oxide nanoparticles will be provided, along with a summary of the principles of the material characterization techniques typically used to characterize such samples.

2.1 Background on the Synthesis and Characterization Techniques

2.1.1 Synthesis methods of Iron Oxide Nanoparticles

The synthesis of iron oxide nanoparticles has been explored for decades beginning with the study of iron oxide-based ferrofluids in the 1970s, and a wealth of literature and detailed reviews have been published on the topic.[54–56,57] Many synthesis methods have been devised, including microemulsions, sol-gel syntheses, sonochemical reactions, hydrothermal reactions, hydrolysis and thermolysis of precursors, flow injection syntheses and electrospray syntheses. Of these synthesis methods, solution-based chemical synthesis routes are preferred and extensively studied due to their simplicity and ease. Considerable research has been performed to understand the effect of experimental conditions and parameters such that nanoparticle properties (size, shape, chemical composition) can be consistently produced. Such precise control of input parameters is important for high performance applications, especially for biomedical applications such as targeted drug delivery vehicles, magnetic resonance imaging (MRI) contrast agents, and cell labelling and sorting technologies.[54,56]

The most common and simplest method to obtain iron oxide nanoparticles is through the coprecipitation of iron salts, giving relatively high yields. The technique is well established, with

many review papers published about the topic.[55,58–60] Coprecipitation is described by the following reaction equation:

$$Fe^{2+} + 2Fe^{3+} + 8OH^- \rightarrow Fe_3O_4 + 4H_2O$$

According to numerous literature reports, the optimal conditions for obtaining Fe_3O_4 requires a pH in between 8 and 14, a stoichiometric ratio of 2:1 Fe^{3+}/Fe^{2+} in a non-oxidizing environment, otherwise a mixture with maghemite, γ-Fe_2O_3, may be produced. The precipitation of nanoparticles is a kinetically driven process, thus making size control difficult. There are two stages: nucleation in which the solution is quickly brought to supersaturation, usually with a rapid change in pH, which induces the formation of precipitate crystals; and a stage of growth involving the diffusion of solutes to the surface of the nuclei to minimize the surface energy of the high surface area possessed by nanoparticles. The rate of nucleation is driven by the difference in chemical potential between the supersaturated concentration and actual concentration before nucleation, where the solubilities of the iron salts are affected by the ionic strength and pH of the solution.[61] Growth rates depend on factors such as the concentration of salts in solution, and the crystal phases and defects present in the nanoparticle structure. In order to obtain a monodisperse population of nanoparticles, the nucleation and growth stages must be separated, and can be achieved with the addition of capping agents such as small molecules or polymers. Size control can be achieved by changing several parameters including the pH, ionic strength, temperature, nature of the counter-ions (such as perchlorates, chlorides, sulfates, and nitrates) and the concentrations and concentration ratio of Fe^{3+}/Fe^{2+}. Subsequently, nanoparticles are usually stabilized electrostatically and/or sterically to prevent agglomeration after the reaction has completed. This can be achieved with small molecules, such as citric acid, oleic acid, and lauric acid; polymers, such as dextran, alginate, polyethylene glycol and polyvinyl alcohol; or a shell of inorganic material such as gold or silica.

Other popular synthetic methods include thermal decomposition and hydrothermal/solvothermal methods.[54–57] Thermal decomposition involves the use of metal-organic precursors such as $Fe(Cup)_3$, $Fe(CO)_5$ or $Fe(acac)_3$ in a high temperature environment to form iron oxide nanoparticles with controlled size and crystallinity. One of the issues with this synthesis method is the use of organic solvents required to stabilize the hydrophobic nanoparticles, although work has been done to explore the possibility of using alternative solvents and amphiphilic surfactants. In addition, the use of organometallic ligands raises

concerns about the toxicity of the synthesized nanoparticles, however research has been performed on the use of iron chloride salts to synthesize non-toxic nanoparticles.[55] Hydrothermal and solvothermal methods are the most well-established methods for the synthesis of nanomaterials in the laboratory and industrial scale.[62] Hydrothermal and solvothermal methods involve reactions at elevated pressures and temperatures, possibly in excess of 2000 psi and 200°C. In the context of iron oxides, it has been shown that parameters such as the reaction time and temperature can be related to crystal nucleation growth, affecting the size of nanoparticles obtained. The control of nanoparticle morphology has also been explored, by utilizing salts or polymers such as polysaccharides to interact with particular crystal planes to promote the preferential growth along certain planes, although a comprehensive mechanistic explanation remains elusive.[62]

More recent works have demonstrated the possibility of loading iron oxide nanoparticles onto GO sheets using the same synthesis techniques introduced above.[63,64] In such cases, the coprecipitation reaction was carried out in the presence of GO sheets, encouraging the nucleation of nanoparticles on the electron-rich surfaces, leading to the uniform decoration of nanoparticles and an appreciable magnetic response to applied magnetic fields. Although the research was for the purpose of water treatment, the work done demonstrates the dispersibility of GO-Fe_3O_4 composites in an aqueous medium as well as their magnetic response to applied fields. The applications of water-dispersible GO-Fe_3O_4 include magnetic fluids and catalysis.[65] Such composites have also been speculated to be useful for biomedical applications due to the presence of functional moieties and high surface area possessed by GO, affording the potential of multimodal diagnostic or therapeutic functions.[66]

2.1.2 Characterization Techniques for Nanomaterials

Microscopic Characterization Methods

The main electron imaging technique usually used is scanning electron microscopy (SEM).[67] In such a technique, an accelerating voltage in the range of 1-40kV is used to tunnel electrons from the atoms of a filament through a series of electromagnetically focused lenses to provide high resolution and depth of field images. As the electron probe rasters, or scans, across the specimen surface, electrons of varying energies are scattered and detected by the various detectors available on a typical SEM. These scattered electrons originate from different depths of

the sample, and afford different types of information. Of interest are the inelastically scattered secondary electrons (SE), which have a relatively low energy in the range of 3-5keV, and give a representation of the surface topography of the sample. Elastically scattered backscattered electrons (BSE) originate from deeper in the interaction volume, and give information about composition of the sample. Simply put, heavier atoms will deflect more electrons and will appear brighter compared to lighter elements. Thus, the difference between metallic elements and carbon can be easily distinguished. Moreover, the use of energy dispersive x-ray spectroscopy (EDX) can definitively elucidate the elements present in the imaged areas by collecting the characteristic x-rays emitted deep within the interaction volume. Although EDX is not a quantitative analysis technique due to limitations in the detector's calibration, it can still provide an estimate of the elemental composition of regions of interest.

Transmission electron microscopy (TEM) is also used as an imaging technique capable of even higher resolutions. Typically, TEMs reach an accelerating voltage of 100-200kV, resulting in a smaller wavelength (as calculated by the de Broglie equation) and hence better resolution than SEMs. Samples are limited to thin specimens since image contrast is dependent on the deflection of incident electrons as they pass through the sample.[67] For nanoparticle characterization this can usually be achieved by drop casting a solution of the sample onto standard TEM grids. However, for extremely thin samples producing low contrast such as single-layered GO or CNTs, lacey carbon films are preferred.

Occasionally, atomic force microscopy (AFM) is used to characterize surface structure to very high resolution, where atomic resolution has been demonstrated using a variant of the technique called scanning tunneling microscopy.[67] In AFM, a sharp tip typically made of silicon from microfabrication techniques rasters over a sample, detecting changes in intermolecular forces such as van der Waals, electrostatic and capillary forces. The instrument converts the tip deflection over the 2D plane into height-based data. Depending on the operating mode the magnitude of these forces varies, and the resulting topography inferred by the instrument thus heavily depends on the operational parameters set by the operator. In addition to the topography, AFM can record the lead and lag between the piezoelectric material applying a strain and the resulting deflection from the cantilever. This "phase" data is useful for understanding the viscoelasticity of the sample and yields information about the material composition and any adhesion or frictional forces acting on the tip as it passes over particular areas of the sample. In

graphene-based composites, analysis of graphene flakes is relatively easier than composites composed of graphene flakes decorated with nanoparticles, since a rough topography with drastic changes in height (which can be quantified by the root mean square of the height) makes it difficult for the AFM tip to properly track the surface.

Spectroscopic Characterization Methods

This section will elaborate on Raman and Fourier Transform Infrared (FTIR) spectroscopy, in other words techniques utilizing incident radiation in the infrared range. Within this range, electromagnetic radiation has enough energy to excite the vibrational modes between two atoms in a molecule usually described as a simple harmonic oscillator. FTIR is based on the absorption of the incident IR that has specific energy to excite a particular vibrational mode.[67] Thus, by acquiring a spectrum and identifying the energies that exhibit increased absorbance, diatomic bonds corresponding to functional moieties of the sample can be identified.

Raman spectroscopy involves studying the interaction of incident radiation with the sample of interest. Most of the radiation is elastically scattered (Rayleigh scattering), but a small percentage interacts with the sample and excites the vibrational states. The resulting inelastically scattered radiation (Raman scattering) has a slightly different energy than the incident radiation, equivalent to the energy needed to excite the particular vibrational state. Most of the incident photons will promote a molecule's vibration to a higher energy state such that the detected photon has a lower energy (Stokes shift), whereas a small percentage of photons interact with a molecule such that the vibrational energy state is lowered and the scattered photon has a higher energy (anti-Stokes shift). Raman spectroscopy records the intensity of the inelastically scattered photons as a function of the energy shift, or Raman shift.

X-ray Diffraction

X-ray diffraction (XRD) is used to identify chemical compounds by determining the crystal structure.[67] By accelerating electrons in a high-voltage field at a metal target, electrons in the inner shell of the metal atoms are excited to a higher energy state, leaving vacancies. Vacancies in the inner shell will be filled by outer electrons, leading to the emission of characteristic x-rays which probe the sample of interest. Crystal planes become evident due to

constructive interference at certain incident angles, and interplanar spacing can be calculated by Bragg's Law:

$$n\lambda = 2dsin\theta \qquad (1)$$

where n is an integer, λ is the wavelength of the characteristic x-rays, d is the crystal plane spacing, and θ is the incident angle. The most common x-ray source is Cu K_α radiation, which has a characteristic wavelength of 1.542Å.[67]

XRD can be used to identify the oxidation state of synthesized iron oxide nanoparticles by comparing acquired spectra with a database of published XRD data. In addition, by analyzing the full-width at half maximum (FWHM) of characteristic peaks as a direct result of peak broadening due to crystallite size, an estimate of nanoparticle size can be calculated by the Scherrer equation:

$$L = \frac{0.94\lambda}{Bcos\theta} \qquad (2)$$

where L is the dimension of the crystals, λ is the wavelength of the characteristic x-rays, B is the FWHM in radians, and θ is the incident angle in radians.[68] The equation was derived for cubic crystals, but is a good approximation for non-cubic crystalline materials.

Superconducting Quantum Interference Device

A superconducting quantum interference device (SQUID) is a sensitive magnetometer that can measure small magnetic fields. SQUID is used in determining the synthesized material's saturation magnetization, M_S, which is the sum of the magnetic moments of the atoms in a given mass, and whether there is any remnant magnetization, M_R, revealing the magnetic behaviour of the synthesized material.[60] These quantities are usually expressed in units of emu/g. Another property often calculated is the magnetic susceptibility, χ, which describes the linear relationship between the applied magnetic field, H, against the magnetization of the material, B. The magnetic susceptibility is important in both the magnitude (slope) and the sign (positive or negative). Materials with positive susceptibility are paramagnetic, where the magnetic domains align in the same direction as the applied magnetic field, whereas materials with negative susceptibility are diamagnetic, where the magnetic domains align antiparallel to the applied magnetic field. Magnetite may be ferrimagnetic or superparamagnetic depending on the particle

size. Overall, SQUID can reveal the magnetic response of the nanomaterial in response to an applied magnetic field.

Dynamic Light Scattering

Dynamic light scattering (DLS) is a commonly used method to determine particle sizes within a colloidal suspension. The technique involves the use of an incident light beam which enters the sample chamber and interacts with the particles, leading to the scattering of light in all directions. Since particles are always diffusing due to Brownian motion, the interference experienced by the incident beam fluctuates over time, where relatively larger particles diffuse slower. The instrument observes the fluctuations of scattered light at a fixed angle relative to the incident light. The time-dependent fluctuations in the intensity of scattered light can then be related to the distribution of diffusion coefficients causing this interference through the generation of a correlation function by the software. This is then converted into a readout giving information about the distribution of particle sizes. Typically, the Stokes Einstein equation is used:

$$R_H = \frac{k_B T}{6\pi\eta D_T} \qquad (3)$$

where R_H is the hydrodynamic radius, k_B is the Boltzmann constant, T is the temperature, η is the solvent's viscosity and D_T is the diffusion coefficient.[69] In the context of this research project, DLS allows a rough determination of particle size as a quick and non-destructive technique, although it is important to emphasize that the hydrodynamic radius of a nanoparticle assumes that the sample shape is spherical, and includes the shell of hydration from the solvent-nanoparticle interaction. This information is useful towards elucidating the nanoparticle size yielded by predetermined reaction conditions, as well as nanoparticle size stability in various buffer solutions over time.

2.2 Materials and methods

Synthesis of graphene oxide

Natural graphite (Sigma, +100 mesh) was chemically exfoliated by a modified Hummers' method.[70,71] As-purchased graphite (~10g) was ground in a mortar and pestle in the presence of

NaCl (~30g, EMD) to reduce the graphite grain size to allow for easier intercalation of subsequent reagents. Ground graphite flakes (3.0g) were dispersed 70mL of H_2SO_4 (95.0-98.0%, Sigma) and physically expanded upon the addition of $NaNO_3$ (1.5g, Sigma) and $KMnO_4$ (15.0g, EMD), which intercalate in between the graphene layers. The addition of potassium permanganate to sulfuric acid is an exothermic process and must be carried out in an ice bath with vigorous stirring, otherwise the formation of explosive manganese (VII) oxide may be formed.[65] Following the addition of $KMnO_4$, the reaction was allowed to stir at 40°C for 2h, whereupon the solution gradually thickened and turned brown indicating the oxidation of graphite. At the end of this period, the reaction mixture was diluted with 140mL milliQ water (18MΩ cm^{-1}), resulting in violent effervescence. The reaction was allowed to stir at 95°C for 1h. Graphite was oxidized and exfoliated upon the addition of milliQ water and heating to 90°C for 1h. At the end of the reaction, the graphite oxide was diluted with milliQ water and 20mL H_2O_2 (30.0wt%, Sigma) to reduce residual permanganate and manganese dioxide into a colourless and soluble manganese sulfate.[70] At this point the supernatant turned into a vibrant yellow colour. The product was purified to remove trace metals by centrifugation (10min, 12,000g), followed by washing with 5% HCl twice and milliQ water twice. The pellet was retained after each wash. Subsequently, the collected graphite oxide was exfoliated by sonication (40min,Branson 2510) to yield single-layer graphene oxide. The solution was centrifuged (10min, 3200g, Beckman Coulter Allegra X-12R) at least six times, collecting the supernatant each time to separate unreacted graphite and residual graphite oxide. The solution was dialyzed against milliQ water for one week (12-14kDa MWCO, Spectrum Labs). The concentration of the synthesized GO was determined by filtering 5.0mL of stock solution through a membrane filter (0.02µm pore size, Al_2O_3 Anodisc™, Whatman) and weighing the mass of the resulting dry film, usually resulting in a stock concentration of 5 to 6mg/mL. The stock solution was kept under ambient conditions until further use.

Synthesis of graphene oxide-magnetite (GO-Fe_3O_4) composite by co-precipitation method

GO-Fe_3O_4 hybrid material was synthesized by the co-precipitation adapted from Chandra et al.[63] In a typical synthesis, 100mg of GO was diluted using milliQ water to a total volume of 90mL and left stirring in a 3-necked flask. $FeCl_3 \cdot 6H_2O$ (1351.6mg, EMD) and $FeCl_2$ (316.88mg, anhydrous, Sigma) were dissolved in 10mL milliQ water and added slowly to the stirring GO

solution, such that the final salt concentrations were [Fe^{3+}] = 50mM and [Fe^{2+}] = 25mM in a 100mL reaction volume. The reaction flask was purged with house nitrogen for 30min using a flow meter and bubbler filled with silicone oil to ensure a constant inflow of nitrogen with no backflow. The pH was adjusted to 10 with the addition of 2mL of NH_4OH (28.0-30.0%, Sigma), resulting in the reaction mixture turning black immediately. The reaction was allowed to stir for 30min. Following this, the product was centrifuged and washed 4 times to neutralize the base (20min, 3200g, Beckman Coulter Allegra X-12R). Nanoparticles requiring drying for characterization were then washed twice in reagent alcohol (Fisher Scientific) to dehydrate the sample, followed by drying in a vacuum at room temperature. Nanoparticles intended for use as a suspension were mixed with a surfactant to maintain colloidal stability. The precipitation of magnetite nanoparticles (Fe_3O_4) was performed using the same procedure and quantities of reagents, in the absence of GO.

Synthesis of GO-Fe_3O_4 by thermal decomposition method

GO-Fe_3O_4 was also synthesized by a thermal decomposition method following the method of He and Gao.[65] A solution of NaOH (200mg, Sigma) was prepared in diethylene glycol (DEG) (20mL, ≥99.0%, Sigma) to a final concentration of 10mg/mL, with heating at 120°C for 1h to accelerate dissolution. GO (60mg) was freeze dried to remove trace amounts of water and redissolved with 50mL of DEG with vigorous stirring and sonication. When the GO was completely dissolved, $FeCl_3 \cdot 6H_2O$ (400mg, EMD) was added slowly. The reaction was purged with house nitrogen for 30min, then the flask was heated to 220°C using a heating mantle under reflux, allowing 2h from the onset of the temperature ramp for the reaction temperature to equilibrate. 10mL of the NaOH solution (i.e. 100mg) was added to initiate the reaction, allowing it to stir overnight. The product was then washed at least four times with milliQ water to replace the DEG (20min, 3200g, Beckman Coulter Allegra X-12R).

Characterization of materials

Scanning electron microscopy (SEM) experiments were performed on a Zeiss Leo 1530, typically at an accelerating voltage of 5kV when operating in secondary electron mode. The samples of GO were prepared by drop casting a diluted solution onto (3-aminopropyl)triethoxysilane (APTES)-modified silicon wafers. Briefly, wafers were cleaned

with piranha solution (3:1 fuming sulfuric acid/hydrogen peroxide), which also converts the silicon dioxide into silanol groups. After neutralization, wafers were submerged into a solution of 1v/v% APTES (Sigma) diluted in reagent alcohol and allowed to react for 30min. The wafers were then cleaned with multiple ethanol washes with very mild sonication to wash off unreacted APTES. Wafers were dried and kept in an inert atmosphere until needed. Transmission electron microscopy (TEM) was carried out on a Philips CM10 instrument, operating at 60kV. Samples were diluted in ethanol or water, depending on solubility, and drop cast onto 200 mesh copper grids with a carbon-formvar coating (1nm thick carbon, 10nm thick formvar, supplied by Electron Microscopy Sciences). Atomic force microscopy (AFM) was performed on a Veeco Nanoscope MultiMode instrument, operating in tapping mode using a cantilever with a resonance frequency of approximately 300kHz. Scans were taken at a line rastering speed of 1.5Hz. Samples were deposited on freshly cleaved mica (Ted Pella Inc.). Dynamic light scattering (DLS) was performed on a Malvern ZS90 equipped with a 633nm laser. The scattering angle was 90°, and the temperature was equilibrated to 25°C before scanning. Samples were prepared and diluted in water. For Fourier Transform Infrared (FTIR) spectroscopy, samples were ground in a mortar and pestle with IR spectroscopy grade KBr (Fisher Scientific) and compressed into pellets (Carver pellet press). Scans were performed on a Bruker Tensor 37 FTIR spectrometer from 400 to 4000cm^{-1} averaging over 16 scans. Raman spectroscopy was performed on a Horiba Jobin Yvon LabRAM HR 800 Raman spectrometer using a 633nm laser. The recorded data was averaged over 2 scans, and the laser power and scan duration were increased until an acceptable signal intensity could be acquired. UV-Vis spectroscopy was performed on an Agilent 8453 UV-visible Spectroscopy System with quartz cells. Powder x-ray diffraction (XRD) experiments were performed on a Bruker D8 Advance diffractometer equipped with Cu K_α radiation (λ = 1.542Å) or on a PANalytical Empyrean using Co Kα radiation (λ = 1.79Å). For characterization of the GO sample, 5mL of solution had been filtered to form a membrane, and the intact membrane was mounted to a standard aluminum tray with petroleum jelly. Superconducting Quantum Interference Device (SQUID) measurements were made on a Quantum Design SQUID-VSM Magnetic Property Measurement System (MPMS). The instrument parameters were set to scan at least one complete cycle to check for hysteresis, at 300K up to 5T magnetic field. Thermogravimetric analysis (TGA) experiments were performed on a TA Instruments SDT Q600 instrument. GO-Fe_3O_4 and Fe_3O_4 were dried under vacuum at

room temperature, GO was freeze dried. Samples were then crushed in an agate mortar and pestle to ensure sufficient contact with the purge gas. Samples were loaded (5 to 10mg) into an alumina crucible, and run with air as the purge gas (100mL/min) with a temperature ramp of 5°C/min. The oven was set to ramp up to 100°C and hold at isothermal conditions for 30min, and the temperature ramp was subsequently resumed at 5°C/min to 800°C.

2.3 Results and discussion

2.3.1 GO material characterization

GO was synthesized using a modified Hummers' method. Upon completion of the reaction and purification procedure, the nanoparticle suspension remains stable for months, with evaporation being the only concern in regards to nanoparticle aggregation. The final product appears to be a brown, somewhat gold, solution. It was observed that the concentration of the stock solution depended heavily on the sonication time, and by extension the sonication power, used to exfoliate graphite oxide into graphene oxide. The yield was optimized by using a sonication duration which maximized graphite oxide exfoliation without causing structural damage to the GO flakes, a phenomenon which was also observed in some batches of GO. For higher stock concentrations, a milky texture was observed. This can be easily mistaken for aggregation or precipitation of graphene oxide but is actually indicative of liquid crystal behaviour.[72] The self assembly of GO flakes into liquid crystals require a minimum threshold lateral sheet size and concentration. This self-assembly can be disrupted by ions or acids which interact with GO, causing aggregation or precipitation due to GO's excellent ability to gelate.[73] Thus, the appearance of liquid crystal behaviour actually indicates a contaminant-free working solution.

FTIR confirmed the oxidation of graphene by examining the characteristic peaks associated with the oxygen-containing groups introduced during the reaction (**Figure 2.1a**). Noticeable peaks are attributed to O-H stretching (3438cm^{-1}), C-H alkane stretching (2923cm^{-1} and 2858cm^{-1}), C=O stretching (1722cm^{-1}), C=C stretching (1628cm^{-1}) from the unoxidized graphitic domains, O-H in-plane bending vibration (1384cm^{-1}) usually attributed to adsorbed water molecules, C-OH stretching (1234cm^{-1}), and C-O-C epoxide stretching (1070cm^{-1}).[74,75,7677,78]

Figure 2.1b shows UV-visible absorption spectra for two different batches of GO. The prominent peaks associate with this type of sample is the peak at 230nm and shoulder at 298nm. The peak at 230nm is attributed to the π-π* transition from C=C bonds, and the shoulder is attributed to the n-π* transition from C=O (carbonyl and carboxylic acid groups).[77–80] As such, UV-Vis spectroscopy gives some information about the relative surface area occupied by the aromatic sp^2 carbon basal plane compared to oxygen-containing groups, as well as restoration of the conjugated structure.[80]

Figure 2.1c shows the Raman spectra for graphite and various batches of synthesized GO, after manual baseline correction and normalizing the peak intensity. The most important peaks for these types of samples are the D and G peaks. The D peak is located at ~1330cm^{-1} and G peak is located at 1580cm^{-1} for graphite and 1595cm^{-1} for GO samples. The structural characterization of graphite has been well documented; the G peak corresponds to the first order scattering of the E_{2g} phonon of sp^2 carbon atoms, and the D peak corresponds to the breathing mode of κ-point photons of A_{1g} symmetry.[77,63] Simply put, the G peak arise from sp^2 domains originating from structurally pure graphene, whereas the D peak is associated with structural defects, amorphous carbon and edges which break the symmetry and selection rule. Typically, the presence of oxygen-containing groups and dangling sp^3 bonds will increase the D peak intensity, as well as physical damage to the sheet structure during the harsh oxidation reaction required.

Several inferences can be made from the peak positions and intensities. In general, peak broadening of the D and G peaks as well as a higher D intensity is attributed to structural disorder. As a rough measure of structural purity, the ratio of the D band's intensity over the G band's intensity is calculated (I_D/I_G).[63,77,81] The I_D/I_G for graphite is 0.37, whereas for GO samples the ratio increases to 0.96, 1.01 and 0.92 indicating the presence of more defects in the carbon basal plane after oxidation. The shift in the G peak's position for GO samples can also be explained.[77] The broadening and shifting of the G peak to higher frequency indicates the creation of isolated C=C bonds during the oxidation process, since such bonds vibrate at higher energies. Overall, it can be shown Raman spectroscopy that the oxidation reaction as part of Hummers' method breaks up the structural symmetry of the sp^2 lattice of graphite, due to the introduction of oxygen-containing groups and more edge defects.

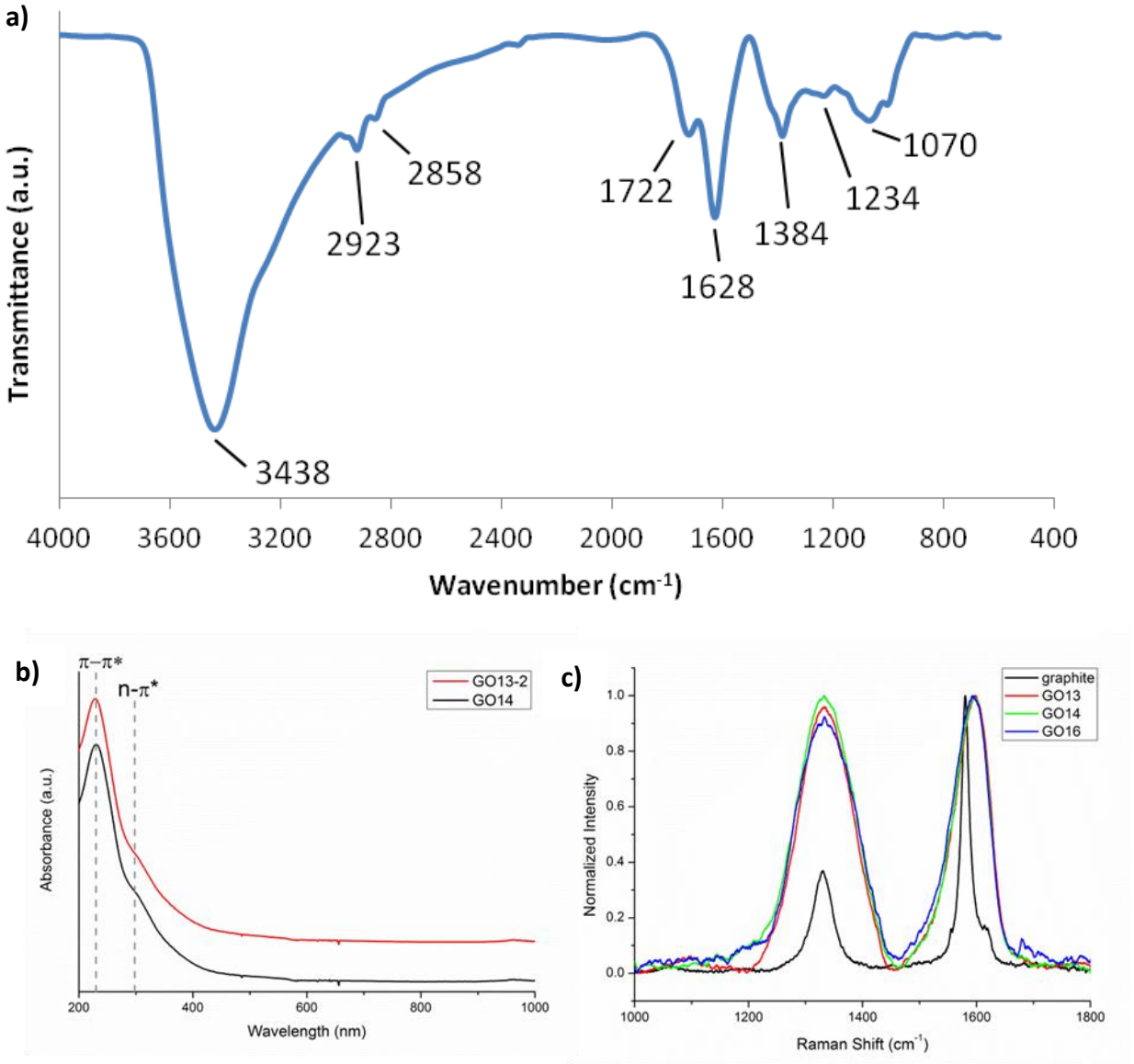

Figure 2.1: Spectroscopic characterization of GO. a) FTIR spectra for two different batches of GO. b) UV-Visible absorption spectra for two different batches, plotted with a vertical offset to each other. GO was diluted to 0.015mg/mL in milliQ water. c) Raman spectra for graphite and various batches of GO. Acquired spectra were corrected with a manually selected background and normalized using the G band.

The properties of GO were also characterized by microscopy techniques. **Figure 2.2a** shows an AFM image of GO, which has a size distribution ranging from hundreds of nanometres to several microns. The average sheet thickness is ~1nm, and can be corroborated by numerous reports.[82,81] **Figure 2.2b** shows an SEM image of a graphene oxide sample. This technique is useful for imaging large surface areas in a shorter amount of time. Increased contrast can be seen where GO sheets fold or stack, but the shortcoming of the SEM is that it is not capable of

measuring height profiles. Samples were deposited on APTES-modified silicon wafers, although the adhesion of GO onto silicon did not show any appreciable difference compared to bare silicon/silicon dioxide (data not shown).

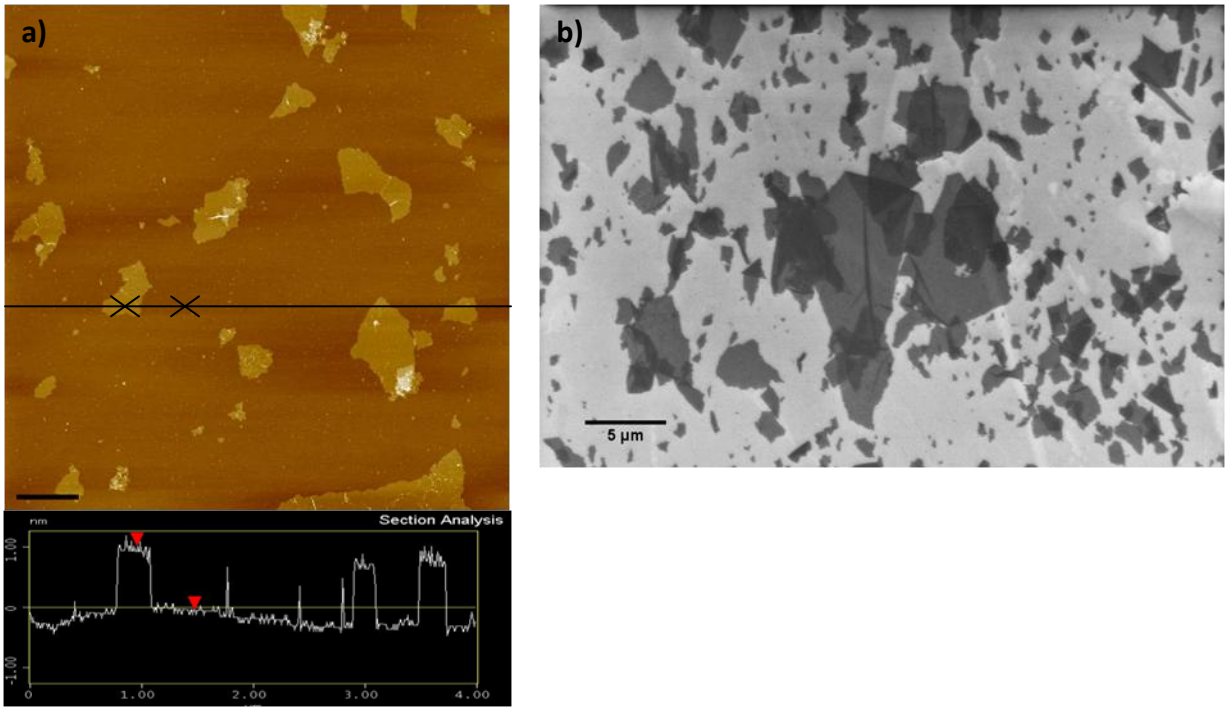

Figure 2.2: Microscopic characterization of GO. a) AFM image obtained in tapping mode, with a height profile. Scale bar is 500nm. b) SEM image showing a larger area.

Figure 2.3 shows a DLS readout showing the number intensity. As mentioned in **Section 2.1.2**, DLS analyzes the diffusion of analytes as they diffuse through solution and represents lateral size as the hydrodynamic radius. The underlying assumption is that the sample analyzed has a spherical shape, and includes a shell of hydration from the interaction with solvent. Therefore, some discrepancy exists between using imaging techniques and an *in situ* analysis technique. In imaging techniques, GO flakes conform to the surface of the substrate they are deposited on, appearing to be rigid flakes. However, GO sheets are highly flexible, and their exact shape in solution is not known.[75] Moreover, DLS is suited to nanoparticles that are known to have a sharp size distribution. On the other hand, GO size distributions are highly polydisperse with a lateral size distribution spanning three orders of magnitude. While it is possible to accurately fit a sample that has a multimodal distribution (up to three sharp peaks) with most

DLS instruments, GO requires special fitting models to accommodate the polydispersity across a very wide range of sizes. In a work by Stankovich et al., isocyanate-treated GO flakes were characterized and fitted using CONTIN analysis.[75] Whereas monomodal samples (a Gaussian distribution centred at one mean size) exhibit a single exponential decay in the autocorrelation data, or bimodal samples (two Gaussian distributions centred at two different mean sizes) exhibit two exponential decays, the CONTIN algorithm was developed to analyse a sample with no prior knowledge about the size distribution and assumes a completely random distribution. This algorithm may be available on certain DLS instrument models or may be applied in offline analysis, but was not in the scope of this project.

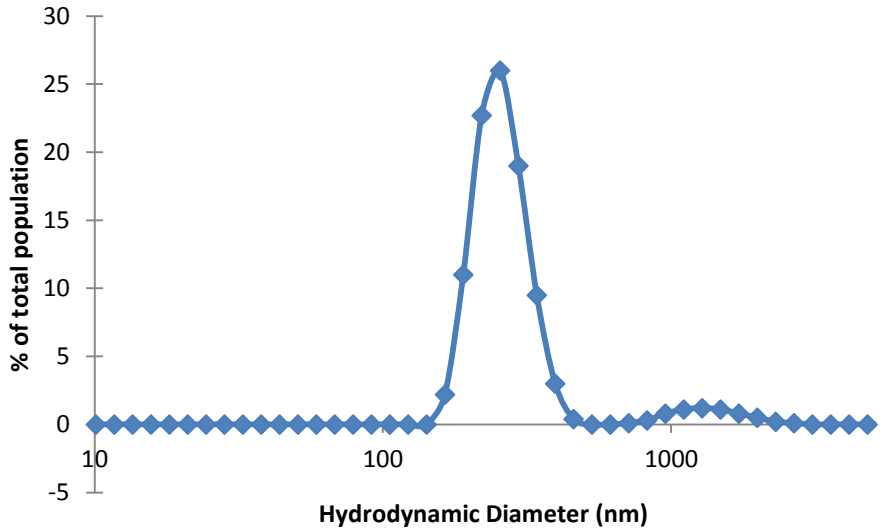

Figure 2.3: GO size distribution measured by DLS, represented as a number distribution.

2.3.2 Characterization of GO-Fe_3O_4 Synthesized by Co-precipitation Method

GO-Fe_3O_4 was synthesized by the co-precipitation method described in **Section 2.2**. Powder x-ray diffraction patterns were obtained for the synthesized product, for co-precipitation reactions carried out in the absence of GO (referred to as Fe_3O_4) and presence of GO (referred to as GO-Fe_3O_4). The synthesized Fe_3O_4 displayed peak positions and relative intensities corresponding to the magnetite crystal structure (Inorganic Crystal Structure Database (ICSD) no. 164814), whereas the GO-Fe_3O_4 product was matched with ICSD no. 031156. The major diffraction peaks can be seen in **figure 2.4a**. The crystallite size can be estimated using Scherrer's equation, and is a good estimate for nanoparticle size if it is a single crystal. Using the

FWHM of the most intense peak for each sample ($2\theta \approx 35.5°$), the crystallite size is calculated to be 15.5nm and 11.8nm for Fe_3O_4 and GO-Fe_3O_4, respectively. It is important to note that iron samples exhibit a fluorescence phenomenon when Cu K_α radiation is used, resulting in a low signal to noise intensity and high background intensity. As a reference, the XRD patterns for graphite and GO films is also included (**figure 2.4b**). Graphite shows a peak at $2\theta = 26.5°$, corresponding to the (002) d-layer spacing of 0.345nm representing the inter-sheet distance. For GO, the peak shifts to 12.1°, or a 0.737nm interlayer distance. This shows that as opposed to atomically flat graphene, GO has oxygen-containing groups and sp^3-hybridized carbon which expand the stacked sheet structure.[82] This feature is not seen in the powder XRD pattern for GO-Fe_3O_4, which was crushed into a fine powder.

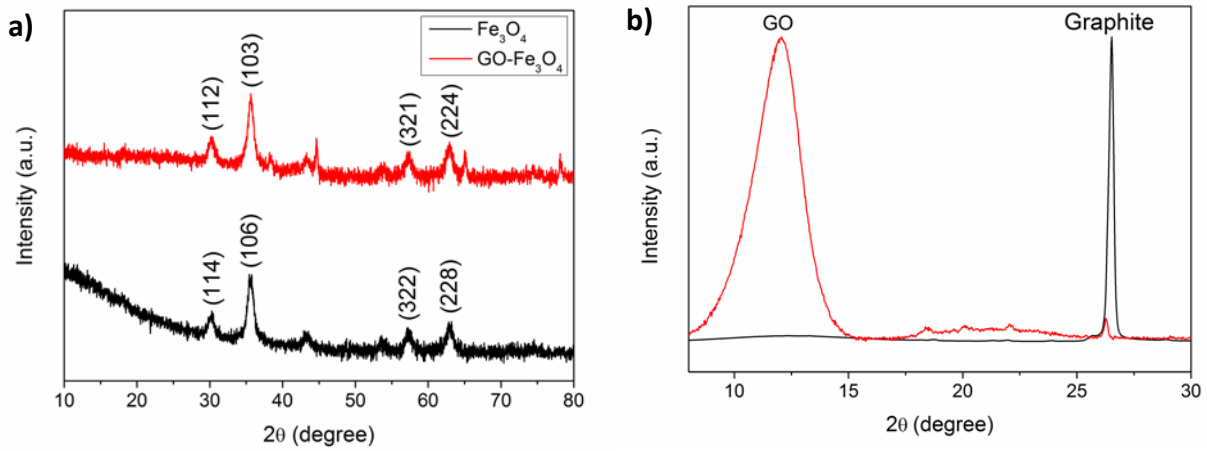

Figure 2.4: XRD patterns of a) Fe_3O_4 and GO-Fe_3O_4, b) graphite and GO as a film. Diffraction patterns were acquired with Cu K_α radiation.

TEM was performed to understand the coverage density and magnetite nanoparticle size grown from this reaction. **Figure 2.5a** shows bare Fe_3O_4 nanoparticles, and **figure 2.5b,c** show GO-Fe_3O_4. The surface coverage of magnetite nanoparticles appears to be low, although high surface coverage resulting in up to several layers of magnetite nanoparticles have been observed (such as in **Figure 2.5c**). Moreover it was observed that magnetite tended to precipitate as bare Fe_3O_4 nanoparticles, not on GO surfaces, resulting in a product that was structurally impure. It has been shown that GO provides an electron-rich environment through the presence of oxygen-containing groups, which act as nucleation sites for nanoparticles[83], which may mean that the ratio of [Fe^{2+}/Fe^{3+}]:[GO] is too high or the nucleation and growth of seed crystals is a poorly controlled process in this type of reaction.

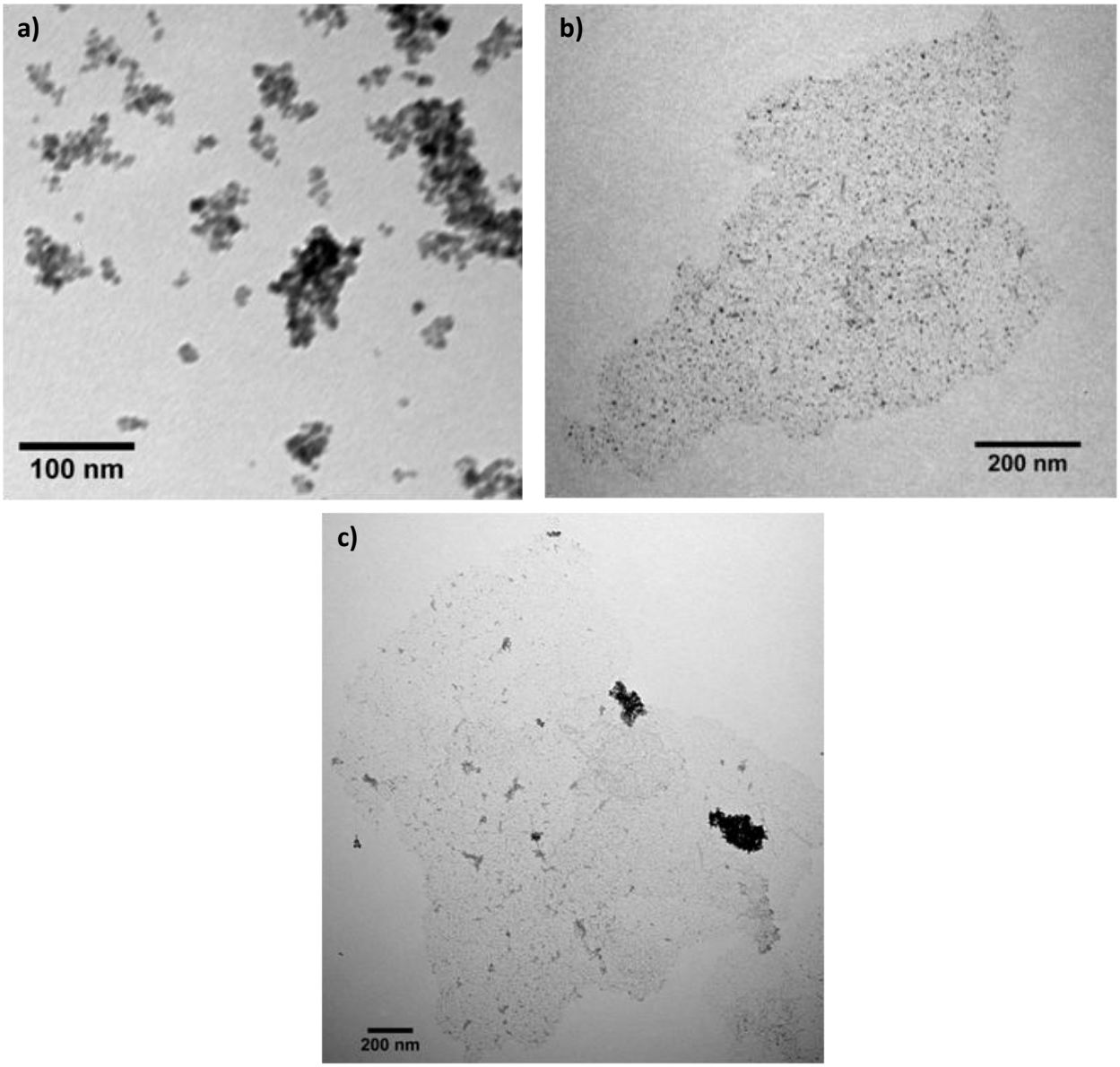

Figure 2.5: TEM images of a) Fe_3O_4 nanoparticles; b) and c) GO-Fe_3O_4.

The magnetic properties of the nanoparticles was studied using SQUID. Magnetic hysteresis curves were obtained at 300K up to 5T (**figure 2.6**). GO-Fe_3O_4 possessed a saturation magnetization of 67.73emu/g and a remnant magnetization of 0.90emu/g; Fe_3O_4 possessed a saturation magnetization of 70.52emu/g and remnant magnetization of 0.91emu/g. This data shows that the synthesized nanoparticles have a high magnetic response and are superparamagnetic, possessing very low remnant magnetization and little hysteresis. Table 1 compares the magnetic properties of the current formulation with recent published works.

Various factors can affect the measured M_S value, and is heavily dependent on experimental parameters such as the specific pH value and presence of surfactant molecules during the precipitation process. These variables contribute to the purity of the crystal structure and the presence of surface defects exacerbated with decreasing nanoparticle size since the relative surface area to volume increases, both of which lower the M_S value obtained. Typically, for Fe_3O_4 nanoparticles, a range of values from 30 to 50emu/g have been reported (compared to 90emu/g for bulk magnetite), and this is largely due to the vast number of studies published with highly variable parameters used.[54,56] The analysis presented describes only a rudimentary understanding of the problem, further studies into the fundamental physical phenomena and relation to the crystal structure needs to be done.

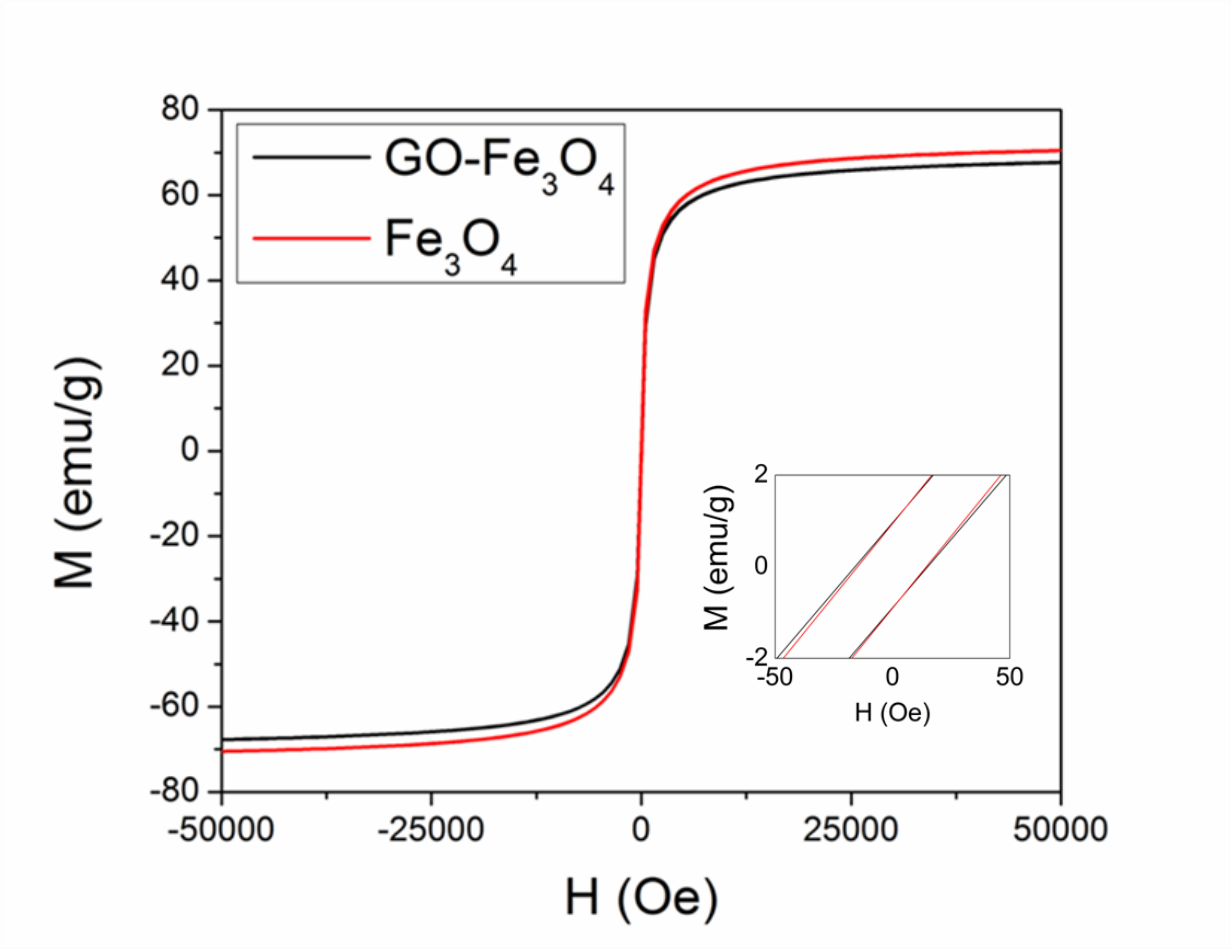

Figure 2.6: Magnetic hysteresis curves for GO-Fe_3O_4 and Fe_3O_4. Inset shows a zoomed-in window to highlight the remnant magnetization and hysteresis.

Table 1: Comparison of M_S values (in emu/g) found in literature, carried out at 300K

Method of synthesis	Fe_3O_4 nanoparticles	GO-Fe_3O_4
Coprecipitation (current work)	70.52	67.73
Coprecipitation (2011)[84]	62	---
Coprecipitation and reduction with hydrazine (2010)[63]	---	59.0
Coprecipitation (2011)[64]	---	31.0
Reduction with hydrazine (2011)[85]	17.96	10.23
Solvothermal synthesis (2013)[86]	60.1	61.2

Regarding the colloidal and chemical stability of the nanoparticles, the Fe_3O_4 and GO-Fe_3O_4 need to be capped with a surfactant to remain colloidally stable due to the propensity of nanoparticles to aggregate to lower surface energy. This is crucial for experiments which subsequently use these nanoparticles as a suspension. Nanoparticles were coated with alginate for hydrogel experiments which will be elaborated upon in **Chapter 3**. As for the chemical stability, magnetite tends to oxidize to hematite (α-Fe_2O_3) in aqueous or oxidizing environments. Regardless of whether there is a surfactant coating, synthesized nanoparticles oxidize over several months, exhibiting the characteristic red colour of hematite, and losing its superparamagnetic response and magnetic susceptibility. In summary, the co-precipitation is a simple method which yields nanoparticles with high magnetic response and colloidal stability, but poor control over nucleation due to the difficulty in separating the nucleation and growth steps involved in crystal growth.

2.3.3 Characterization of GO-Fe_3O_4 Synthesized by Thermal Decomposition Method

The thermal decomposition method was performed in order to obtain GO-Fe_3O_4 with uniform and preferential deposition of magnetite on to GO surfaces, resulting in a product with high magnetic response and pure structural properties. The original protocol was promising, having demonstrated slow and controlled crystal growth. It was hypothesized that the crystal growth followed the LaMer model, were seed crystals were quickly precipitated, followed by a diffusion-controlled growth process governed by the Lifshitz-Slyozov-Wagner theory relating to Ostwald ripening. As a result, nanoparticle size grew linearly (in terms of nm^3/min) with particle growth rate reaching a plateau at about 24 hours.

The method was attempted, yielding good results. The decoration of nanoparticles was very uniform, as was the particle size distribution (**figure 2.7a**). In addition, XRD using Cu K_α radiation yielded quite high signal to noise ratio compared to the results obtained with the co-

precipitation method (the scan times were kept constant at 30min), which could indicate higher crystallinity of the Fe_3O_4 structure (**figure 2.7b**).

Macroscopically and microscopically (**figure 2.7c and d**), it was observed that this method produced an aggregated product, which can be explained by the fact that DEG was heated to 220°C, which is very close to its boiling point. Over the course of the reaction, the solvent evaporates and recondenses, which causes the nanoparticles at the solvent-air interface to aggregate. This observation can be supported by others, such as in Li et al.'s work in graphene suspensions.[87] The original protocol did not use any surfactant and did not report excessive aggregation, although their work did not require well dispersed nanoparticles, such as is required for this project. The use of alginate as a surfactant was attempted. However, since alginate is not soluble in DEG, it could only be added after the reaction was completed. Even with extended sonication in the presence of alginate, the aggregated GO-Fe_3O_4 could not be resuspended. Hence, although this method produces highly crystalline and monodisperse Fe_3O_4 crystallites, the overall product was not colloidally stable over the duration of the experiment, which is a requirement for their use in nanoparticle-incorporated hydrogels.

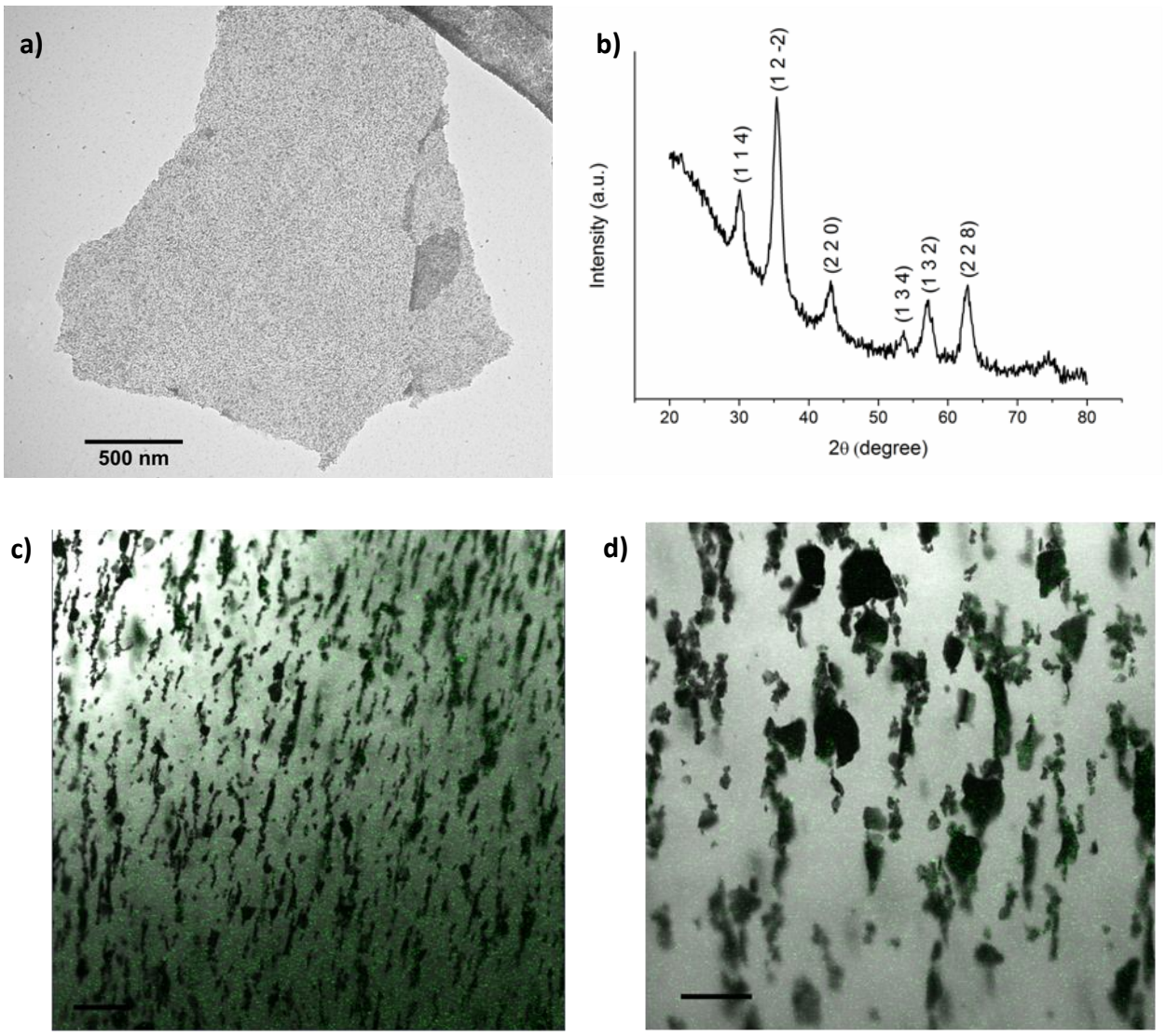

Figure 2.7: Characterization data for GO-Fe_3O_4 synthesized by thermal decomposition. a) TEM image of GO-Fe_3O_4 after a 12 hour reaction. b) XRD pattern of GO-Fe_3O_4 after a 3 hour reaction. c) and d) GO-Fe_3O_4 nanoparticles in a 1w/v% alginate hydrogel, captured with a fluorescence microscope. Scale bars, c) 100µm and d) 50µm.

2.3.4 Characterization of GO-Fe_3O_4 Synthesized by Revised Co-precipitation Method

In a second attempt to produce GO-Fe_3O_4 that was colloidally stable and had a high but not excessive coverage of magnetite particles on GO, the co-precipitation method was repeated with modified quantities of ferrous chloride and ferric chloride. Keeping the other reagent quantities the same, iron salt concentration was reduced to [Fe^{3+}] = 12.5mM and [Fe^{2+}] = 6.25mM to react with 100mg. **Figure 2.8** shows representative TEM images, where the

decoration of magnetite onto GO sheets is more controlled, but the size distribution is not as uniform as the thermal decomposition method.

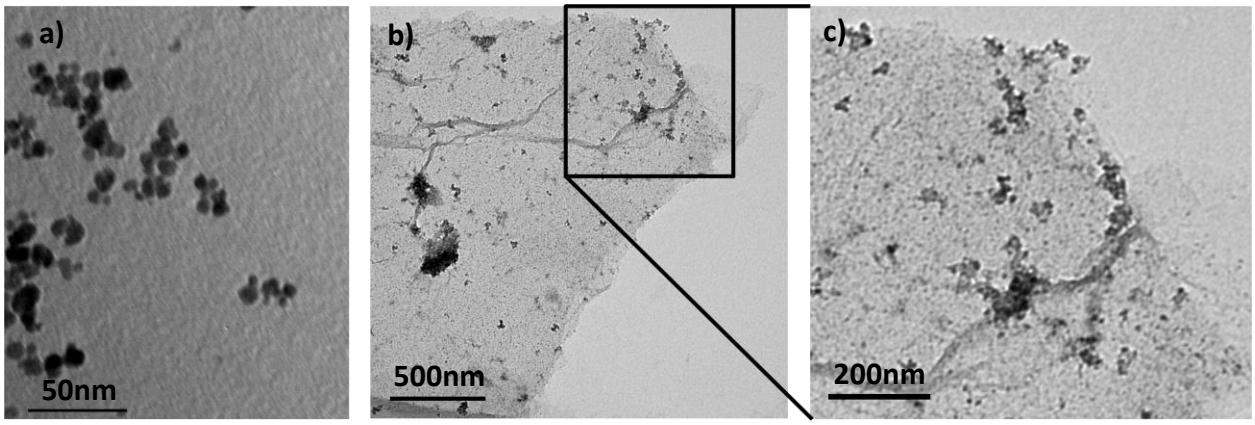

Figure 2.8: TEM images of a) Fe_3O_4 nanoparticles; and b) GO-Fe_3O_4. c) is a higher magnification image of b).

XRD was also performed on the new sample, using Co K_α radiation to obtain a better signal to noise ratio. **Figure 2.9** shows the acquired diffraction pattern for Fe_3O_4 and GO-Fe_3O_4 synthesized with the new ferrous and ferric salt concentrations. The diffraction pattern for Fe_3O_4 shows increased signal to noise due to the absence of the x-ray fluorescence phenomenon that was observed with using a copper source. The peak intensities indicates good crystallinity, as should be expected. With the GO-Fe_3O_4 sample however, the peak intensities are weak, although the peaks are in the correct positions. It can only be hypothesized that the Fe_3O_4 in this formulation are amorphous leading to the scarcity of crystal planes to diffract the x-rays at characteristic angles, or that the material has extremely small crystallite size causing increased peak broadening. However, peak broadening as a direct consequence of crystallite size should not affect the poor signal intensity of diffracted peaks, in addition it has been shown that co-precipitation produces relatively poor crystallinity. Hence, it is more likely that the poor signal intensity is due to a somewhat amorphous structure. Macroscopically, the magnetic behaviour has been verified to be weaker than with GO-Fe_3O_4 synthesized with the original formulation ($[Fe^{3+}]$ = 50mM, $[Fe^{2+}]$ = 25mM).

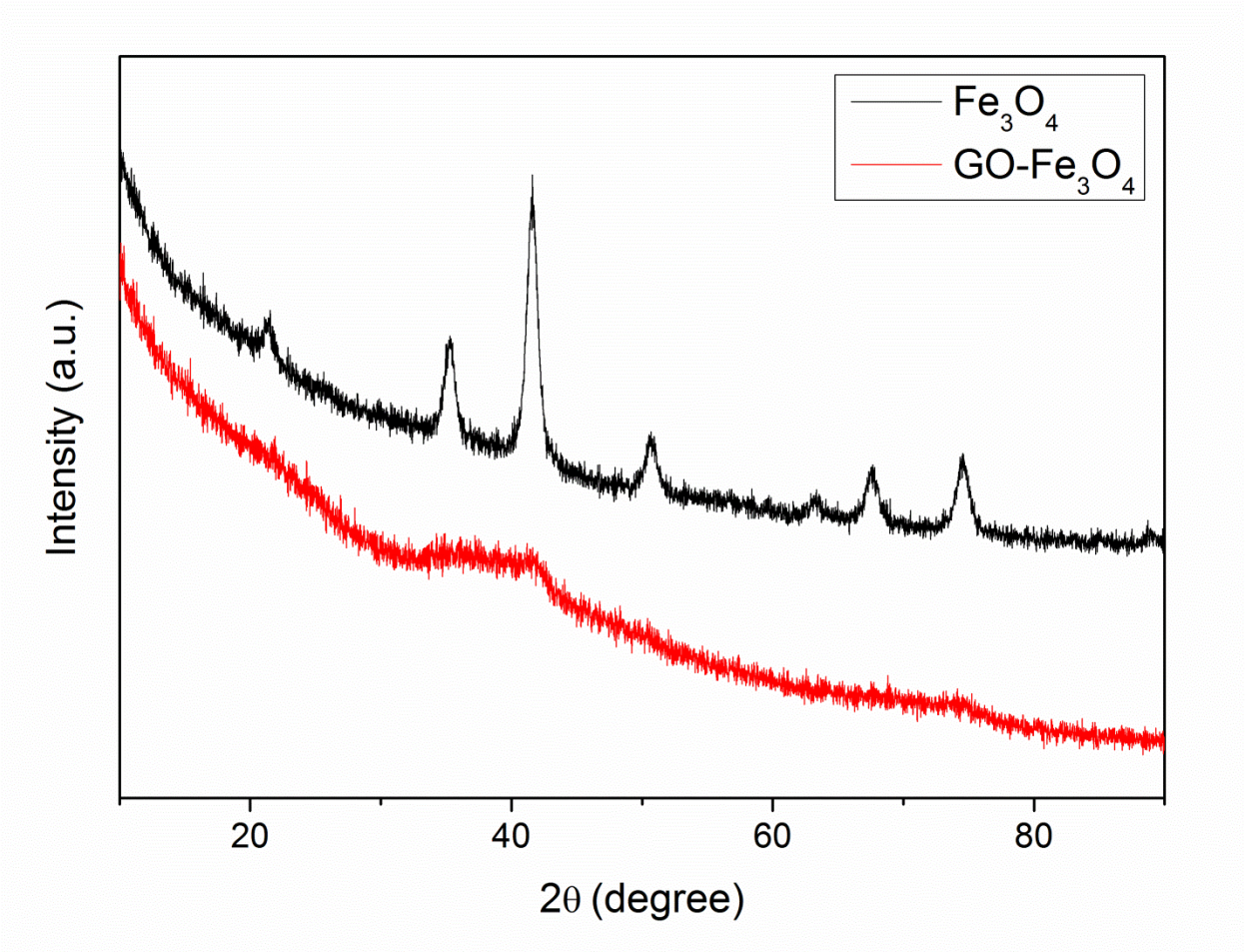

Figure 2.9: XRD patterns for the new co-precipitation formulation, using Co K_α radiation.

SQUID analysis was performed on the new formulation (**figure 2.10**). GO-Fe_3O_4 possessed a saturation magnetization of 24.2emu/g and a remnant magnetization of 1.16emu/g; Fe_3O_4 possessed a saturation magnetization of 74.5emu/g and remnant magnetization of 2.95emu/g. There was minimal change in the magnetic properties of the Fe_3O_4. For GO-Fe_3O_4, the saturation magnetization showed a significant decrease, due to the lower loading of iron, and poor crystallinity of the magnetite crystal structure as elucidated by XRD.

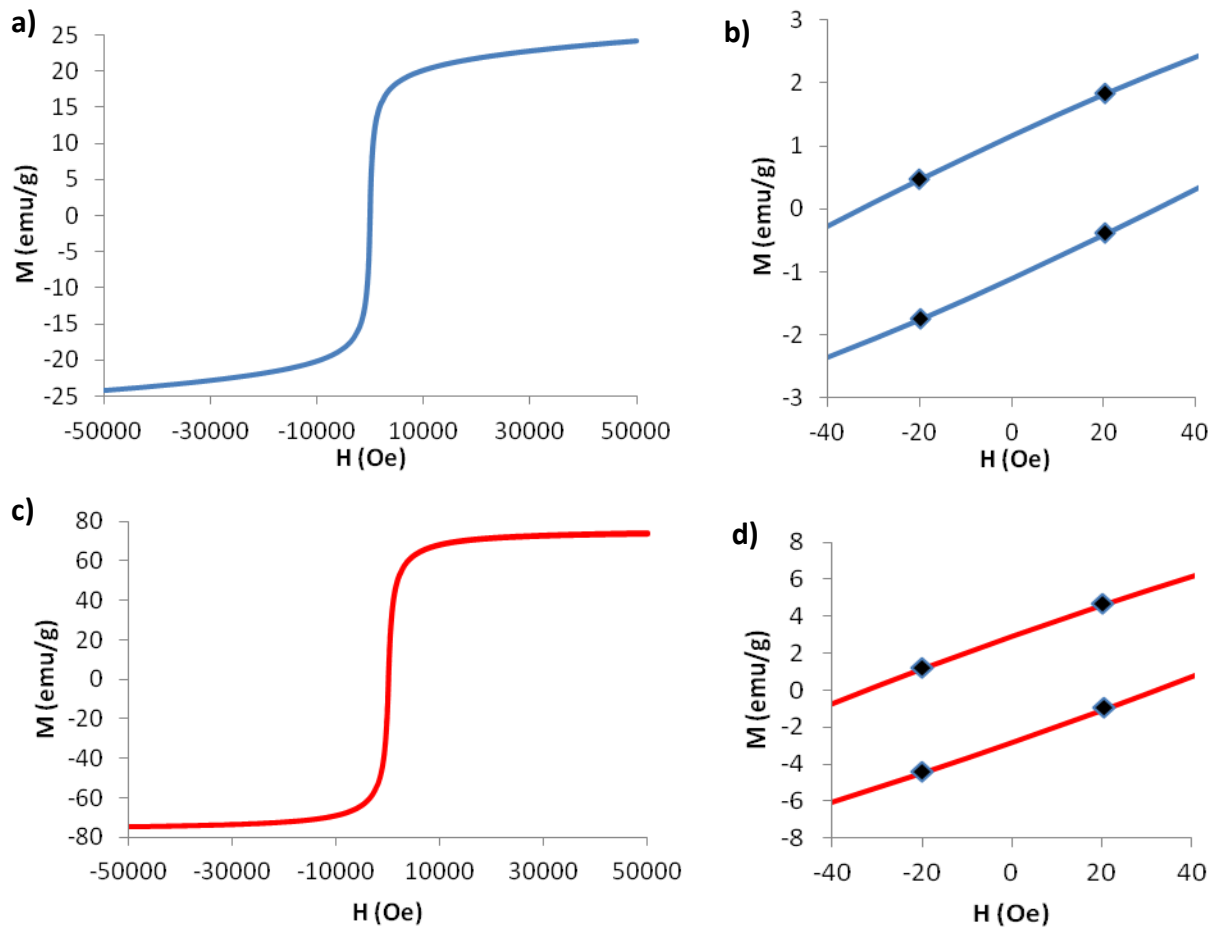

Figure 2.10: Magnetic hysteresis curves for GO-Fe_3O_4 (a and b) and Fe_3O_4 (c and d). b) and d) are zoomed-in windows to highlight the remnant magnetization and hysteresis.

Thermogravimetric analysis (TGA) was performed to quantify the relative mass ratios of graphene oxide and iron oxide, as a measure of the iron oxide loading. **Figure 2.11** shows the resulting heating curve for Fe_3O_4, GO, and GO-Fe_3O_4. The GO sample in this case was treated with NH_4OH under the same conditions as the co-precipitation procedure to eliminate any variances in the chemical structure of GO that could have occurred during the reaction. In general, samples were heated to 100°C from room temperature at a rate of 5°C/min and held at isothermal conditions to allow any adsorbed water to be purged, in order to separate thermal events, which can be examined using the Differential Thermal Analysis functionality of the instrument (data not shown). The mass percentage of adsorbed water can be large, especially for GO which is very hydrophilic, so it was imperative to allow this moisture to desorb to accurately

calculate the mass contribution from iron oxide and graphene oxide. The heating ramp was then resumed at 5°C/min until 800°C.

For the analysis of Fe_3O_4, it was expected that some water would be lost by desorption. At 270°C, magnetite oxidizes to maghemite (γ-Fe_2O_3) and further into hematite (α-Fe_2O_3) reaching completion at about 320°C.[88] The oxidation process causes an increase in mass. Overall, the Fe_3O_4 lost about 2.91% mass. The GO sample undergoes two main decompositions after residual moisture has desorbed. At 150-200°C, oxygen-containing groups are removed, generating CO, CO_2 and steam.[89,90] This is followed by the decomposition of the remaining carbon lattice at 450-500°C resulting in no remaining mass.[91] For the GO-Fe_3O_4 sample, the same thermal decompositions as the GO sample are observed (the decomposition of the carbon lattice appears to occur at an earlier onset temperature), such that any remaining mass is attributed to hematite.

The mass contribution of iron oxide can then be calculated. The final mass of the GO-Fe_3O_4 is 62.6%, and is assumed to be composed of iron oxide. By applying the correction factor to account for the small percentage of mass lost in a pure iron oxide sample (2.91%), the original mass composition can be calculated as 64.5%. Hence, the mass ratio of GO : Fe_3O_4 is 0.355 : 0.645. This was the ratio used in the preparation of GO-Fe_3O_4 incorporated hydrogels.

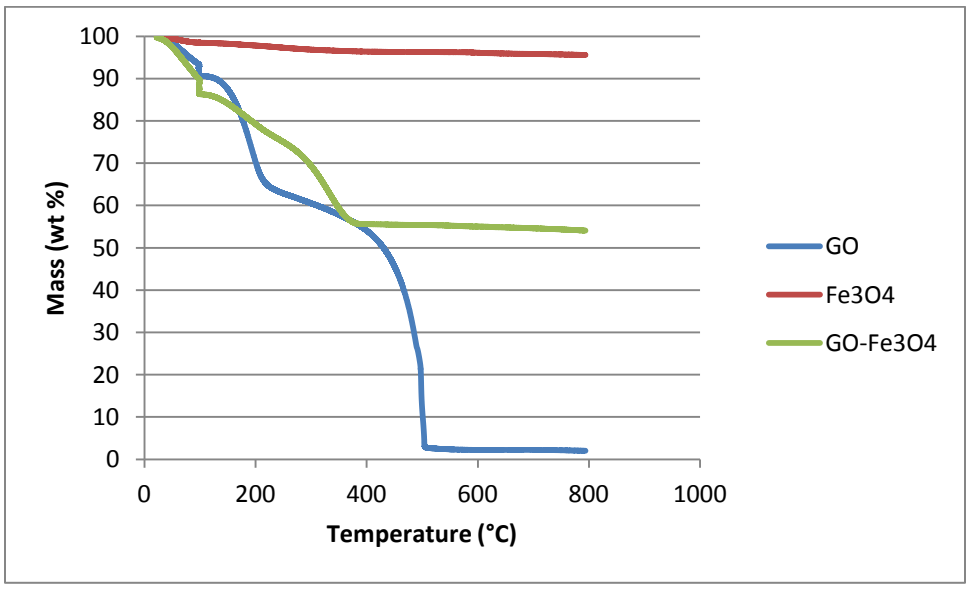

Figure 2.11: TGA curve for GO, Fe_3O_4 and GO-Fe_3O_4, with air as the purge gas.

2.4 Conclusions

Graphene oxide was synthesized and shown to be a chemically and structurally pure through various forms of characterization. Graphene oxide was then decorated with magnetite nanoparticles using a few methods. In the co-precipitation route, graphene oxide decorated with a higher loading of nanoparticles exhibited appreciable magnetic response and was superparamagnetic at room temperature. However, the shortcomings of this method is that the crystallinity of the magnetite tends to be relatively lower compared to methods such as thermal decomposition. Also, the nucleation of nanoparticles was not very well controlled, as imaging techniques revealed the precipitation of magnetite on GO surfaces as well as bare nanoparticles. Thus, the thermal decomposition method was performed, yielding magnetite nanoparticles of higher crystallinity, and uniform size distribution decorating GO surfaces to a high coverage density with very little bare Fe_3O_4 observed. However, this method was not well suited for further work requiring colloidally stable nanoparticles as is expected for biomedical applications. The co-precipitation method was revised, using a lower loading of iron. The product appeared to have poor crystallinity, but the product was more pure chemically as indicated by a higher percentage of magnetite nanoparticles nucleating on GO surfaces. As a next step, hydrothermal synthesis methods should be investigated to produce crystalline magnetite and be colloidally stable.

Chapter 3: Hydrogels Incorporating GO-Based Nanoparticles for Mechanical Reinforcement

3.1 Introduction

This chapter encompasses the work done on crosslinking alginate and studying the effect of nanoparticle incorporation on the mechanical properties of the hydrogel. Briefly, the incorporation of GO and GO-Fe_3O_4 into alginate-based systems through physical interactions with the polymer was explored. In addition the covalent coupling of GO to alginate was performed, with a preliminary study on the resulting hydrogel mechanical properties. Finally, work was done to evaluate the viability of alginate as a scaffold material for tissue engineering.

The following section briefly reviews relevant background information on the use of alginate towards the fabrication of hydrogels, and relevant literature on the methods of nanoparticle incorporation into polymeric matrices for high-performance composites. The use of alginate for biomedical applications is widespread in biomedical applications.[92–94] Alginate is a linear unbranched polysaccharide that can be isolated from several sources such as seaweed or bacteria. The structure is composed of two monomer units: β-D-mannuronic acid (M block) and α-L-guluronic acid (G blocks), which form the polymer chain as repeating M units, repeating G units and as a random, or atactic, sequence of M and G blocks. This chemical composition, along with the overall M:G ratio, affects the physical properties such as mechanical strength, elasticity and swelling.[95] The reason is because alginate crosslinks through the use of multivalent cations, such as Ca^{2+}, Ba^{2+}, La^{3+}, Fe^{3+}, Zn^{2+}, Mg^{2+} and Sr^{2+}. These ions, with varying affinity,[92] electrostatically interact with two neighbouring alginate chains possessing a GG block presenting carboxylic and alcohol groups, forming an egg-box structure. It is due to the ease of this crosslinking process which makes alginate popular as a material for forming hydrogels. At the same time, it is recognized that this crosslinked network is a transient structure, as monovalent ions present in the physiological environment or in vitro culture conditions, such as Na^+ and K^+ or chelating agents such as phosphates, citrates and ethylenediaminetetraacetic acid (EDTA), will cause a reversible sol-gel transition and weaken the gel, until an equilibrium is reached. Therefore, there is a consensus among the scientific community that alginate gels are difficult to control in terms of its mechanical properties, swelling and degradation profile as multivalent ions are lost to the surrounding solution.

Researchers have devised strategies in order to create mechanically stronger hydrogels. Traditionally, methods such as increasing polymer concentration and crosslinking density have been employed. For example, Ahearne et al. found a linear increase in elastic modulus with increasing polymer concentration for alginate and agarose hydrogels.[96] Similarly, increasing the number of chemical crosslinks tends to increase the stiffness of gels, as found by Kong et al. while systematically studying ionic and covalent crosslinks in alginate hydrogels.[97] However, these strategies have their shortcomings. Increased polymer concentration leads to lower porosity, having direct implications in cell viability since the diffusion of molecules and cell migration through the porous structure is hindered.[44] Increasing the density of chemical crosslinks tends to create more rigid gels, but are more brittle since these gels can't dissipate energy as effectively. These gels have a lower ultimate strain and hence, a lower toughness. Nanoparticles have been incorporated into nanocomposites including hydrogels in order to impart their properties. Specifically in terms of mechanical strength, the use of CNTs has been shown to improve the compressive and tensile moduli without sacrificing porosity.[44] GO has been used to simultaneously improve the stiffness and toughness of gelatin hydrogels.[98] This chapter explores two different methods to create alginate hydrogels with improved mechanical properties using GO-based nanoparticles.

One method of creating mechanically reinforced hydrogels is by inducing preferential alignment of structural elements, and may inadvertently create heterogeneous structures at the nano and microscale. Creating heterogeneous structures can be achieved by techniques such as 3D printing/computer aided design[16,3] and using layer-by-layer techniques to build up tissue,[99,100,101] which typically focus on directing cell organization. Other work focus on creating aligned structural elements to study the effect on mechanical properties such as the alignment of electrospun fibers.[102,103] One method which was the inspiration for this work is the use of magnetic fields to direct structural elements, and has been shown to direct collagen fibers into lamellar structures[104] or the self-assembly into vessels.[105] The goal of the work summarized in this chapter was to use magnetically responsive GO to create anisotropic structures for enhanced mechanical properties and direct cell organization, owing to enhanced cell adhesion onto GO surfaces.[50,101]

The other method involves the covalent conjugation of reinforcing nanoparticles to the matrix material. Although nanoparticles such as CNTs and GO confer enhanced mechanical

properties, they also tend to aggregate, especially with high nanoparticle concentrations. Another factor that determines the efficacy of reinforcement is the polymer interaction with the polymer.[106] For example, by chemically conjugating GO to gelatin, Cha et al. demonstrated enhanced interaction and colloidal stability of the GO/gelatin suspension at increased concentrations compared to non-covalently modified nanoparticles and contributed to higher ultimate strain and toughness. The second part of this chapter explores the covalent conjugation of GO to alginate to improve the interaction between the nanoparticle and matrix.

3.2 Materials and methods

Fabrication and Characterization of GO-Fe_3O_4 hydrogels

GO-Fe_3O_4 (following the formulation from **Section 2.3.4**) was suspended in alginate (sodium salt, 120,000-190,000g/mol, Sigma). Immediately following the synthesis, 5mL of the nanoparticle solution (aqueous) was vacuum filtered (0.1µm pore size, polycarbonate, Whatman) to determine the concentration of the nanoparticle suspension. Simultaneously, 2w/v% alginate was prepared in milliQ water, and the nanoparticle solution and alginate solution were added 3:1 by volume to attain a GO-Fe_3O_4 suspension in 0.5w/v% alginate. Hydrogels with varying GO-Fe_3O_4 concentrations were crosslinked in custom-made cylindrical molds (7mm diameter x 3mm height) in 2w/v% $CaCl_2$ (Sigma) for 45min until fully crosslinked.

Unconfined compression testing was performed on a TA XT Plus Texture Analyser (Stable Micro Systems). Samples were examined for physical defects and air bubbles before being tested, and the dimensions of each sample were measured with calipers. The crosshead speed was set to 0.05mm/s. The compressive modulus was extracted from the slope of the first 10% of stress-strain curve, where the curve was linear.

Synthesis of GO-EDA-alginate

GO was modified with alginate using EDC/NHS coupling chemistry. 200mg of GO and 100mg of alginate were dissolved in 0.1M 2-(*N*-morpholino)ethanesulfonic acid (MES), as an aqueous solution. 49.44mg of 1-Ethyl-3-(3-dimethylaminopropyl)carbodiimide (EDC) (G Biosciences) and 29.76mg of *N*-Hydroxysuccinimide (NHS) (Alfa Aesar) were added to the reaction mixture and the carboxylic acids were allowed to activate for 1h. Subsequently,

2.224mL (equivalent to 2g) ethylenediamine (EDA) (Acros Organics, 99+% pure) was diluted with water and added to the reaction flask slowly. The reaction was allowed to proceed overnight (~18h), after which the reaction was washed four times with water (10,000g, 20min) and the product was left as a suspension for further experiments. For FTIR or TGA analysis, samples were dehydrated with at least two washes with reagent alcohol and lyophilized. The final product was designated as GO-EDA-alginate. The same reaction was carried out, without alginate, to study EDA-mediated reduction of GO; this product was designated as GO-EDA.

Characterization of GO-EDA-alginate

Fourier Transform Infrared (FTIR) spectroscopy was performed on a Bruker Tensor 37 FTIR spectrometer from 400 to 4000cm^{-1} averaging over 16 scans. Samples were ground in a mortar and pestle with IR spectroscopy grade KBr (Fisher Scientific) and compressed into pellets (Carver pellet press). Ethylenediamine was analyzed by sandwiching a droplet in between two salt plates, then mounted into a special holder for analysis. Zeta potential measurements were performed on a Malvern ZS90 equipped with a 633nm laser. The scattering angle was 90°, and the temperature was equilibrated to 25°C before scanning. Samples were prepared and diluted in water to avoid nanoparticle aggregation, and three scans were performed for each sample. UV-Vis spectroscopy was performed on a Agilent 8453 UV-visible spectrometer with quartz cells. Thermogravimetric analysis (TGA) experiments were performed on a TA Instruments SDT Q600 instrument. GO-EDA and GO-EDA-alginate were freeze dried. Samples were then crushed in an agate mortar and pestle to ensure sufficient contact with the purge gas. Samples were loaded (~10mg) into an alumina crucible, and run with nitrogen as the purge gas (100mL/min) with a temperature ramp of 5°C/min. The oven was set to ramp up to 100°C and hold at isothermal conditions for 30min, and the temperature ramp was subsequently resumed at 5°C/min to 800°C. The mechanical properties were evaluated with a TA XT Plus Texture Analyser (Stable Micro Systems), with a crosshead speed of 0.05mm/s.

Cell Studies

NIH-3T3 cells (ATCC) were cultured according to the supplier's instructions. Cells were cultured in a cell culture incubator (Revco Ultima II) in a 5% CO_2 atmosphere a 37°C. Cells were maintained in Dulbecco's modified Eagle's medium (DMEM, Lonza) supplemented with

10% Fetal Bovine Serum (FBS) and 1% penicillin/streptomycin (ATCC), and changed every 3 days. Cells were passaged at approximately 70% confluency.

For cell encapsulation studies, alginate was prepared at 0.5w/v% and sterilized by filtering through a 0.22µm polyethersulfone (PES) filter inside a biosafety cabinet. Cells were passaged with trypsin-EDTA (0.025%, Lonza) and resuspended to a concentration of 5 x 10^5cells/mL. The viability was measured using the trypan blue exclusion assay and counted using a haemocytometer, and used to adjust the working cell concentration. Alginate slabs were crosslinked using a custom mold (1cm x 1cm x 1mm) in a 2w/v% $CaCl_2$ salt bath for 5min. Cells were seeded on top of the slabs at a density of 10^5cells/well, in a 6-well plate. For cell encapsulated hydrogels, the 0.5w/v% alginate was mixed with the cell suspension in a 3:2 ratio and crosslinked under the same conditions. Cells were examined for morphology using an inverted light microscope (Zeiss Invertoskop 40C). The calcein-AM/ethidium homodimer Live/Dead assay (Invitrogen) was used to label the cells, according to the manufacturer's instructions. Calcein-AM and EthD-1 were diluted to 1µM and 2µM, respectively, in Hank's balanced salt solution (HBSS). Cells were labelled at designated time points, incubated for 30min at 37°C following the addition of dye, then replaced with fresh HBSS. Cells were visualized under confocal laser scanning microscope (CLSM) (LSM 510, Zeiss).

3.3 Results and discussion

3.3.1 Alginate Hydrogels incorporating GO-Fe_3O_4

GO-Fe_3O_4 nanoparticles have a propensity to aggregate, due to magnetic dipole-dipole interactions and van der Waals attractive forces,[57] as such nanoparticles requiring colloidal stability were suspended in alginate immediately after the synthesis and purification of GO-Fe_3O_4. Alginate was chosen due to its widespread use as a polymer for biomedical applications, as well as the possibility of a strong interaction with the iron oxide nanoparticle surface from electrostatic attractions between the iron cations and the carboxylic acid groups on alginate polymer chains.[55]

The first step was to determine a concentration of alginate to use for GO-Fe_3O_4 incorporated hydrogels. Alginate supplied from Sigma Aldrich, with a molecular weight ranging from 120,000 to 190,000g/mol, were crosslinked at 0.5, 1 and 2w/v%. **Figure 3.1a** shows

representative stress-strain curves obtained from varying the alginate concentration in the pre-gel solution. The compressive moduli were calculated based on the first 10% of the curves, in the linear portion. The compressive moduli are: 11.58 ± 1.53kPa, 36.74 ± 2.17kPa, and 129.38 ± 12.62kPa for 0.5w/v%, 1w/v% and 2w/v%, respectively (**figure 3.1b**). It was concluded that 0.5w/v% alginate would be used, since it was observed in other works that GO improved the compressive modulus by 2 to 3 times when the hydrogel, with no nanoparticle loading, was in the range of 5 to 10kPa.[50,98] Upon nanoparticle incorporation, even a low loading of GO (~2.0mg/mL) resulted in pronounced enhancement of several times. It was important to be able to demonstrate a significant improvement in compressive modulus at low nanoparticle concentrations, since nanoparticles tend to aggregate at higher concentrations to lower surface energy. In addition, the synthesized GO-Fe_3O_4 tends to be viscous at its working concentration and difficult to work with.

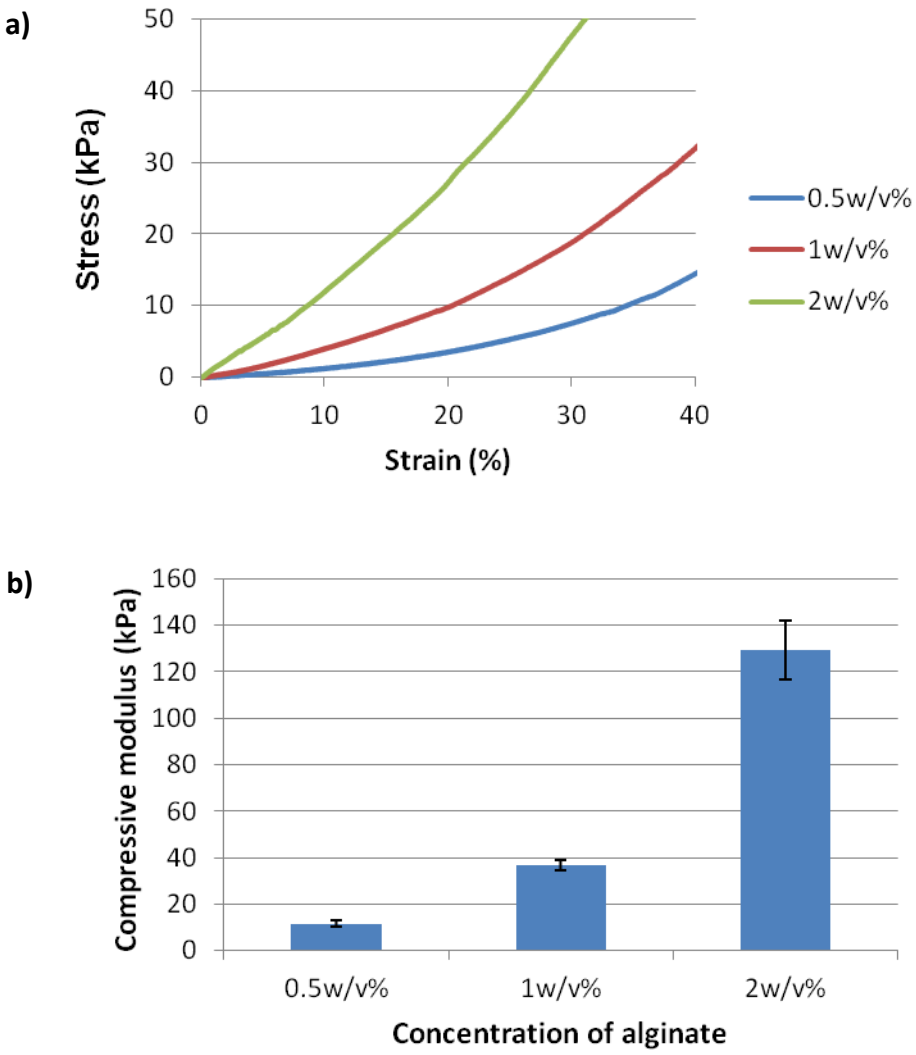

Figure 3.1: Mechanical properties of alginate. a) Representative stress-strain curves for varying concentration of alginate. b) Compressive moduli of hydrogels of varying alginate concentration, error bars represent the standard deviation (n=10).

Next, GO-Fe_3O_4 alginate hydrogels were fabricated following the procedure outlined in **Section 3.2**. As a point of comparison, alginate hydrogels incorporating GO were also fabricated. The mechanical properties can be closely compared by representing the incorporated nanoparticle concentration as the effective GO concentration. For GO-Fe_3O_4 samples, this can be calculated using the mass ratio derived in **Section 2.3.4**. Unconfined compression tests were carried out on a series of samples, shown in **figure 3.2** (a set of samples with 1.0mg/mL nanoparticle concentration were tested, but omitted due to an error in preparing the pre-gel solution). It can be concluded that both GO and GO-Fe_3O_4 exhibit increasing compressive moduli with nanoparticle concentration, leading to stiffer gels. In fact, the relationship between

compressive modulus and nanoparticle concentration follows a linear trend for hydrogels incorporating GO and GO-Fe_3O_4 (**figure A.1**). It can also be concluded that the mechanical reinforcement between GO and GO-Fe_3O_4 for tested nanoparticle concentrations are quite similar. This suggests that GO, possessing a rigid sheet structure, is solely responsible for mechanical reinforcement regardless of the mass of Fe_3O_4 that decorates the GO surface. The data in **figure 3.2b** shows that the ultimate strain reaches a maximum at a certain nanoparticle concentration, after which any higher loading of nanoparticles will cause earlier failure, in other words a lower ultimate strain. Thus, it shows that excessive nanoparticle loading leads to poor toughness, which is due to nanoparticle aggregation at high nanoparticle incorporation. It has been suggested that GO, which is a rigid structure, limits the compressive deformation of the elastic components of the matrix, leading to earlier fracture.[50] In that sense, it appears that GO-Fe_3O_4 is more rigid and causes brittle fracture at lower ultimate stresses.

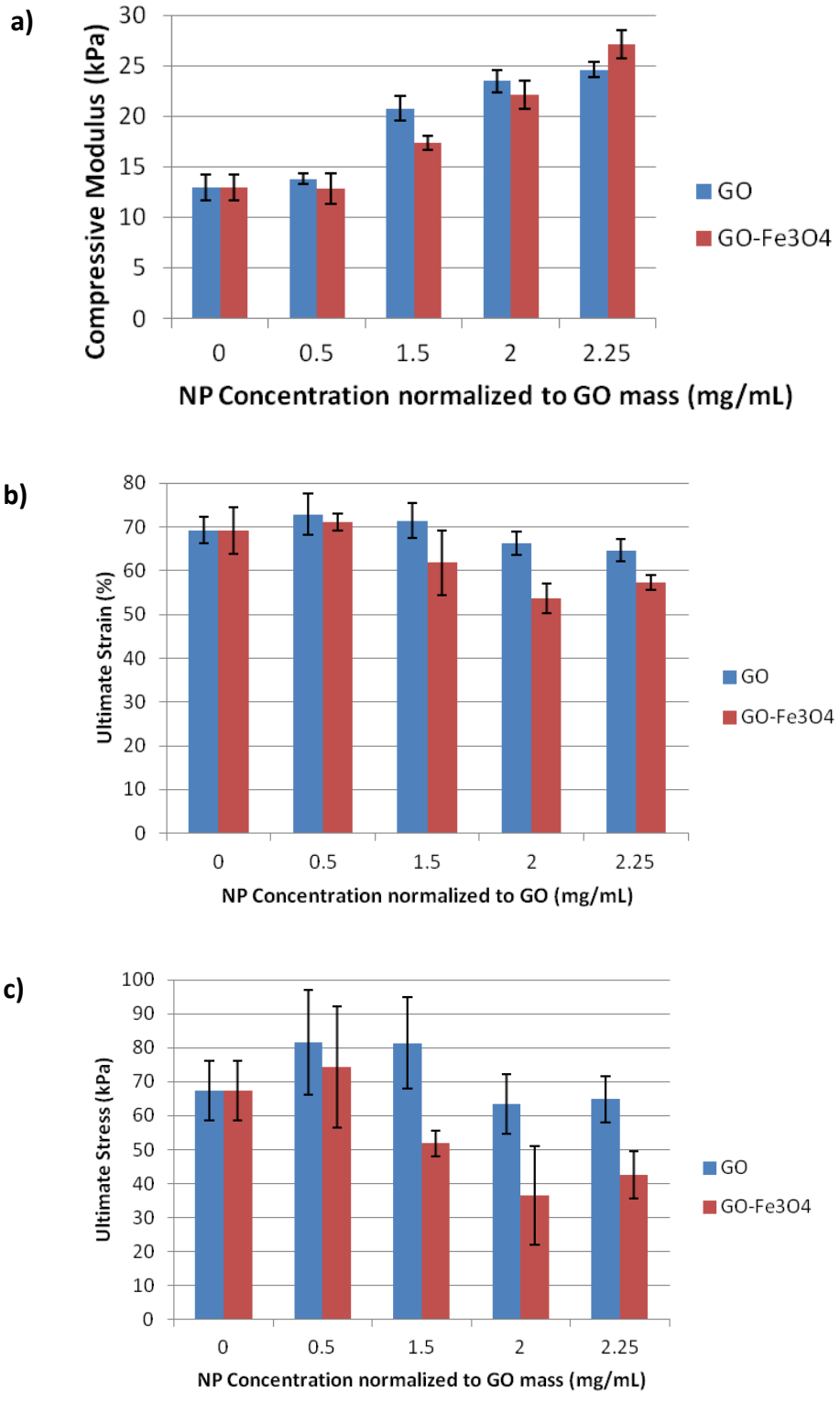

Figure 3.2: Mechanical properties of the GO and GO-Fe_3O_4 hydrogels (0.5w/v% alginate) with varying concentrations of nanoparticles normalized to the GO mass concentration. a) Compressive moduli of GO and GO-Fe_3O_4 hydrogels. b) Ultimate strain of GO and GO-Fe_3O_4

hydrogels. c) Ultimate stress of GO and GO-Fe_3O_4 hydrogels. Error bars represent the standard deviation of measurements performed on five samples.

To demonstrate the use of magnetically responsive nanoparticles to create heterogeneous, anisotropic structures, alginate hydrogels with incorporated GO-Fe_3O_4 were crosslinked in the presence of fridge magnets. These magnets were measured to have a uniform field strength of ~30mT at the particular distances used in this setup (**figure 3.3a and b**) In such an experiment, molds were filled with the pre-gel solutions and allowed to stand for 10min with the magnets set up as described in **figure 3.3a and b** before crosslinking with $CaCl_2$. As shown in **figure 3.3c**, the externally applied magnetic field did not produce any effect on the mechanical properties due to the anisotropically aligned GO-Fe_3O_4. A different experiment was tried (**figure A.2**) where Fe_3O_4 and GO-Fe_3O_4, suspended in alginate solution, was diluted and left to dry overnight with the fridge magnets in place. The results show that the Fe_3O_4, with higher saturation magnetization, respond to the external stimulus by forming needle shapes, whereas no reorganization is exhibited by the GO-Fe_3O_4. This proves that the GO-Fe_3O_4 as synthesized by the revised co-precipitation method does not possess a high enough magnetic response to the current field strength of 30mT. Work in this field have studied nanoparticle orientation in a magnetic field by statistical mechanics analysis,[107,108] which may be helpful in elucidating the shortcomings of the current nanoparticles.

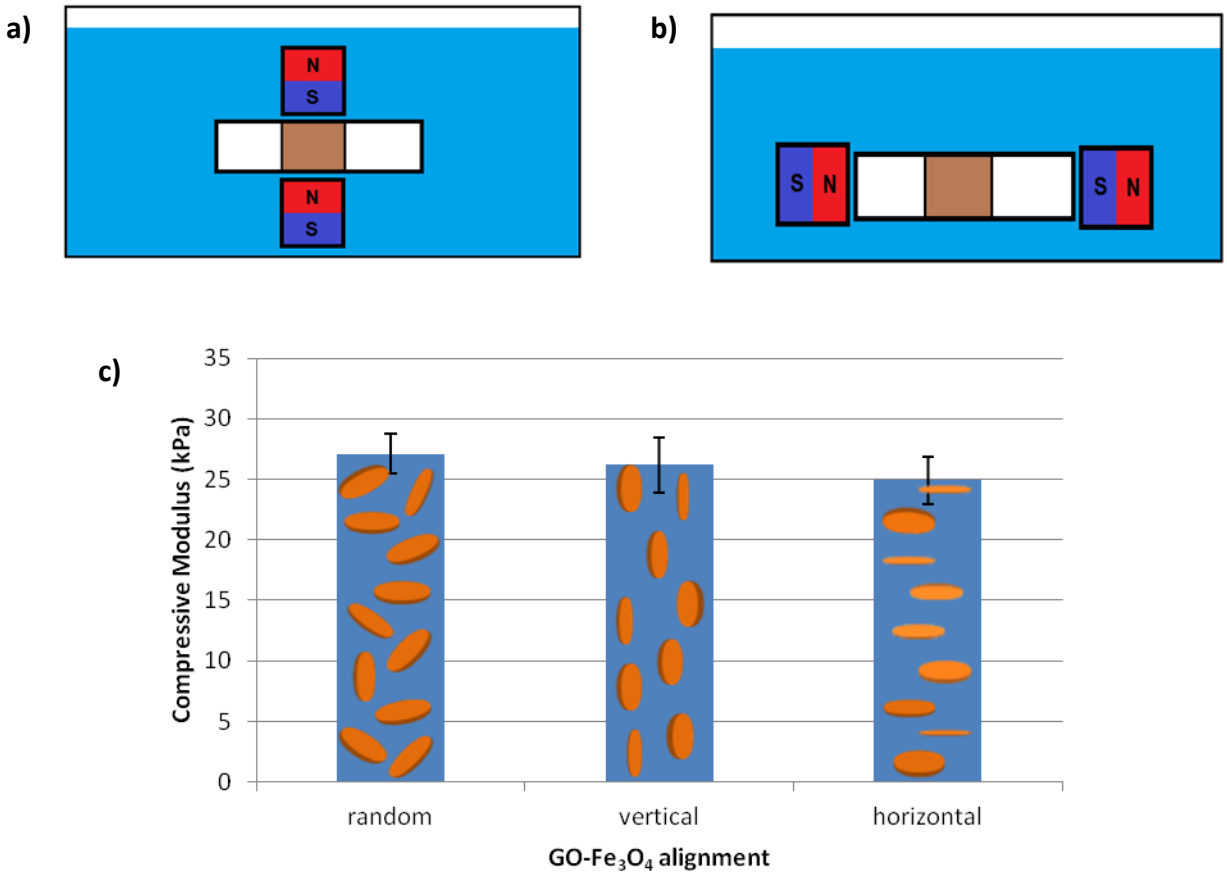

Figure 3.3: The effect of anisotropically ordered GO-Fe_3O_4 on mechanical properties. A schematic of the experimental setup showing a vertically applied magnetic field (a), and a horizontally applied field (b). c) Compressive modulus of 0.5w/v% alginate hydrogels after GO-Fe_3O_4 (2.25mg/mL) has been aligned by a magnetic field and fixed in place by gelation.

3.3.2 Alginate Hydrogels incorporating GO-EDA-alginate

The second part of this chapter explores the covalent conjugation of GO nanoparticles to polymer chains in order to create hydrogels with enhanced mechanical strength. GO was modified by EDC/NHS conjugation to covalently link alginate and GO through their carboxylic acid groups. Ethylenediamine was selected as a crosslinking molecule since it presents two primary amine groups. FTIR was used to examine the success of the reaction (**figure 3.4a**). Amines such as ethylenediamine can reduce GO, and FTIR can be used to monitor the degree of reduction.[109,110] GO-EDA and GO-EDA-alginate showed reduced peak intensities at 1730cm^{-1}, 1400cm^{-1} and 1224cm^{-1} corresponding to COOH, OH and epoxy groups. In addition, a new peak appeared at 1175cm^{-1} and was attributed to EDA. The peak at 1628cm-1, corresponding to C=C

stretching, broadened since EDA has an intense peak at 1600cm^{-1} (see **figure B.2**). Thus it can be concluded that this reaction was successful in conjugating EDA to GO and produced reduced GO concurrently, but it is difficult to identify alginate in the final product since its characteristic peaks are weak which can be obscured by the broad absorption by reduced GO, and the more intense peaks overlap with GO. Supplementary techniques were performed.

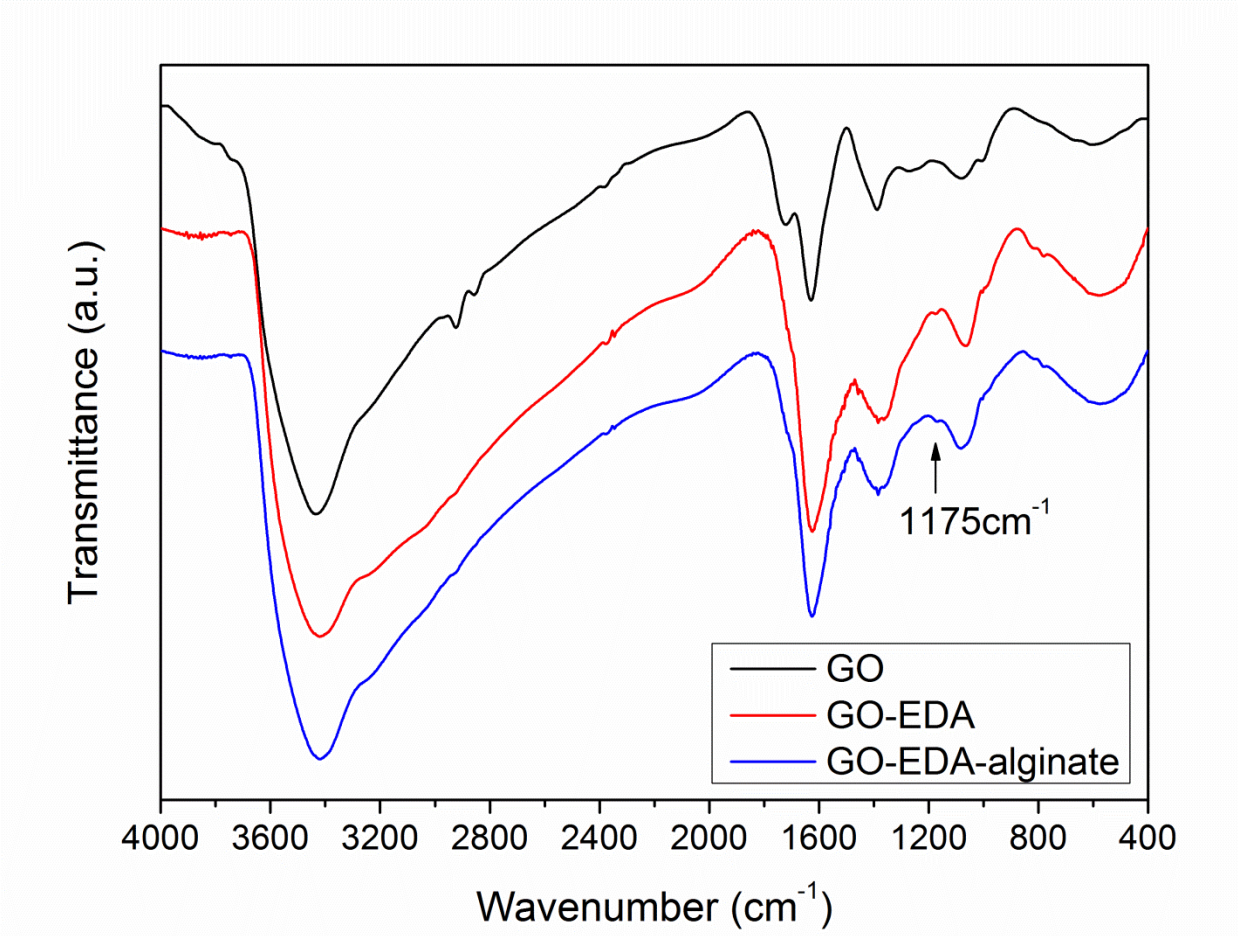

Figure 3.4: FTIR spectra for GO, GO-EDA, and GO-EDA-alginate.

UV-Vis characterization revealed some additional information (**figure 3.5**). As GO was reduced, the peak at 228nm did not change in position, indicating that although some oxygen-containing groups were being removed, the overall conjugated structure of the carbon basal plane was not being restored.[80] In addition, the shoulder at 300nm remained visible. This peak corresponds to the n-π* transition of C=O, meaning that the degree of carboxylic acid groups being removed was not very high. Absorption in the region greater than 228nm (visible light)

increased, corresponding to the darkening solution as the reaction proceeded. Overall, we can conclude that EDA mildly reduced the GO over the course of the reaction.

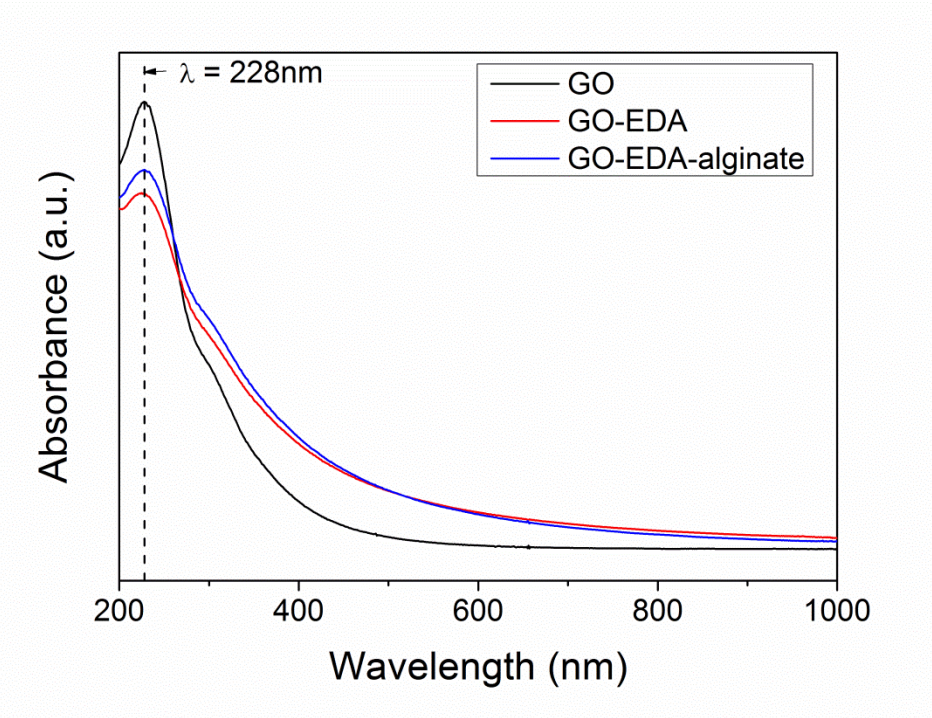

Figure 3.5: UV-visible spectra for GO, GO-EDA, and GO-EDA-alginate.

To confirm the covalent attachment of alginate to GO, zeta potential was used as another supporting characterization method (**figure 3.6**). Zeta potential works in conjunction with DLS, where nanoparticle surface charge can be quantified by measuring their velocity from electrophoretic motion. GO is usually very negatively charged due to its abundance of carboxylic acid groups. Upon conjugation of EDA to the carboxylic acids, the net surface charge tended toward neutral as EDA presents an amine group after coupling to GO. When alginate is conjugated to the amine group presented from EDA, the surface charge became more negative, since alginate chains possess a high number of carboxylic acids. Hence, the characterization methods presented here can prove that alginate was successfully conjugated to GO.

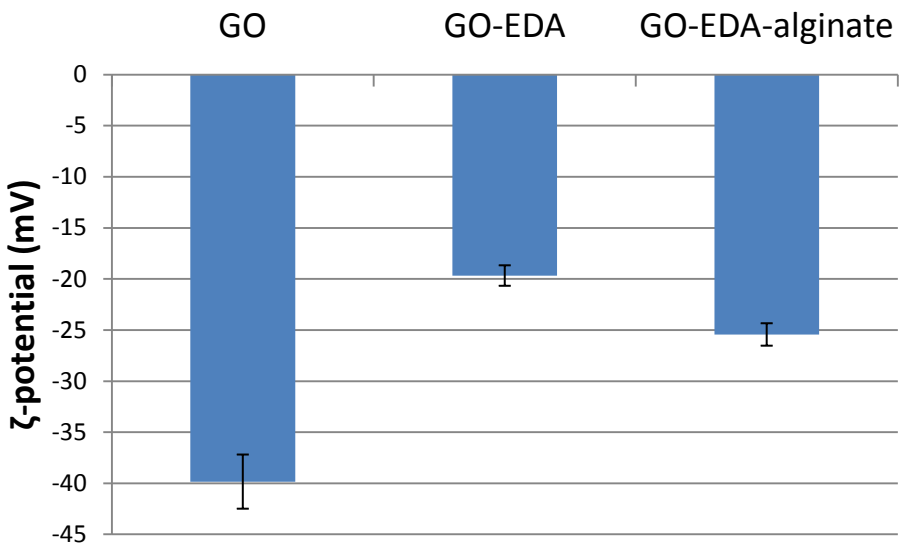

Figure 3.6: Zeta-potentials for GO, GO-EDA, and GO-EDA-alginate nanoparticles.

Thermogravimetric analysis was performed to quantify the mass of alginate conjugated to GO. **Figure 3.7** shows alginate, GO-EDA, and GO-EDA-alginate heated under nitrogen flow. Samples were run with a temperature ramp at 5°C/min until the instrument reached 100°C, when it was programmed to maintain isothermal conditions for 30min to let moisture desorb. The temperature ramp was continued until 800°C. The alginate sample shows complete degradation by the time the oven reaches and stabilizes at 800°C. For GO-EDA and GO-EA-alginate samples, after moisture desorption, there was a mass loss at 150-200°C resulting from the removal of oxygen-containing groups. Finally, covalently bound compounds were removed from GO in the range of 200-500°C, which included conjugated alginate.[111] The final remaining mass% (at 800°C, and factoring out the mass lost from adsorbed moisture) for GO-EDA was 54.5%, and 51.2% for GO-EDA-alginate, and the GO-EDA (or reduced GO) mass contribution can be calculated as being 94.9% of the mass, with 5.1% of the remaining mass composed of alginate. This seems like a small quantity; potentiometric titration could be done to quantify the number of carboxylic groups in a given volume or mass of GO and could be very useful in designing new synthesis protocols. In such a way, moles : moles calculations can be done instead of the current method of using mass : moles (GO : ligand), and would give more information about the reaction efficiency with the alginate.

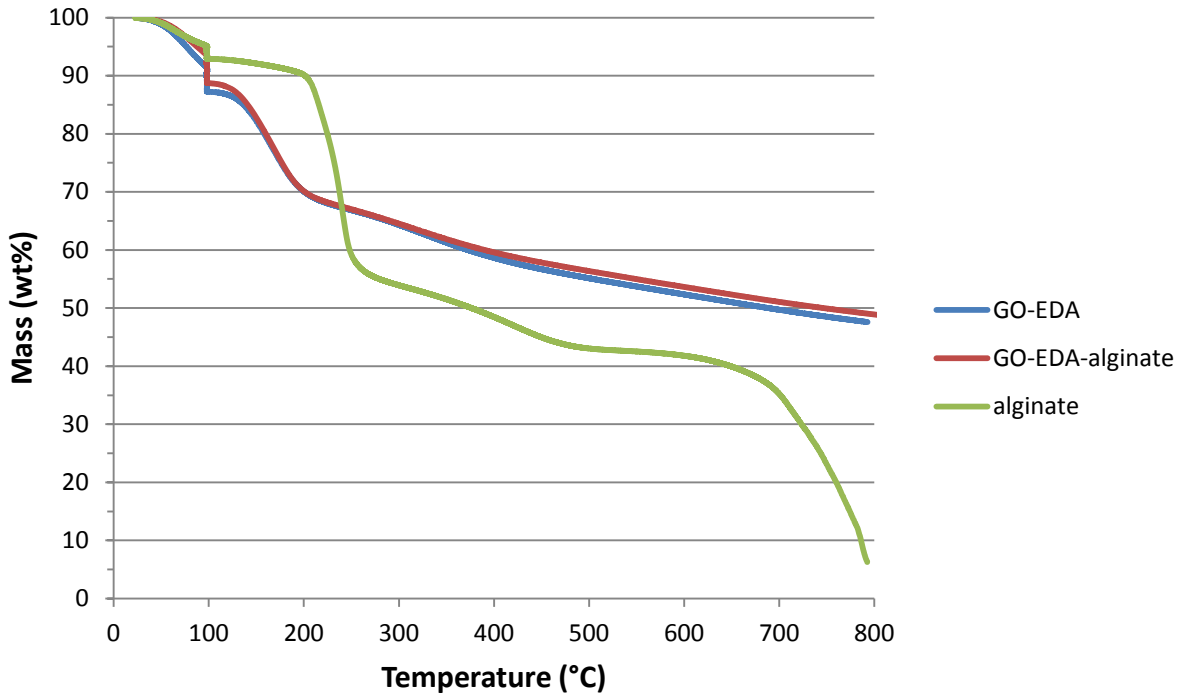

Figure 3.7: TGA curve for GO, GO-EDA and GO-EDA-alginate, with nitrogen as the purge gas.

GO-EDA-alginate was used to fabricate hydrogels, and compared with GO hydrogels. In terms of the compressive modulus, GO follows a linear trend with increasing nanoparticle concentration which is the same trend as before (**figure 3.8a**). It is interesting to see that GO-EDA-alginate hydrogels do not get stiffer with increasing nanoparticle concentration. Looking at the ultimate strain, we see that GO hydrogels have slightly lower values than the control (**figure 3.8b**). This may be due to the fact that GO is a rigid structure that can't dissipate the energy from compression. When compared with GO-EDA-alginate, it is evident that the ultimate stress (and strain) achieved is much higher, indicating that the energy dissipation is much better in this case. It can be seen that GO helps dissipate energy to achieve a high toughness only when the covalent bonds are formed, which helps the interfacial interaction between GO and alginate. This can be rationalized by the fact that alginate is very hydrophilic and would not have many sites to interact with GO favourably, which is a hydrophobic plane of sp^2-hybridized carbon with functional groups that confer some hydrophilicity. At higher GO-EDA-alginate concentrations, it can be seen that the positive effects of using covalent linkages can't overcome the propensity for nanoparticle aggregation, resulting in lower fracture energies.

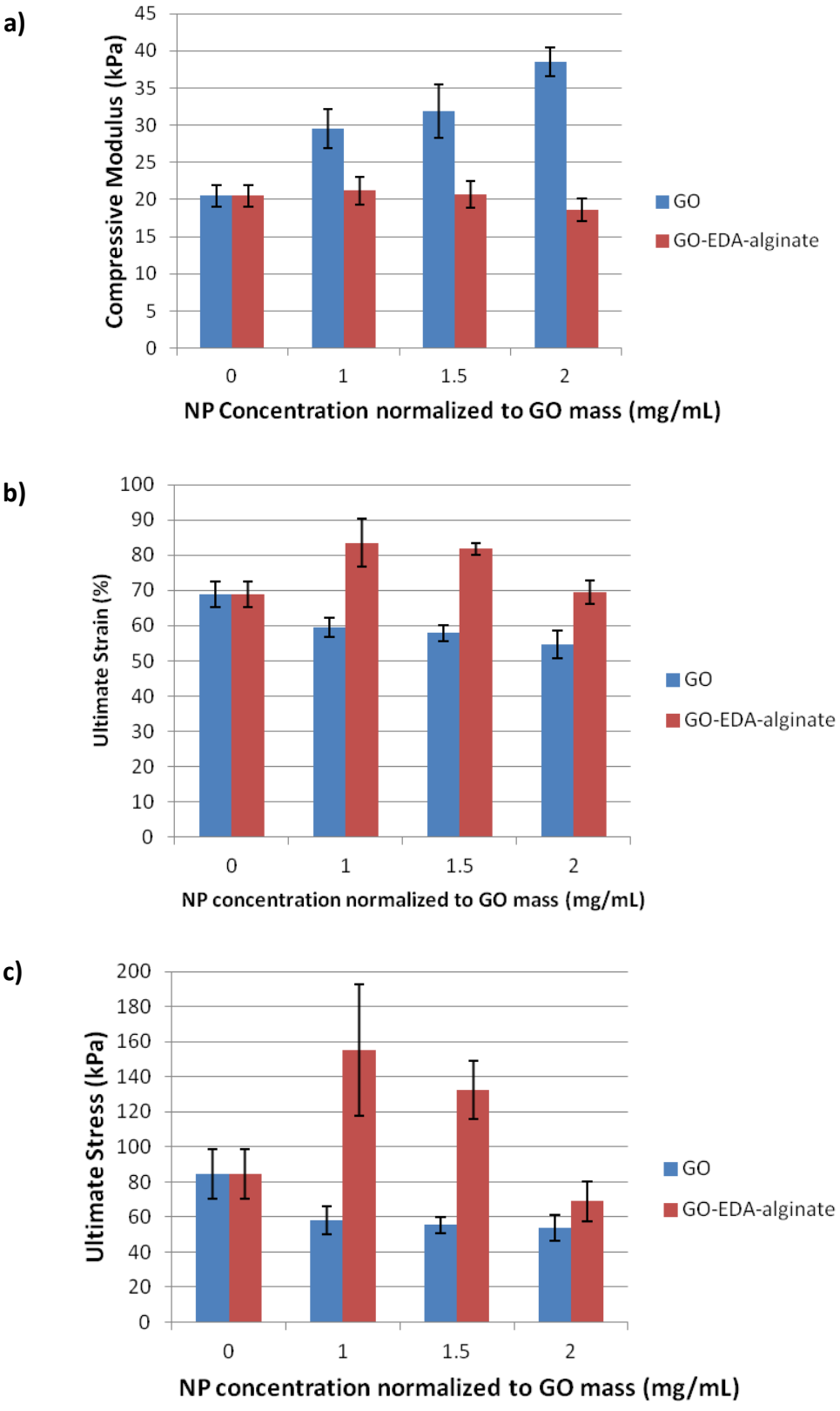

Figure 3.8: Mechanical properties of the GO and GO-EDA-alginate hydrogels (0.5w/v%

alginate) with varying concentrations of nanoparticles normalized to the GO mass concentration. a) Compressive moduli of GO and GO-EDA-alginate hydrogels. b) Ultimate strain of GO and GO-EDA-alginate hydrogels. c) Ultimate stress of GO and GO-EDA-alginate hydrogels. Error bars represent the standard deviation of measurements performed on six samples.

Overall, it can be concluded that the use of covalent bonds to help nanoparticles form a more favourable interaction with the polymer matrix mainly improves the toughness. This observation was also seen by Cha et al., who used covalently crosslinked GO to gelatin.[98] Although the effects seen in the current work is not as impressive as Cha's work, perhaps with the appropriate selection of a polymer system, a similar enhancement can be achieved.

3.3 3 Cell Viability Studies

The viability of NIH-3T3 fibroblasts was examined using alginate hydrogels. Viability was studied in two ways: by observing the cell morphology under light microscope and by using the Live/Dead assay supplied by Invitrogen. The cell morphology can indicate how well cells adhere to substrates, appearing to be spread out to maximize contact with the substrate if interaction is favourable. Moreover, observation of cell morphology may reveal any underlying sources of toxicity to the cell, since they will form a globular shape and lift from the substrate.

Three groups of samples were studied. In the first case, cells were seeded onto glass cover slips placed in a cell culture plate, as a control. The second group of samples was made by seeding a cell suspension onto fabricated alginate films. The third group was made by mixing the cell suspension with the 0.5w/v% alginate polymer solution in a 2:3 ratio and crosslinking it to form a cell-encapsulated alginate film. **Figure 3.9** shows images taken on a light microscope for the three groups of samples, taken approximately 24 and 48h after gel formation or cell seeding (named Day 1 and Day 2, respectively). On Day 1, the control sample appeared to have a relatively high proliferation rate compared to the other groups, and had a stretched morphology characteristic of adherent cell lines such as fibroblasts. The control group continued to have the highest proliferation on Day 2, exhibiting signs of assembly into organized bundles. Fibroblasts seeded on to alginate films had a much lower proliferation rate based on the confluency of the substrate. It could also be seen that the cells had a rounded shape and were in the process of lifting off the film, indicating a cytotoxic event. Day 2 results indicated that cells continued to lift, although the surviving cells had a slightly stretched morphology which shows that they were beginning to recover their biological function. For fibroblasts encapsulated in alginate films, they

appeared globular since there is no surface for the cells to adhere to and not much can be concluded about the viability for Day 1 and 2.

The other technique used to study cell viability was the Live/Dead assay. The study was only performed for Day 1 samples (see **figures C.1-3**). Upon transferring gel films to the microscope stage, the alginate had mostly reverted back into a solution, indicating that the monovalent salts in DMEM can fairly quickly replace the Ca^{2+} salts involved in the crosslinking reaction. Also, all sample groups showed co-localization of calcein-AM and EthD-1, indicating that cells still exhibited biological function through the conversion of the calcein-AM into fluorescent calcein. However the internalization of the EthD-1 indicated cell lysis. These results are not conclusive since we cannot definitely say that the cell encapsulation and seeding process was cytotoxic, due to the fact that the EthD-1 was also internalizing into cells in the control sample.

To shed light onto the underlying phenomena, it should also be noted that the HBSS used to prepare the fluorescent dye solution is not the correct buffer to use given the particular protocol that was performed. HBSS has a relatively low concentration of sodium bicarbonate, which normally buffers against alkalinity caused by dissolved CO_2. Under ambient atmospheric conditions (low CO_2 conditions), HBSS can sufficiently buffer against CO_2 present, but is not suitable for incubation in a 5% CO_2 environment. This may have led to the low viability of the fibroblasts. The current assay protocol needs to be modified such that the incubation with the calcein-AM/EthD-1 is carried out at room temperature or a different buffer should be used to prepare the dye working solution, such as phosphate buffered saline.

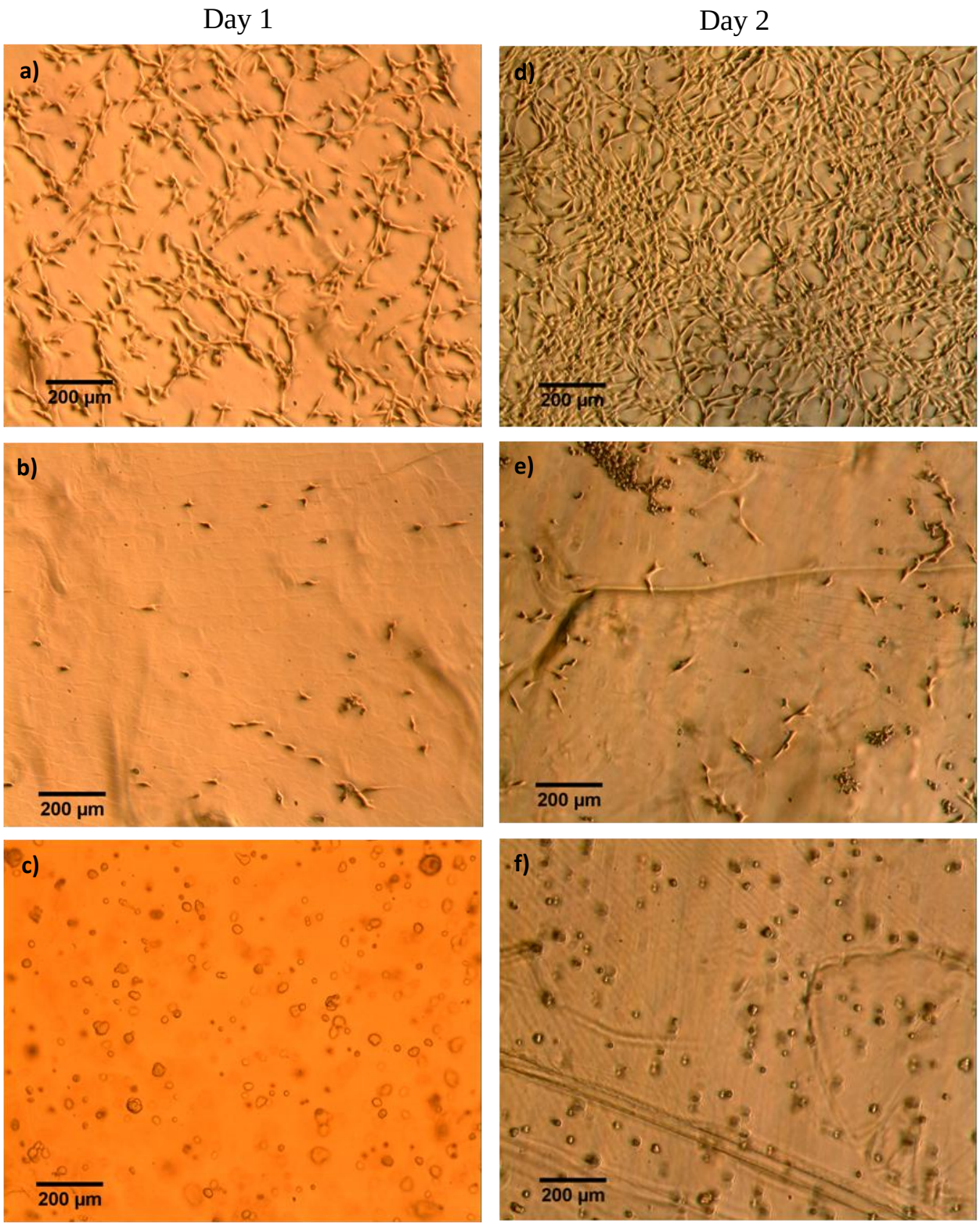

Figure 3.9: Morphology of cultured 3T3 fibroblasts. a-c) Day 1 images of 3T3 cells seeded on a glass cover slip (control), 3T3 cells seeded on alginate film, 3T3 cells encapsulated in alginate film. d-f) Day 2 images of 3T3 cells seeded on a glass cover slip (control), 3T3 cells seeded on alginate film, 3T3 cells encapsulated in alginate film.

There are conflicting reports detailing the biocompatibility of the encapsulation, where researchers present varying observations regarding cell viability from the encapsulation process.[93,112,113] A more detailed review needs to be performed to understand the experimental parameters used, such as the calcium salt concentration and gelation time used. In one study, it was reported that cell viability for swine-derived MSCs was only 53% after a 10min exposure to 102mM $CaCl_2$, but viability recovered to 94% after 15 days for cells encapsulated in alginate.[113] As a comparison, 2w/v% $CaCl_2$ used in this current work is equivalent to approximately 180mM. It can be concluded that encapsulated cells can recover their biological function if given enough time, and cultured in the recommended conditions. This can be supported by the fact that fibroblasts seeded on alginate films began to recover and showed a healthy morphology on Day 2 (**figure 3.9e**). It is recommended that after the gelation period, the $CaCl_2$ solution should be replaced with fresh media and regularly replaced until the encapsulated cells are viable before performing assays. The $CaCl_2$ concentration of 2w/v% or 180mM is quite high and can lead to cell lysis (see **figure C.4**, images were captured in a separate experiment) if incubated for extended periods due to hypertonic conditions. It is recommended that a lower salt concentration be used for the crosslinking, such as 20-100mM,[92] which may weaken the gel due to fewer ionic crosslinks being formed. Thus it is also recommended that a secondary mode of crosslinking be employed to improve the mechanical strength of the gels.

Finally, another explanation for the poor viability of encapsulated and seeded cells is that alginate does not promote cell adhesion.[114,115] Alginate does not have recognition sequences, unlike proteins such as collagen, which possess specific peptide sequences to promote cell binding. In addition, alginate is very hydrophilic, which is not conducive to the adsorption of serum proteins which may possess cell adhesion sequences. One strategy to improve the biochemical properties of alginate is through modification with peptides, such as the work by Rowley et al. where alginate was covalently modified with a RGD-containing peptide to enhance myoblast adhesion.[115]

To summarize this section, it appears that the alginate purchased from the supplier may be suitable for use as a scaffold material, but several concerns need to be addressed before investigating the biocompatibility of alginate hydrogels incorporating the nanoparticles synthesized in **Chapter 2**. The encapsulation process needs to be revised to use a lower $CaCl_2$ salt concentration in order to improve cell viability. The cultured cells require time to recover

their biological functions so a longer observation time is needed. Finally, modification of the alginate could be required, in order to maintain its structural integrity during culturing, or to promote cell adhesion through the incorporation of cell-binding ligands. These recommendations apply to both forms of scaffolding explored, whether cells are seeded on to films or are incorporated into the film.

3.4 Conclusions

The work in this chapter focused on creating nanostructures within hydrogels which could be directed by an externally applied magnetic field, which could be applied to creating anisotropically reinforced nanocomposites or for heterogeneous structures in directing cell organization. The nanocomposite hydrogel consisting of alginate incorporating GO-Fe_3O_4 showed that the mechanical reinforcement was comparable to GO in terms of enhancement in compressive modulus, however GO-Fe_3O_4 causes brittle fracture at lower ultimate stresses due to its rigid structure. Moreover, anisotropic reinforcement could not be demonstrated. It was believed that the GO-Fe_3O_4 did not possess a sufficient magnetic response to the magnetic field currently available.

The covalent linkage of GO to alginate was attempted. Current data shows that the conjugation reaction was successful, and the improved interaction between the nanoparticles and polymer phase results in enhanced toughness as opposed to matrix stiffness.

Cell encapsulation experiments revealed that the use of calcium salt as a crosslinker poses cytotoxic risk to 3T3 fibroblasts; moreover, the use of unmodified alginate is not amenable to cell adhesion. With extended periods, cell viability should recover, as was observed through cell morphology.

Chapter 4: Summary and Future work

Tissue engineering involves combining natural and synthetic materials that can integrate with the host body to facilitate healing or as tissue replacements. With increased academic interest in nanotechnology, this project aims to improve traditional polymeric materials with the properties of graphene oxide nanoparticles.

In **Chapter 2**, the decoration of graphene oxide flakes with iron oxide nanoparticles was explored, with the intent of creating heterogeneous structures in hydrogels. Coprecipitation methods were facile and tended to yield nanoparticles with excellent colloidal stability. Thermal decomposition was also investigated, demonstrating that high temperature processes served to improve the crystallinity of magnetite and hence, the magnetic properties. However, extended reactions at high temperature yields aggregated nanoparticles, which are not ideal for applications requiring a colloidally stable suspension of nanoparticles. The co-precipitation method was revised such that fewer magnetite particles nucleated on GO surfaces, yielding a cleaner product but was not as crystalline as the Fe_3O_4 synthesized by thermal decomposition.

In **Chapter 3**, GO-based nanoparticles were incorporated into alginate hydrogels to examine their mechanical properties. GO-Fe_3O_4 synthesized by the revised co-precipitation method were used in the fabrication of hydrogels. It was concluded that due to the rigid structure of GO-Fe_3O_4, the nanoparticle was able to increase the compressive modulus, but also resulted in lower ultimate strains, which has been observed in past works using GO. The magnetite synthesized by the revised co-precipitation method is not very crystalline, leading to a poor magnetic response.

GO was conjugated to alginate using EDC/NHS coupling. In such a system, it was shown that the compressive modulus did not differ much from hydrogels with no nanoparticle loading. On the other hand, the ultimate strain and by extension, toughness, was increased, due to the enhanced interaction between the reinforcing nanoparticle and the polymer matrix. It is suggested that the nanoparticles help to relieve compressive energy through deformations.

Finally, cell viability was investigated using alginate hydrogels. It was shown that the crosslinking method employed is cytotoxic. With time, cells begin to recover, which was observed in this work. Also, alginate hydrogels quickly lose their structural integrity when

subjected to cell media, so other polymers or a second mode of crosslinking is recommended to keep the structure in place for longer periods of time.

In light of the conclusions drawn from the current work, some recommendations for future work can be made. First, the nanomaterial needs to be redesigned from the ground up, and the problem can be broken down into several aspects. The first aspect deals with the synthesis of the GO-Fe_3O_4 hybrid material. Selective nucleation of magnetite on GO sheets has been observed as a challenge for the co-precipitation method, which yields a quick burst of nucleation followed by crystal growth, whereas minimizing the quantity of iron salts used yields low magnetic response, as was seen in this current work. Alternative methods include hydrothermal synthesis to yield crystalline magnetite in a slow controlled growth process or a two-stage synthesis where seed crystals are precipitated followed by crystal growth initiated by a second addition of iron salt. Such methods allow for controllable and predictable growth of nanoparticles, which relate directly to their magnetic properties. Thus it is crucial to understand and control the relevant parameters in the synthesis method.

The second aspect of the nanomaterial design is the surfactant used for stabilizing the GO-Fe_3O_4 nanoparticles. Alginate has been shown to stabilize the nanoparticles for weeks but may not be ideal for cell encapsulation purposes due to their lack of adhesion-promoting sequences, transient physical properties during culture conditions and the inherently cytotoxic encapsulation process. It may be possible to use a small ligand molecule to cap the nanoparticles during the synthesis which can then be subsequently covalently modified with polymers, or a combination of polymers that are known to enhance the biological function of encapsulated cells. A library of knowledge regarding the physical and chemical properties of polymers and other ECM substitute materials will allow for rational and methodical design of tissue scaffolds. On a related note is the establishment of a library of knowledge relating to conjugation techniques which also pose low cytotoxic risk, which is useful when making hybrid biomaterials intended for tissue engineering applications. Of direct relevance when chemical modifications are involved is the quantification of the functional groups on GO through techniques such as potentiometric titrations as previously mentioned. It is recommended as one of the characterization methods that should be performed on new batches of GO. Knowing the molar concentration of the functional groups on GO is essential if further work is to be done on

covalent coupling of GO to various polymers. This helps in being able to calculate a quantitative reaction efficiency and to potentially reduce the consumption of GO.

The fundamental physics that dictate ordering of the nanoparticles based on the applied magnetic field, thermal fluctuations, gravitational energy and viscosity of the pre-gel solution need to be better understood once the nanoparticles are made highly responsive to magnetic stimuli and demonstrating selective loading onto GO surfaces. With a strong knowledge base and methodical characterization of GO particle size, accurate hypotheses can be made regarding the strength of magnetic field required to induce nanoparticle ordering. The relationship between nanoparticle size and magnetic field strength is important, since it is always preferable to minimize the magnetic field strength required from a practical and academic standpoint.

In the application of GO-Fe_3O_4, work has already been done on using graphene oxide to anisotropically enhance electrical or mechanical properties, among many applications.[108,116] The real potential, once the synthesis of iron oxide nanoparticles is optimized, is the use in directing structural elements for heterogeneous scaffolding. One of the advantages of using magnetic fields to direct structural ordering is that the stimulus is applied remotely, with no impact on cultured cells. This can also apply to mechanical stimulation of cultured cells, where magnetically responsive hydrogels can periodically deform to provide a stimulus to cells without risking harm to them. In addition, work is currently being done on investigating the electrical conductivity of scaffolds, which can potentially exhibit anisotropic enhancement once the nanoparticle formulation is modified.

The work done on the GO-EDA-alginate system can be further expanded, such as in the study of the mechanisms of stress dissipation or in cyclic loading tests to study elastic recovery. Further literature search should be performed to gain a comprehensive understanding of polymer and nanomaterial behaviour and phenomena in various forms of mechanical testing if there is continued interest in studying the mechanical properties of soft nanocomposites. In the context of the work shown here, the factors that affect and enhance matrix stiffness and toughness need to be understood such that the expected outcomes can be predicted a priori.

References

1. Venugopal, J. *et al.* Biomimetic hydroxyapatite-containing composite nanofibrous substrates for bone tissue engineering. *Philos. Trans. A. Math. Phys. Eng. Sci.* **368,** 2065–2081 (2010).
2. Place, E. S., George, J. H., Williams, C. K. & Stevens, M. M. Synthetic polymer scaffolds for tissue engineering. *Chem. Soc. Rev.* **38,** 1139–1151 (2009).
3. Hutmacher, D. W. Scaffolds in tissue engineering bone and cartilage. *Biomaterials* **21,** 2529–2543 (2000).
4. Hollister, S. J. Porous scaffold design for tissue engineering. *Nat. Mater.* **4,** 518–524 (2005).
5. Stevens, B., Yang, Y., Mohandas, A., Stucker, B. & Nguyen, K. T. A review of materials, fabrication methods, and strategies used to enhance bone regeneration in engineered bone tissues. *J. Biomed. Mater. Res. B. Appl. Biomater.* **85,** 573–582 (2008).
6. Bueno, E. & Glowacki, J. Cell-free and cell-based approaches for bone regeneration. *Nat. Rev. Rheumatol.* **5,** 685–697 (2009).
7. Venugopal, J., Low, S., Choon, A. T. & Ramakrishna, S. Interaction of Cells and Nanofiber Scaffolds in Tissue Engineering. *J. Biomed. Mater. Res. Part B* **84B,** 34–48 (2008).
8. Abbott, A. Cell culture: biology's new dimension. *Nature* **424,** 870–872 (2003).
9. Pampaloni, F., Reynaud, E. G. & Stelzer, E. H. K. The third dimension bridges the gap between cell culture and live tissue. *Nat. Rev. Mol. Cell Biol.* **8,** 839–845 (2007).
10. Justice, B. A., Badr, N. A. & Felder, R. A. 3D cell culture opens new dimensions in cell-based assays. *Drug Discov. Today* **14,** 102–107 (2009).
11. Griffith, L. G. & Naughton, G. Tissue engineering--current challenges and expanding opportunities. *Science* **295,** 1009–1014 (2002).
12. Tibbitt, M. W. & Anseth, K. S. Hydrogels as extracellular matrix mimics for 3D cell culture. *Biotechnol. Bioeng.* **103,** 655–663 (2009).
13. Ritchie, R. O., Buehler, M. J. & Hansma, P. Plasticity and toughness in bone. *Phys. Today* **62,** 41–47 (2009).
14. Domingues, R. M. A., Gomes, M. E. & Reis, R. L. The potential of cellulose nanocrystals in tissue engineering strategies. *Biomacromolecules* **15,** 2327–2346 (2014).
15. Lutolf, M. P. & Hubbell, J. A. Synthetic biomaterials as instructive extracellular microenvironments for morphogenesis in tissue engineering. *Nat. Biotechnol.* **23,** 47–55 (2005).
16. Griffith, L. G. & Swartz, M. A. Capturing complex 3D tissue physiology in vitro. *Nat. Rev. Mol. Cell Biol.* **7,** 211–224 (2006).
17. Engler, A. J., Sen, S., Sweeney, H. L. & Discher, D. E. Matrix elasticity directs stem cell lineage specification. *Cell* **126,** 677–689 (2006).
18. Zaman, M. H. *et al.* Migration of tumor cells in 3D matrices is governed by matrix stiffness along with cell-matrix adhesion and proteolysis. *Proc. Natl. Acad. Sci. U. S. A.* **103,** 10889–10894 (2006).
19. Pérez, R. a, Won, J.-E., Knowles, J. C. & Kim, H.-W. Naturally and synthetic smart composite biomaterials for tissue regeneration. *Adv. Drug Deliv. Rev.* **65,** 471–496 (2013).
20. Lutolf, M. P., Gilbert, P. M. & Blau, H. M. Designing materials to direct stem-cell fate. *Nature* **462,** 433–441 (2009).

21. Dvir, T., Timko, B. P., Kohane, D. S. & Langer, R. Nanotechnological strategies for engineering complex tissues. *Nat. Nanotechnol.* **6,** 13–22 (2011).

22. Grayson, W. L., Martens, T. P., Eng, G. M., Radisic, M. & Vunjak-Novakovic, G. Biomimetic approach to tissue engineering. *Semin. Cell Dev. Biol.* **20,** 665–73 (2009).

23. Bartnikowski, M., Klein, T. J., Melchels, F. P. W. & Woodruff, M. a. Effects of scaffold architecture on mechanical characteristics and osteoblast response to static and perfusion bioreactor cultures. *Biotechnol. Bioeng.* **111,** 1440–51 (2014).

24. Anseth, K. S., Bowman, C. N. & Brannon-Peppas, L. Mechanical properties of hydrogels and their experimental determination. *Biomaterials* **17,** 1647–1657 (1996).

25. Ahearne, M., Yang, Y. & Liu, K.-K. in *Top. Tissue Eng.* **4,** 1–16 (2008).

26. Xiao, Y., Friis, E. A., Gehrke, S. H. & Detamore, M. S. Mechanical Testing of Hydrogels in Cartilage Tissue Engineering: Beyond the Compressive Modulus. *Tissue Eng. Part B Rev.* **19,** 403–412 (2013).

27. Hunt, N. C., Smith, A. M., Gbureck, U., Shelton, R. M. & Grover, L. M. Encapsulation of fibroblasts causes accelerated alginate hydrogel degradation. *Acta Biomater.* **6,** 3649–3656 (2010).

28. Peterlik, H., Roschger, P., Klaushofer, K. & Fratzl, P. From brittle to ductile fracture of bone. *Nat. Mater.* **5,** 52–55 (2006).

29. Fratzl, P. Bone fracture: When the cracks begin to show. *Nat. Mater.* **7,** 610–612 (2008).

30. You, J. O., Rafat, M., Ye, G. J. C. & Auguste, D. T. Nanoengineering the heart: Conductive scaffolds enhance connexin 43 expression. *Nano Lett.* **11,** 3643–3648 (2011).

31. Dvir, T. *et al.* Nanowired three-dimensional cardiac patches. *Nat. Nanotechnol.* **6,** 720–5 (2011).

32. Shin, S. R. *et al.* Carbon-nanotube-embedded hydrogel sheets for engineering cardiac constructs and bioactuators. *ACS Nano* **7,** 2369–2380 (2013).

33. Drury, J. L. & Mooney, D. J. Hydrogels for tissue engineering: scaffold design variables and applications. *Biomaterials* **24,** 4337–4351 (2003).

34. Bhagat, S. D., Kim, Y.-H., Ahn, Y.-S. & Yeo, J.-G. Rapid synthesis of water-glass based aerogels by in situ surface modification of the hydrogels. *Appl. Surf. Sci.* **253,** 3231–3236 (2007).

35. Wang, C., Liu, H., Gao, Q., Liu, X. & Tong, Z. Alginate–calcium carbonate porous microparticle hybrid hydrogels with versatile drug loading capabilities and variable mechanical strengths. *Carbohydr. Polym.* **71,** 476–480 (2008).

36. Kang, H. W., Tabata, Y. & Ikada, Y. Fabrication of porous gelatin scaffolds for tissue engineering. *Biomaterials* **20,** 1339–1344 (1999).

37. Invitrogen. *Quant-iT ™ PicoGreen ® dsDNA Reagent and Kits*. (2008).

38. Invitrogen. *LIVE/DEAD ® Viability/Cytotoxicity Kit *for mammalian cells**. (2005).

39. Mosmann, T. Rapid colorimetric assay for cellular growth and survival: application to proliferation and cytotoxicity assays. *J. Immunol. Methods* **65,** 55–63 (1983).

40. Kuhn, D. M., Balkis, M., Chandra, J., Mukherjee, P. K. & Ghannoum, M. A. Uses and limitations of the XTT assay in studies of Candida growth and metabolism. *J. Clin. Microbiol.* **41,** 506–508 (2003).

41. Malich, G., Markovic, B. & Winder, C. The sensitivity and specificity of the MTS tetrazolium assay

for detecting the in vitro cytotoxicity of 20 chemicals using human cell lines. *Toxicology* **124,** 179–192 (1997).

42. Thermo Fisher Scientific Incorporated. *CellTracker ™ Fluorescent Probes*. (2014).

43. Rodrigues, M. *et al.* Synergistic effect of scaffold composition and dynamic culturing environment in multilayered systems for bone tissue engineering. *J. Tissue Eng. Regen. Med.* **6,** e24–e30 (2012).

44. Shin, S. R. *et al.* Carbon nanotube reinforced hybrid microgels as scaffold materials for cell encapsulation. *ACS Nano* **6,** 362–72 (2012).

45. Rezwan, K., Chen, Q. Z., Blaker, J. J. & Boccaccini, A. R. Biodegradable and bioactive porous polymer/inorganic composite scaffolds for bone tissue engineering. *Biomaterials* **27,** 3413–31 (2006).

46. Bhardwaj, N. & Kundu, S. C. Electrospinning: a fascinating fiber fabrication technique. *Biotechnol. Adv.* **28,** 325–47 (2010).

47. Cui, W., Zhou, Y. & Chang, J. Electrospun nanofibrous materials for tissue engineering and drug delivery. *Sci. Technol. Adv. Mater.* **11,** 014108 (2010).

48. Jang, J.-H., Castano, O. & Kim, H.-W. Electrospun materials as potential platforms for bone tissue engineering. *Adv. Drug Deliv. Rev.* **61,** 1065–83 (2009).

49. Bussy, C., Ali-Boucetta, H. & Kostarelos, K. Safety considerations for graphene: lessons learnt from carbon nanotubes. *Acc. Chem. Res.* **46,** 692–701 (2013).

50. Shin, S. R. *et al.* Cell-laden Microengineered and Mechanically Tunable Hybrid Hydrogels of Gelatin and Graphene Oxide. *Adv. Mater.* (2013). doi:10.1002/adma.201301082

51. Jun Han, Z. *et al.* Carbon nanostructures for hard tissue engineering. *RSC Adv.* **3,** 11058–11072 (2013).

52. Newman, P., Minett, A., Ellis-Behnke, R. & Zreiqat, H. Carbon nanotubes: their potential and pitfalls for bone tissue regeneration and engineering. *Nanomedicine* **9,** 1139–58 (2013).

53. Shao, S. *et al.* Osteoblast function on electrically conductive electrospun PLA/MWCNTs nanofibers. *Biomaterials* **32,** 2821–33 (2011).

54. Gupta, A. K. & Gupta, M. Synthesis and surface engineering of iron oxide nanoparticles for biomedical applications. *Biomaterials* **26,** 3995–4021 (2005).

55. Laurent, S. *et al.* Magnetic iron oxide nanoparticles: synthesis, stabilization, vectorization, physicochemical characterizations, and biological applications. *Chem. Rev.* **108,** 2064–110 (2008).

56. Sun, C., Lee, J. S. H. & Zhang, M. Magnetic nanoparticles in MR imaging and drug delivery. *Adv. Drug Deliv. Rev.* **60,** 1252–65 (2008).

57. Mahmoudi, M., Sant, S., Wang, B., Laurent, S. & Sen, T. Superparamagnetic iron oxide nanoparticles (SPIONs): Development, surface modification and applications in chemotherapy. *Adv. Drug Deliv. Rev.* **63,** 24–46 (2011).

58. Babes, L., Denizot, B., Tanguy, G., Le Jeune JJ & Jallet, P. Synthesis of Iron Oxide Nanoparticles Used as MRI Contrast Agents: A Parametric Study. *J. Colloid Interface Sci.* **212,** 474–482 (1999).

59. Kim, D. K., Zhang, Y., Voit, W., Rao, K. V. & Muhammed, M. Synthesis and characterization of surfactant-coated superparamagnetic monodispersed iron oxide nanoparticles. *J. Magn. Magn. Mater.* **225,** 30–36 (2001).

60. Teja, A. S. & Koh, P.-Y. Synthesis, properties, and applications of magnetic iron oxide nanoparticles. *Prog. Cryst. Growth Charact. Mater.* **55,** 22–45 (2009).

61. Boistelle, R. & Astier, J. Crystallization mechanisms in solution. *J. Cryst. Growth* **90,** 14–30 (1988).

62. Patzke, G. R., Zhou, Y., Kontic, R. & Conrad, F. Oxide Nanomaterials: Synthetic Developments, Mechanistic Studies, and Technological Innovations. *Angew. Chemie Int. Ed.* **50,** 826–859 (2011).

63. Chandra, V. *et al.* Water-dispersible magnetite-reduced graphene oxide composites for arsenic removal. *ACS Nano* **4,** 3979–3986 (2010).

64. Liu, M., Chen, C., Hu, J., Wu, X. & Wang, X. Synthesis of Magnetite/Graphene Oxide Composite and Application for Cobalt(II) Removal. *J. Phys. Chem. C* **115,** 25234–25240 (2011).

65. He, H. & Gao, C. Supraparamagnetic, conductive, and processable multifunctional graphene nanosheets coated with high-density Fe3O4 nanoparticles. *ACS Appl. Mater. Interfaces* **2,** 3201–3210 (2010).

66. Yang, X. *et al.* Superparamagnetic graphene oxide–Fe3O4 nanoparticles hybrid for controlled targeted drug carriers. *J. Mater. Chem.* **19,** 2710–2714 (2009).

67. Leng, Y. *Materials Characterization: Introduction to Microscopic and Spectroscopic Methods*. (John Wiley & Sons (Asia) Pte Ltd, 2008).

68. Warren, B. E. *X-Ray Diffraction*. (Dover Publications, Inc., 1990).

69. Muschol, M. & Rosenberger, F. Interactions in undersaturated and supersaturated lysozyme solutions: Static and dynamic light scattering results. *J. Chem. Phys.* **103,** 10424 (1995).

70. Hummers, W. J. & Offeman, R. Preparation of graphitic oxide. *J. Am. Chem. Soc.* **80,** 1339 (1958).

71. Kovtyukhova, N. I. *et al.* Layer-by-Layer Assembly of Ultrathin Composite Films from Micron-Sized Graphite Oxide Sheets and Polycations. *Chem. Mater.* **11,** 771–778 (1999).

72. Kim, J. E. *et al.* Graphene oxide liquid crystals. *Angew. Chem. Int. Ed. Engl.* **50,** 3043–7 (2011).

73. Bai, H., Li, C., Wang, X. & Shi, G. On the gelation of graphene oxide. *J. Phys. Chem. C* **115,** 5545–5551 (2011).

74. Ai, K., Liu, Y., Lu, L., Cheng, X. & Huo, L. A novel strategy for making soluble reduced graphene oxide sheets cheaply by adopting an endogenous reducing agent. *J. Mater. Chem.* **21,** 3365–3370 (2011).

75. Stankovich, S., Piner, R. D., Nguyen, S. T. & Ruoff, R. S. Synthesis and exfoliation of isocyanate-treated graphene oxide nanoplatelets. *Carbon N. Y.* **44,** 3342–3347 (2006).

76. Sun, X. *et al.* Nano-graphene oxide for cellular imaging and drug delivery. *Nano Res.* **1,** 203–212 (2008).

77. Zhu, C., Guo, S., Fang, Y. & Dong, S. Reducing Sugar : New Functional Molecules for the Green Synthesis of Graphene Nanosheets. **4,** 2429–2437 (2010).

78. Yang, S. *et al.* A facile green strategy for rapid reduction of graphene oxide by metallic zinc. *RSC Adv.* **2,** 8827–8832 (2012).

79. Akhavan, O., Ghaderi, E., Aghayee, S., Fereydooni, Y. & Talebi, A. The use of a glucose-reduced graphene oxide suspension for photothermal cancer therapy. *J. Mater. Chem.* **22,** 13773–13781 (2012).

80. Kumar, P. V. *et al.* Scalable enhancement of graphene oxide properties by thermally driven phase

transformation. *Nat. Chem.* **6,** 151–158 (2014).

81. Gao, X. & Tang, X. (Shirley). Effective reduction of graphene oxide thin films by a fluorinating agent: Diethylaminosulfur trifluoride. *Carbon N. Y.* **76,** 133–140 (2014).

82. Stankovich, S. *et al.* Synthesis of graphene-based nanosheets via chemical reduction of exfoliated graphite oxide. *Carbon N. Y.* **45,** 1558–1565 (2007).

83. Huang, X., Qi, X., Boey, F. & Zhang, H. Graphene-based composites. *Chem. Soc. Rev.* **41,** 666–86 (2012).

84. Srivastava, S. *et al.* Innovative synthesis of citrate-coated superparamagnetic Fe3O4 nanoparticles and its preliminary applications. *J. Colloid Interface Sci.* **359,** 104–11 (2011).

85. Su, J., Cao, M., Ren, L. & Hu, C. Fe3O4-Graphene Nanocomposites with Improved Lithium Storage and Magnetism Properties. *J. Phys. Chem. C* **115,** 14469–14477 (2011).

86. Wu, Q., Feng, C., Wang, C. & Wang, Z. A facile one-pot solvothermal method to produce superparamagnetic graphene-Fe3O4 nanocomposite and its application in the removal of dye from aqueous solution. *Colloids surfaces B Biointerfaces* **101,** 210–214 (2013).

87. Li, D., Müller, M. B., Gilje, S., Kaner, R. B. & Wallace, G. G. Processable aqueous dispersions of graphene nanosheets. *Nat. Nanotechnol.* **3,** 101–105 (2008).

88. Fajaroh, F., Setyawan, H., Nur, A. & Lenggoro, I. W. Thermal stability of silica-coated magnetite nanoparticles prepared by an electrochemical method. *Adv. Powder Technol.* **24,** 507–511 (2013).

89. Choi, E.-Y. *et al.* Noncovalent functionalization of graphene with end-functional polymers. *J. Mater. Chem.* **20,** 1907–1912 (2010).

90. Zhang, Y. *et al.* Controlled assembly of Fe3O4 magnetic nanoparticles on graphene oxide. *Nanoscale* **3,** 1446–1450 (2011).

91. Lerf, A., He, H., Forster, M. & Klinowski, J. Structure of Graphite Oxide Revisited. **102,** 4477–4482 (1998).

92. Smidsrød, O. & Skjåk-Bræk, G. Alginate as immobilization matrix for cells. *Trends Biotechnol.* **8,** 71–78 (1990).

93. Jeon, O., Bouhadir, K. H., Mansour, J. M. & Alsberg, E. Photocrosslinked alginate hydrogels with tunable biodegradation rates and mechanical properties. *Biomaterials* **30,** 2724–2734 (2009).

94. Lee, C. *et al.* Bioinspired, Calcium-Free Alginate Hydrogels with Tunable Physical and Mechanical Properties and Improved Biocompatibility. *Biomacromolecules* **14,** 2004–2013 (2013).

95. Connon, C. J. & Hamley, I. W. *Hydrogels in Cell-Based Therapies*. (2014).

96. Ahearne, M., Yang, Y., El Haj, A. J., Then, K. Y. & Liu, K.-K. Characterizing the viscoelastic properties of thin hydrogel-based constructs for tissue engineering applications. *J. R. Soc. Interface* **2,** 455–463 (2005).

97. Kong, H. J., Wong, E. & Mooney, D. J. Independent control of rigidity and toughness of polymeric hydrogels. *Macromolecules* **36,** 4582–4588 (2003).

98. Cha, C. *et al.* Controlling Mechanical Properties of Cell-Laden Hydrogels by Covalent Incorporation of Graphene Oxide. *Small* 1–10 (2013). doi:10.1002/smll.201302182

99. Nishiguchi, A., Yoshida, H., Matsusaki, M. & Akashi, M. Rapid construction of three-dimensional multilayered tissues with endothelial tube networks by the cell-accumulation technique. *Adv. Mater.* **23,** 3506–3510 (2011).

100. Guillame-Gentil, O. *et al.* Engineering the extracellular environment: Strategies for building 2D and 3D cellular structures. *Adv. Mater.* **22,** 5443–5462 (2010).

101. Shin, S. R. *et al.* Layer-by-Layer Assembly of 3D Tissue Constructs with Functionalized Graphene. *Adv. Funct. Mater.* **24,** 6136–6144 (2014).

102. Cooper, A., Jana, S., Bhattarai, N. & Zhang, M. Aligned chitosan-based nanofibers for enhanced myogenesis. *J. Mater. Chem.* **20,** 8904–8911 (2010).

103. Wilson, S. L. *et al.* Chemical and topographical effects on cell differentiation and matrix elasticity in a corneal stromal layer model. *Adv. Funct. Mater.* **22,** 3641–3649 (2012).

104. Torbet, J. *et al.* Orthogonal scaffold of magnetically aligned collagen lamellae for corneal stroma reconstruction. *Biomaterials* **28,** 4268–4276 (2007).

105. Sapir, Y., Cohen, S., Friedman, G. & Polyak, B. The promotion of in vitro vessel-like organization of endothelial cells in magnetically responsive alginate scaffolds. *Biomaterials* **33,** 4100–4109 (2012).

106. Liu, H. & Brinson, L. C. Reinforcing efficiency of nanoparticles: A simple comparison for polymer nanocomposites. *Compos. Sci. Technol.* **68,** 1502–1512 (2008).

107. Erb, R. M., Libanori, R., Rothfuchs, N. & Studart, A. R. Composites reinforced in three dimensions by using low magnetic fields. *Science* **335,** 199–204 (2012).

108. Jiao, W. *et al.* Improving the gas barrier properties of Fe3O4/graphite nanoplatelet reinforced nanocomposites by a low magnetic field induced alignment. *Compos. Sci. Technol.* **99,** 124–130 (2014).

109. Ma, H.-L. *et al.* Chemical reduction and removal of Cr(vi) from acidic aqueous solution by ethylenediamine-reduced graphene oxide. *J. Mater. Chem.* **22,** 5914–5916 (2012).

110. Kim, N. H., Kuila, T. & Lee, J. H. Simultaneous reduction, functionalization and stitching of graphene oxide with ethylenediamine for composites application. *J. Mater. Chem. A* **1,** 1349–1358 (2013).

111. Wang, J.-Y. *et al.* Preparation and properties of graphene oxide/polyimide composite films with low dielectric constant and ultrahigh strength via in situ polymerization. *J. Mater. Chem.* **21,** 13569–13575 (2011).

112. Shoichet, M. S., Li, R. H., White, M. L. & Winn, S. R. Stability of hydrogels used in cell encapsulation: An in vitro comparison of alginate and agarose. *Biotechnol. Bioeng.* **50,** 374–381 (1996).

113. Cohen, J. *et al.* Survival of porcine mesenchymal stem cells over the alginate recovered cellular method. *J. Biomed. Mater. Res. A* **96,** 93–99 (2011).

114. Smetana, K. Cell biology of hydrogels. *Biomaterials* **14,** 1046–1050 (1993).

115. Rowley, J. A., Madlambayan, G. & Mooney, D. J. Alginate hydrogels as synthetic extracellular matrix materials. *Biomaterials* **20,** 45–53 (1999).

116. Wu, L. *et al.* Magnetically induced anisotropic orientation of graphene oxide locked by in situ hydrogelation. *ACS Nano* **8,** 4640–9 (2014).

Appendix A: Supplementary Data for GO-Fe_3O_4 Hydrogels

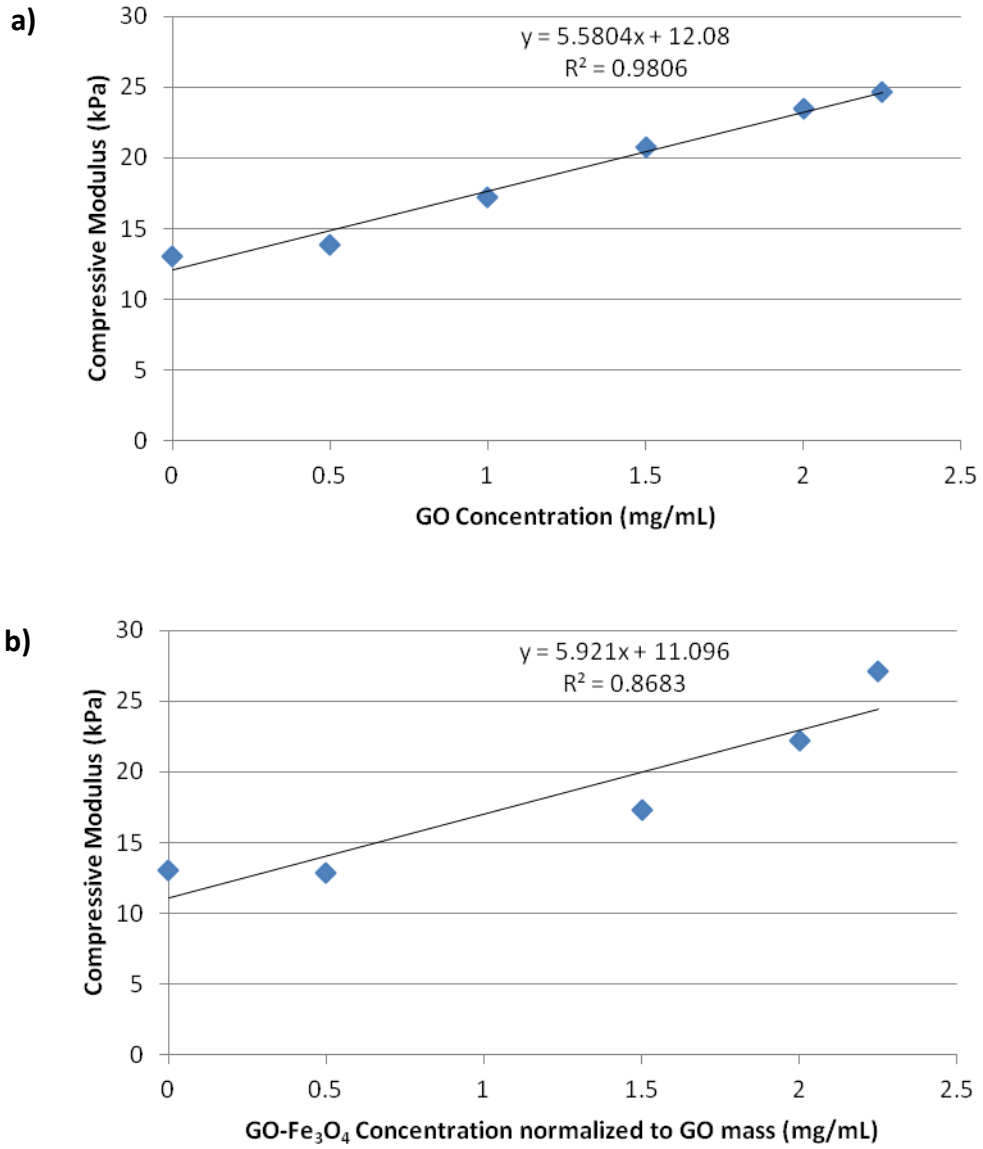

Figure A.1: Relationship between compressive modulus and nanoparticle concentration. a) Compressive modulus plotted against nanoparticle concentration for GO hydrogels. b) Compressive modulus plotted against nanoparticle concentration for GO-Fe_3O_4 hydrogels.

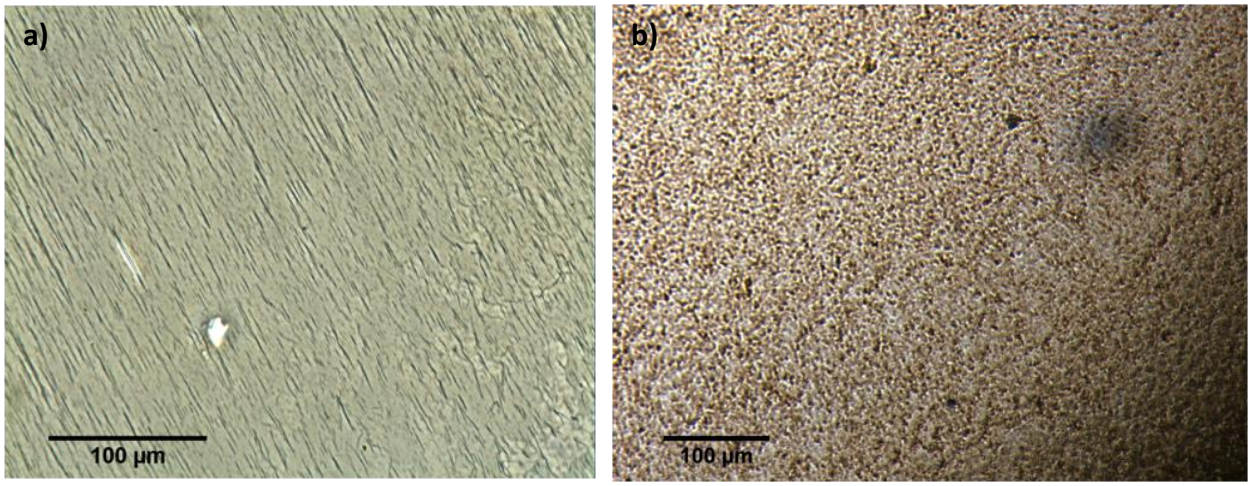

Figure A.2: Nanoparticle solutions dried on glass slides under an applied magnetic field of ~30mT. a) Fe_3O_4 coated with alginate, b) GO-Fe_3O_4 coated with alginate, which does not show any anisotropic ordering.

Appendix B: FTIR Spectra for Starting Materials

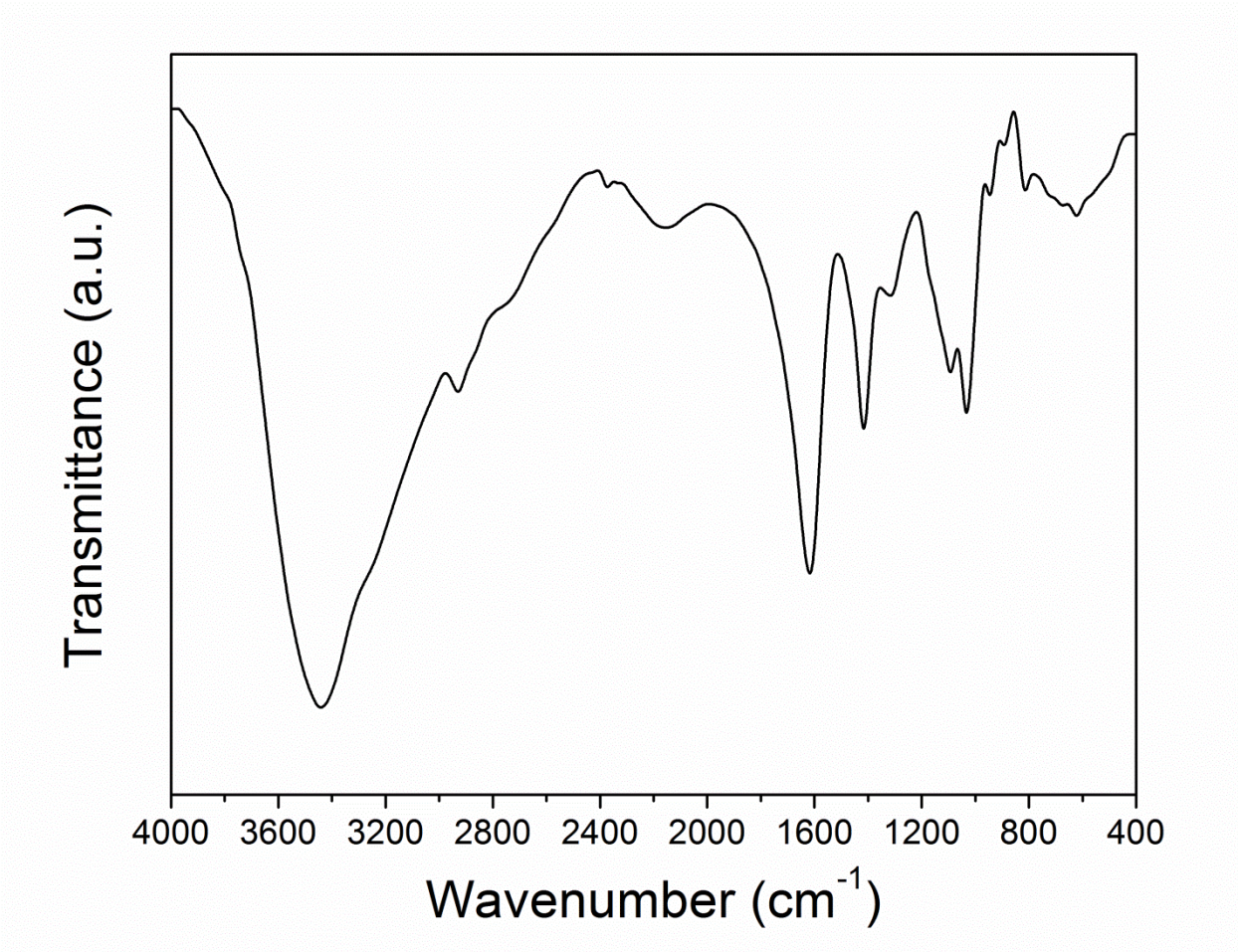

Figure B.1 : FTIR spectrum acquired for alginate.

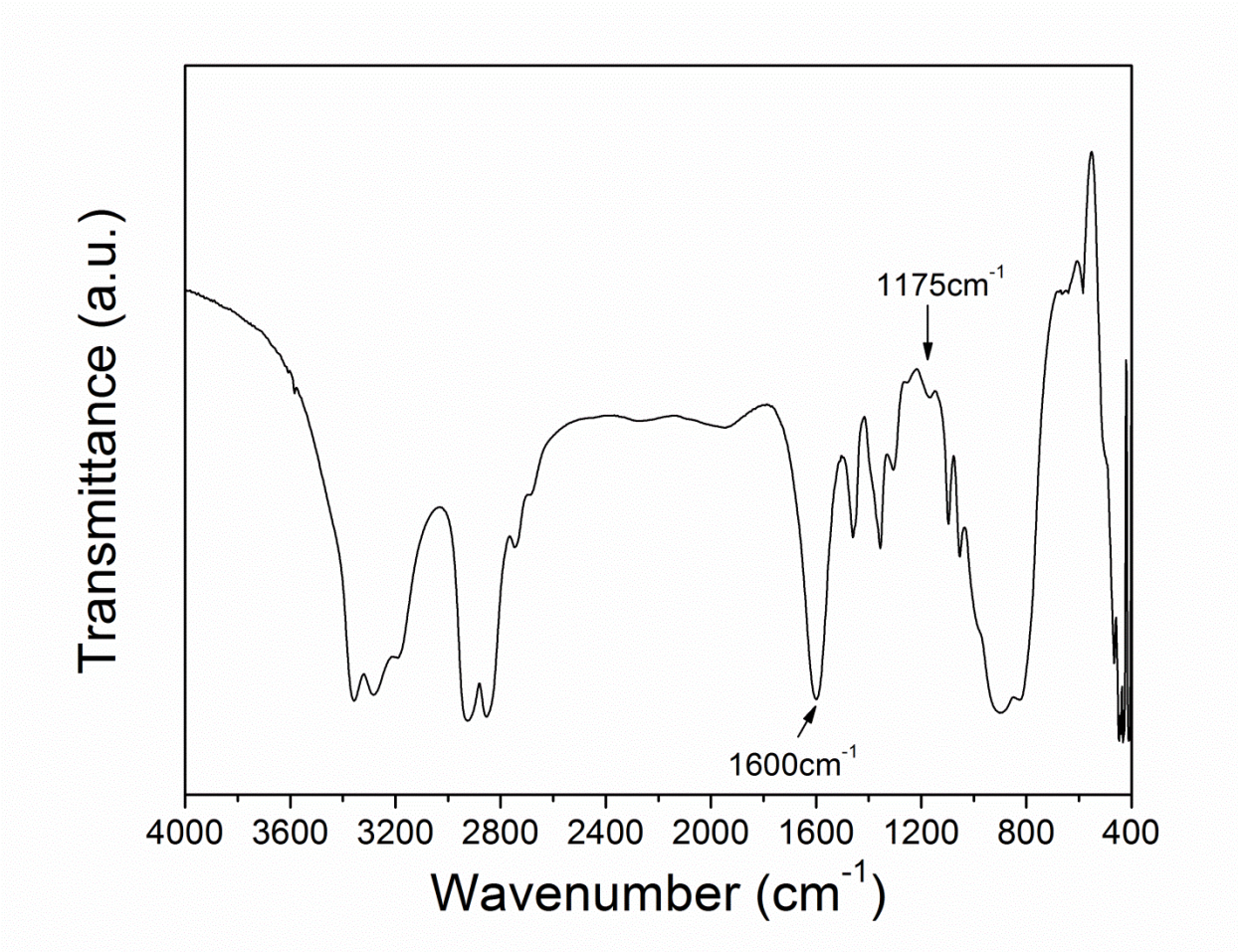

Figure B.2 : FTIR spectrum for ethylenediamine.

Appendix C: Supplementary CLSM images

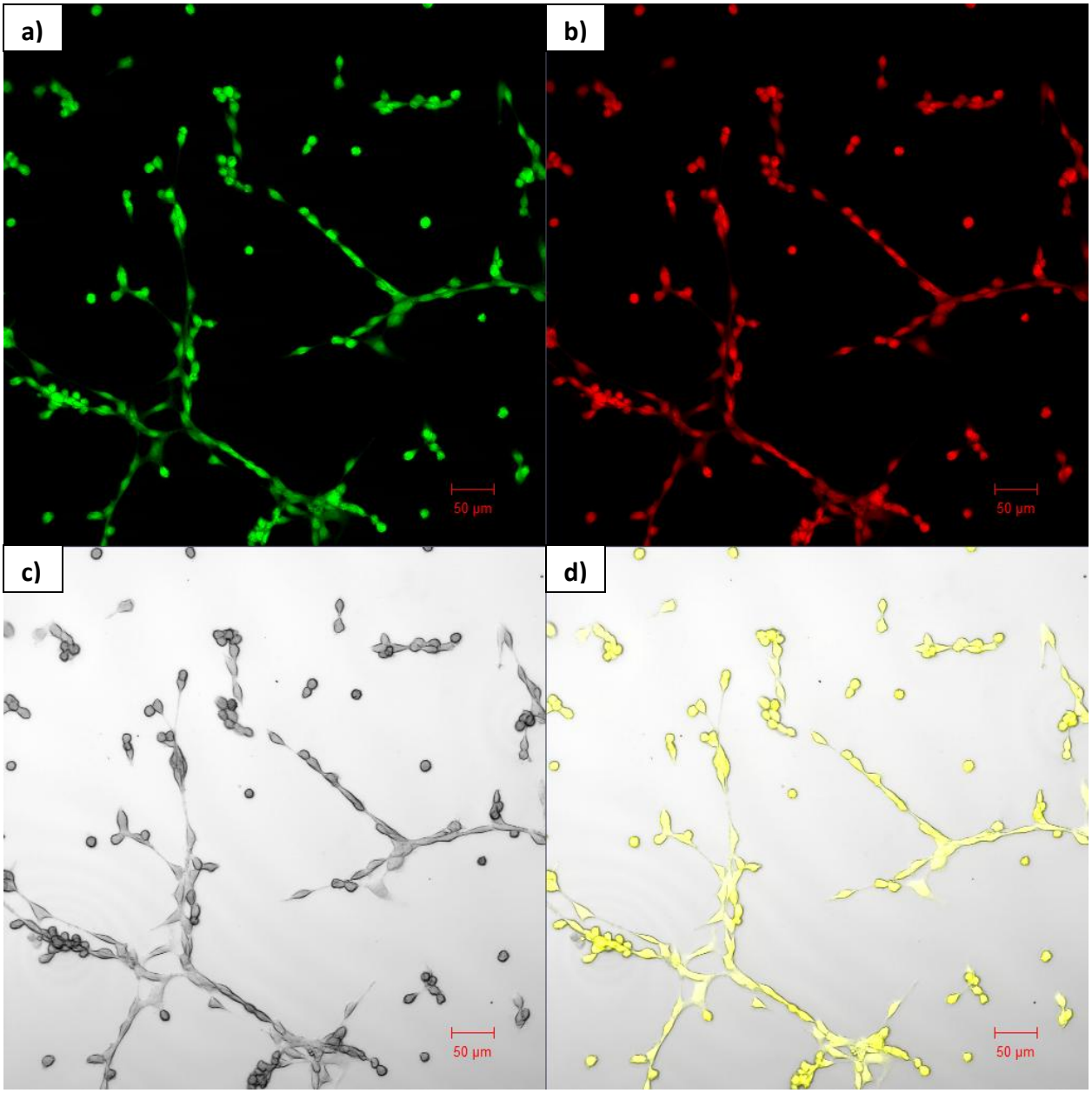

Figure C.1: CLSM images of 3T3 fibroblasts labelled with calcein-AM (green) and EthD-1 (red); Day 1 control. Images are split such that each channel can be individually seen: a) FITC filter, b) rhodamine filter, c) bright field/DIC, d) composite image.

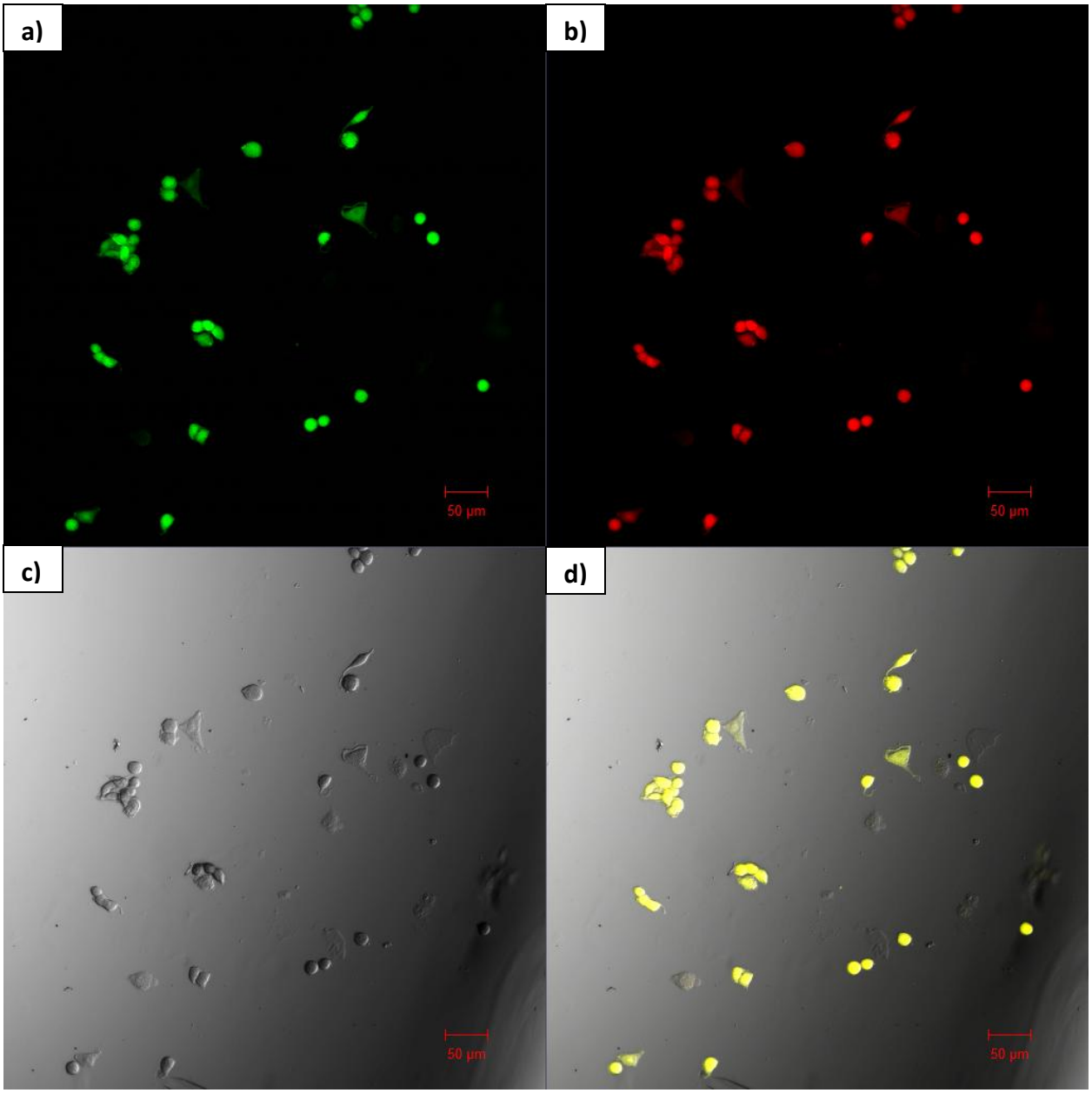

Figure C.2: CLSM images of 3T3 fibroblasts labelled with calcein-AM (green) and EthD-1 (red); Day 1, fibroblasts seeded on alginate films. Images are split such that each channel can be individually seen: a) FITC filter, b) rhodamine filter, c) bright field/DIC, d) composite image.

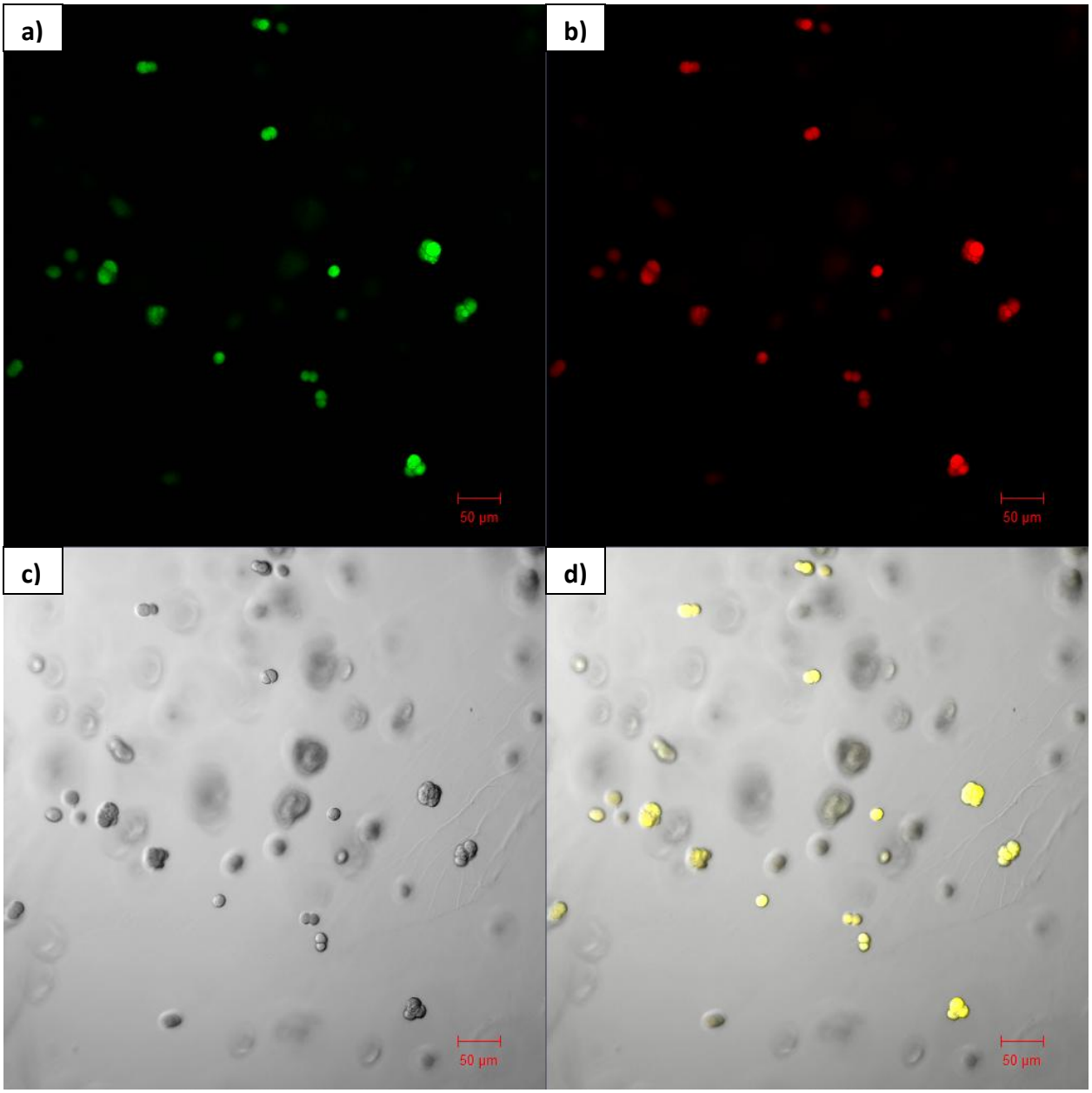

Figure C.3: CLSM images of 3T3 fibroblasts labelled with calcein-AM (green) and EthD-1 (red); Day 1, fibroblasts encapsulated in alginate films. Images are split such that each channel can be individually seen: a) FITC filter, b) rhodamine filter, c) bright field/DIC, d) composite image.

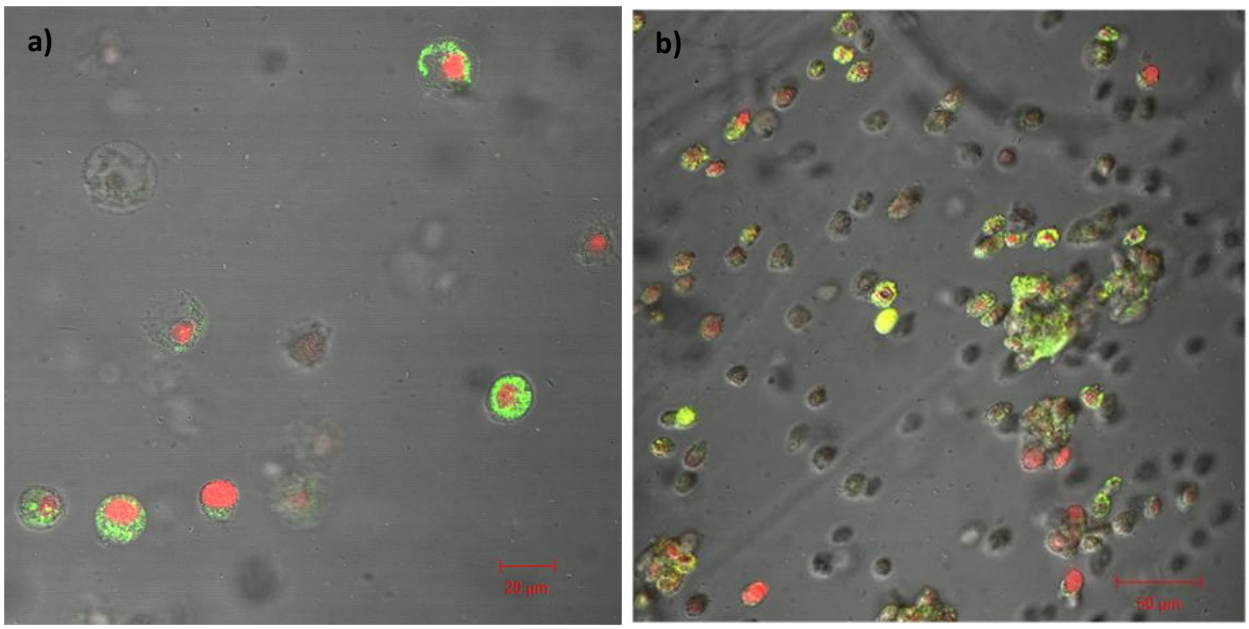

Figure C.4: CLSM images of 3mm thick alginate hydrogels, crosslinked in a mold. a) 1w/v% alginate hydrogels crosslinked for 30min. Cell lysis is evident, and the green and red dyes are not co-localized. b) 2w/v% alginate hydrogels crosslinked for 45min. Cell lysis is also evident.